EXPERIMENTAL STUDIES ON COLLECTIVE PHENOMENA IN DUSTY PLASMAS

By

MANGILAL CHOUDHARY

PHYS06201104003

Institute for Plasma Research, Gandhinagar

A thesis submitted to the
Board of Studies in Physical Sciences

In partial fulfillment of the requirements

For the Degree of

DOCTOR OF PHILOSOPHY

of

HOMI BHABHA NATIONAL INSTITUTE

April 2017

Homi Bhabha National Institute

Recommendations of the Viva Voce Committee

As members of the Viva Voce Committee, we certify that we have read the dissertation prepared by **Mangilal Choudhary** entitled "EXPERIMENTAL STUDIES ON COLLECTIVE PHENOMENA IN DUSTY PLASMAS" and recommend that it may be accepted as fulfilling the thesis requirement for the award of Degree of Doctor of Philosophy.

Date : 23/06/2017

Chairman : Prof. Sudip Sengupta

Date : 23.06.2017

Guide/Convener : Prof. Subroto Mukherjee

23/6/'17

Date : 23.06.2017

Examiner : Prof. Mridul Bose

Date : 23/06/2017

Member : Dr. G. Ravi

Pintu Bandyopadhyay

Date : 23/06/2017

Member : Dr. Pintu Bandhyopadhyay

Date : 23/06/2017

Technical Advisor : Dr. Suryakant Gupta

Final approval and acceptance of this thesis is contingent upon the candidate's submission of the final copies of the thesis to HBNI.

I hereby certify that I have read this thesis prepared under my direction and recommend that it may be accepted as fulfilling the thesis requirement.

Date : 23.06.2017

Place : Gandhinagar

Guide : Prof. Subroto Mukherjee

STATEMENT BY AUTHOR

Mangilal

Mangilal Choudhary

DECLARATION

I, hereby declare that the investigation presented in the thesis has been carried out by me. The work is original and the work has not been submitted earlier as a whole or in part for a degree/diploma at this or any other Institution or University.

Mangilal

Mangilal Choudhary

List of Publications arising from the thesis

Journal:

- **"Long–time evolution of a low pressure laboratory plasma after application of transient high voltage positive pulses"**,
  Mangilal Choudhary, S. Kar and S. Mukherjee,
  Contributions to Plasma Physics 56, 878 (2016)

- **"Propagation characteristics of dust–acoustic waves in presence of a floating cylindrical object in the DC discharge plasma"**,
  Mangilal Choudhary, S. Mukherjee and P. Bandyopadhyay,
  Phys. Plasmas 23, 083705 (2016)

- **"Transport and trapping of dust particles in a potential well created by inductively coupled diffused plasmas"**,
  Mangilal Choudhary, S. Mukherjee and P. Bandyopadhyay,
  Rev. Sci. Instrum. 87, 053505 (2016)

- **"Experimental observation of self excited co–rotating multiple vortices in a dusty plasma with inhomogeneous plasma background"**,
  Mangilal Choudhary, S. Mukherjee and P. Bandyopadhyay,
  Phys. Plasma 24, 033703 (2017)

Conferences/Schools:

International Participation

- "Transport and dynamical behavior of dust particles in a potential well created by inductively coupled diffused plasma"
  18^{th} International Congress on Plasma Physics (ICPP - 2016),
  Kaohsiung, Taiwan, June 27 - July 1, 2016.

- "Propagation characteristics of dust-acoustic waves in presence of a floating object in the DC discharge plasma",
  10^{th} Asia Plasma and Fusion Association Conference (APFA - 2015),
  Institute for Plasma Research, Gandhinagar, India, December 14 - 18, 2015.

- "7^{th} International Conference on the Physics of Dusty Plasma (ICPDP - 2016)".
  New Delhi, India, March 3 - 7, 2014.

National Participation

- "A Study of self–excited dust acoustic waves in the dust medium trapped at diffused plasma in variable cross–section tube",
  30^{th} National Symposium on Plasma Science and Technology (PLASMA-2015),
  Saha Institute of Nuclear Physics, Kolkata, India, December 1 - 4, 2015.

- "Hands on School on Nonlinear Dynamics - 2015 (HSND - 2015)"
  Institute for Plasma Research, Gandhinagar, India, February 16 - 22, 2015.

- "Long–time evolution of low pressure plasma after application of transient high voltage positive pulses",
  28^{th} National Symposium on Plasma Science and Technology (Plasma - 2013),
  KIIT University, Bhubaneswar, India, December 3 - 6, 2013.

- DST SERC School on Tokamaks and Magnetized Plasma Fusion.
  Institute for Plasma Research, Gandhinagar, India, February 25 - March 15, 2013.

- "Transient evolution of electron energy distribution function of solitary electron hole in laboratory low pressure plasma",

27^{th} National Symposium on Plasma Science and Technology (Plasma - 2012),

Pondicherry University, India, December 10 - 13, 2012.

- 1^{st} PSSI - Plasma Scholars Colloquium (PPSC - 2012).

  Institute for Plasma Research, Gandhinagar, India, July 3 - 4, 2012.

Mangilal

Mangilal Choudhary

To my family with Love and affection

ACKNOWLEDGEMENTS

This thesis marks the end of my journey in obtaining my PhD. This thesis has been kept on track and been seen through to completion with the support and encouragement of numerous people, friends, well wishers and colleagues. At the end of my thesis, I would like to thank all those people who made this thesis possible and an unforgettable experience for me.

At this moment of accomplishment, first of all I would like to express deep gratitude to my thesis supervisor, Prof. Subroto Mukherjee for his guidance, encouragement and gracious support throughout this research work. Under his guidance I successfully overcame many difficulties and learned a lot. Without his valuable assistance, this work would not have been completed. He has been a strong and supportive adviser to me throughout my doctoral research. I specially thank him for the freedom that he has given me to do research and his availability for discussion at any time. I am thankful to him for encouraging me during difficult personal circumstances and remembering these moments, words fail me in thanking him for his support. I am eternally grateful to him for his supportive and friendly nature.

I wish to express my thanks to Dr. Pintu Bandyopadhyay for thoroughly checking each of my research manuscripts, numerous helpful comments which have improved my understanding and enriched my knowledge. I have enjoyed many stimulating discussions with him and learned various image analysis techniques.

I would also like to thank Dr. S. Kar for his constant support and encouragements during the initial period of this long journey. I learned various experimental techniques from him.

I am also very thankful to Prof. Abhijit Sen, Prof. R. Ganesh, Dr. M. Bandyopadhyay and Dr. D. Sharma for their advice, discussion, and support that I got from them.

I extend my thanks and polite acknowledgement to my Doctoral Committee including Prof. S. Sengupta (Chairman), Dr. G. Ravi, Dr. P. Bandyopadhyay and Dr. S. Gupta for their critical evaluation and constant support throughout the work. I am thankful to them for their valuable suggestions during the progress reviews. I would like to express my sincere gratitude to Prof. D. Bora, who was my previous doctoral committee chairman, for his valuable guidance and suggestions throughout the work.

I would like to acknowledge, Prof. A. Das, Prof. R. Ganesh, Prof. S. Sengupta, Prof. S. Mukherjee, Prof. P. K. Chattopadhyay, Dr. J. Ghosh, Dr. D. Sharma, Dr. M. Kundu, Dr. S. Karkari, Dr. N. Bisai, Dr. D. Chandra, Dr. D. Raju, Dr. G. Ravi, Dr. R. Srinivasan, and others who have taught me plasma physics and other relevant subjects.

I would like to express my deep thanks to FCIPT staff, Dr. G. Ravi, Dr. S. K. Nema, Dr. S. Gupta, Dr. Alphonsa Joseph, Dr. M. Ranjan, Dr. Balasubramanian, Dr. Vishal Jain, Dr. Nirav Jamnapara, R. Rane, Sagar Agarwal, A. Satyaprasad, Anand Visani, Purvi Kikani, Nisha Chandwani, Keena Kalaria, P. V. Murugan, Narendra Chauhan, Adam bhai, Vagela bhai, Garima Joshi and Parchi for their kind help for carrying out my experiments.

I would like to thanks FCIPT workshop staff Gautam R Vadolia, Kaila bhai (Mama), Sanjay and Vipul for their outstanding support in making the parts of experimental system. I would like to give special thanks to FCIPT electronics devision staff B. K. Patel, Chirayu Patil, and Vijay bhai for their help in making the electronic circuits. I would like to thank Akshay Vaid for providing the drawing of experimental setup. I am thankful to Satish for resolving computer related issues that I had faced in this duration.

I am also thankful to staff in the IPR library, Administration, the Purchase department, the Store, Workshop and Computer Center for their kind support during the PhD tenure. I am thankful to the Institute for Plasma Research, Gandhinagar to give me an opportunity to complete my doctoral research.

I would like to thank Neeraj Chaubey separately for being a friend before a labmate. Thank you dear for being with me in ups and downs of life during last 5 years and for keeping a healthy atmosphere in lab. I would also like to give special thanks to my senior Vikram Singh Dharodi for the quality time that I have spent with him. I would like to give special thanks to my senior Soumen Ghosh for the outstanding support he has offered me during this long journey. Our discussions and his suggestions were always very valuable. I also acknowledge to Vidhi Goyal for her support during the tough time of my life. My special thanks to Deepak bhai, Satya bhai, Sayak da, Soumen da, Vikram dharodi, Neeraj, Meghraj, Samir, Chandrasekhar and Jervis for reading my manuscripts and thesis chapters and giving fruitful suggestions. I would also like to give my special thanks to my seniors Jugal bhai, Satya bhai, Khitish bhai, Deepak bhai, Guru bhai, Aditya bhai and Soumen da for their constant support and helping me to understand various aspects of life.

My heartfelt thanks to my college roommate Dipesh Trivedi, Praveen Singh Rajpurohit, Hitesh and Chandekant Dave for providing me moral support and helping in various aspects. I would like to acknowledge Dr. Mridul Bose and Sanjeeb Sarkar for introducing me to the field of dusty plasma during my visit to Jadavpur University.

I would like to thank all my seniors Sharad bhai, Satya bhai, Shekar bhai, Jugal bhai, Kshitish bhai, Deepak bhai, Ujjwal bhai, Gurudatt bhai, Vikram paji, Prabal bhai, Ashwin bhai, Sita di, Rameswar bhai, Sushil bhai, Sanat bhai, Pravesh bhai, Sayak da, Manjit di, Aditya bhai, Soumen da, and Vikram for their best wishes and moral supports during the Ph.D tenure. I thank my batch mates Neeraj, Vara, Bibhu, Rupendra, Chandrasekhar, Meghraj, Akanksha, Vidhi, Deepa, Harish, and Samir for the quality time that I have spent with them. I would also like to convey my best wishes to my juniors, Sonu, Debraj, Ratan, Umesh, Narayan, Modhu, Amit, Arghaya, Bhumika, Sagar, Atul, Deepak, Alam, Jervis, Sandeep, Prabhakar, Minakhi, Pallvi, Avnish, Shivam, Rupak, Chinmoy and other scholars and TTPs for creating a friendly ambiance around me.

I thank with love to Rekha and Param, my wife and son. You, Rekha has been my best friend and great companion, loved, supported, encouraged and helped me get through this agonizing period in the most positive way. I greatly value her contribution and deeply appreciate her belief in me. Words would never say how grateful I am to you. I don't want to win the race of life by being the fastest runner. I want to win it by walking slowly, hand in hand with you. Thanks dear for making every day of our lives a grand celebration.

Finally, I would extend my respect to my parents (Late Shri Achalaram Ji and Smt. Jamani Baai), my brother (Late Mohan Choudhary) and sisters (Jatu and Bhanvri) and all elders in my family. I can't imagine a life without their love and blessings. Thank you "Papa Ji and Mummy Ji" for showing faith in me and giving me liberty to choose what I desired.

Contents

Synopsis . . . xiii
List of Figures . . . xiii

1 Introduction **1**
- 1.1 Introduction . . . 1
  - 1.1.1 Dusty plasma . . . 2
  - 1.1.2 Dusty plasma in universe and atmosphere . . . 2
  - 1.1.3 Dusty plasma in laboratory . . . 4
- 1.2 Key features of laboratory dusty plasma . . . 6
- 1.3 Fundamental properties of dusty plasma . . . 7
  - 1.3.1 Dust charging processes . . . 8
  - 1.3.2 Quasi–neutrality condition . . . 12
  - 1.3.3 Debye shielding . . . 13
  - 1.3.4 Characteristic frequency . . . 14
  - 1.3.5 Coulomb coupling constant . . . 15
- 1.4 Forces acting on the dust grains . . . 16
  - 1.4.1 Gravitation force . . . 16
  - 1.4.2 Electrostatic force . . . 16
  - 1.4.3 Ion drag force . . . 16
  - 1.4.4 Neutral drag force . . . 18
  - 1.4.5 Thermophoretic force . . . 18
- 1.5 Dusty plasma formation using different electrostatic traps . . . 19
- 1.6 Overview of the earlier work . . . 21
- 1.7 Motivation behind the present research work . . . 24
- 1.8 Scope and outline of the thesis . . . 25

2 Experimental Setup and Diagnostics **28**
- 2.1 Introduction . . . 28
- 2.2 Experimental setup . . . 29
  - 2.2.1 Vacuum vessels and pumping system . . . 29
  - 2.2.2 Cathode and anode . . . 31
  - 2.2.3 Power supplies . . . 32
- 2.3 Plasma and dusty plasma production . . . 34

2.3.1 DC glow discharge plasma . . . 34
2.3.2 Inductively coupled discharge plasma . . . 38
2.4 Plasma diagnostics . . . 38
2.4.1 Single Langmuir probe . . . 39
2.4.2 Double probe . . . 44
2.4.3 Emissive probe . . . 47
2.5 Dust grain diagnostics . . . 50
2.5.1 Imaging . . . 50
2.5.2 Magnification of the object . . . 51
2.5.3 Data storage . . . 52
2.5.4 Image analysis . . . 52

3 Dust Acoustic Wave and its Propagation Characteristics in Presence of a Floating Object 54
3.1 Introduction . . . 54
3.2 Experimental setup . . . 57
3.3 Plasma production and its characterization . . . 59
3.4 Dusty plasma and its characterization . . . 60
3.5 Results on the dust acoustic waves . . . 63
3.5.1 Excitation of dust acoustic waves . . . 63
3.5.2 Dispersion relation of dust acoustic wave . . . 63
3.5.3 Characteristics of dust acoustic waves . . . 65
3.6 Characteristics of dust acoustic waves in presence of a floating object 68
3.6.1 Vertically aligned floating rod . . . 68
3.6.2 Horizontally aligned floating rod . . . 72
3.7 Summary and conclusions . . . 76

4 Transport and Trapping of Dust Particles in Diffused Plasma 80
4.1 Introduction . . . 80
4.2 Experimental device and techniques . . . 82
4.3 Characterization of diffused plasma . . . 85
4.3.1 Plasma density and electron temperature variation . . . 85
4.3.2 Plasma potential variation . . . 87
4.4 Dust grain transport and trapping . . . 92
4.5 Summary and conclusions . . . 98

5 Multiple Co–rotating Vortex Structures **99**
5.1 Introduction 99
5.2 Dusty plasma and its characteristics 101
5.3 Observations on dust vortices 104
5.3.1 Vortices in a plane at different input RF powers 104
5.3.2 Velocity distribution in vortex structures 105
5.3.3 Vortices in different planes at a constant power 107
5.4 Origin of multiple dust vortices 108
5.4.1 Formation of a vortex 108
5.4.2 Formation of the multiple vortices 117
5.5 Summary and conclusion 118

6 Summary and Future Scope **120**
6.1 Summary and conclusion 120
6.2 Future work 124

SYNOPSIS

Dusty plasma consists of sub-micron to micron sized particles embedded in two components electron-ion plasma. Depending on the plasma environment surrounding the dust grain, it may get either positive or negative charge. In low temperature laboratory plasma, due to higher mobility of electrons, the electron flux on the dust particle surface is comparatively higher than that of the ion flux. Because of higher electron flux and the large size, dust particle acquires a high negative charge of the order of $10^3 - 10^5e$. Owing to the high charge on dust particles, the dust-dust interaction as well as dust-plasma species (electrons and ions) interaction get stronger and causes the increase in complexity of the ambient plasma. Thus, they either modify the collective modes of the electron-ion plasma or show entirely new collective modes such as linear and nonlinear waves [1–7] and dynamic structures (vortices) [8–13]. Due to the heavy mass of dust grain, the dynamics of dust particles is quite slow in comparison to the background lighter species (electrons and ions). Therefore, imaging of their dynamics is possible by simple imaging diagnostics. Hence, this is a unique medium which offers a way to study complex collective phenomena (due to high charge) at slow time scale (due to heavy mass) which may not accessible with conventional two component plasma. These novel aspects of dusty plasma have attracted a great deal of interest to study the dynamics of the dusty plasma medium in a controlled manner in the laboratory.

For the studies of dusty plasma in the laboratory, it is necessary to create a dusty plasma with dimensions larger than the characteristic length scale of the dust collective modes (waves and vortices). In addition to that, a potential well is required to confine the dust grains for the time longer than the characteristic time of dust oscillation. On the other hand, it is well known that dust dynamics is self–consistently associated to the motion of the background species (electrons, ions and neutrals), which gets modified when an equilibrium of the surrounding plasma is changed. In fact, an equilibrium of dust medium can be modified either by applying an external field or self–consistently (due to the change of discharge parameters), resulting in the modification of the dynamics of the dust-plasma system [14–16]. However, various configurations have been used to produce dusty plasma for studying the collective modes [2, 13, 17–20], still the studies of such modes and its characteristics with an external perturbation in a large volume dusty plasma need to be explored.

This thesis focuses on the experimental configurations to produce large volume dust medium at comparatively low argon pressure ($\leq$ 0.07 mbar) and to study the role of ambient plasma environment on the collective dynamics of the dusty plasma medium. For producing the dusty plasma, at first, conventional DC discharge (cathode–anode) configuration is employed. Excitation of waves and its characteristics with an external potential perturbation are investigated in a 3-dimensional (3D) dusty plasma at an argon pressure of 0.07 mbar. Working at even low pressure ($<$ 0.05 mbar) using the DC discharge configuration makes dust medium highly unstable. Therefore; for the formation of an equilibrium dusty plasma at lower pressure (0.05 to 0.01 mbar), a novel configuration using inductively coupled plasma is investigated to confine the dust grains. In this electrodeless configuration, negatively charged particles are confined in a potential well of the diffused plasma. For injecting dust grains into a potential well, a unique technique using the DC plasma source is also employed. Collective dynamics of the confined dust grains, which exhibits waves and/or vortex structures, are studied at the wide range of discharge parameters. The underlying physics causing the modification in the propagation characteristics of the dust acoustic wave with an external electric perturbation, particles transport and confinement in a potential well of the diffused plasma, and collective modes in large volume dusty plasma are thoroughly investigated.

We provide below the summary of the experimental work carried out in this thesis.

Dusty plasma in the laboratory is produced using two different discharge (DC and RF) configurations. In the DC configuration, discharge is initiated by applying a high negative DC voltage to cathode with respect to the anodes, which are grounded through a resistance. Strong electric field present in the cathode sheath is exploited to levitate the negatively charged dust particles in an equilibrium bowl shaped (3D) dust cloud. Due to the poor confinement at low pressure, the volume of the dust grain medium doesn't remain constant; therefore, an inductively coupled plasma (ICP) configuration is taken into account to create a potential well so that a constant large volume dusty plasma could be obtained. In the case of ICP configuration, particles are confined in a potential well created by inductively coupled diffused plasma. The levitation or confinement of these particles in both discharge configurations is the result of the action of various forces such as gravitational force, the electrostatic force due to the electric field, the repulsive Coulomb force among the like charged dust particles, ion drag force due to the streaming of ions relative to the dust particles, and friction force due to collision with the neutrals. Since, the dynamics of the particle is self–consistently linked to the background plasma parameters. Therefore, to track the dynamical changes of the dust medium, plasma parameters are measured using active diagnostics such as a single Langmuir probe, double probe and emissive probe in the absence of dust particles. For imaging the self–oscillatory motion of dust grains, a diode pumped solid state (DPSS) red laser, cylindrical lens, CCD camera, zoom lens, and high performance computer are utilized. The wavelength, frequency and phase velocity of the low frequency oscillations are obtained from the video images by using an imageJ software and MATLAB based software. In the case of vortex motion, Particle Image Velocimetry (PIV) analysis [21] is conducted on the still video images to measure the magnitude as well as the direction of the velocity vector (or flowing particles) in a given vertical plane of a dust cloud. The angular velocity of a rotating particle can also be measured using the PIV analysis technique. The dynamics of dust grain medium at low pressure is presented in the following experiments.

In the first set of experiments, a DC discharge plasma is produced by applying the voltage in the range of 300–500 V between the cathode and two anodes (both are grounded) at an argon of pressure of 0.07 mbar. A disk shaped electrode having a plane surface on one side and a step of 5 mm width and 2 mm height around its periphery on the other side is used as a cathode. The plane surface of the cathode is parallel to a stainless steel (SS) disk, which acts as an anode (lower anode) and is kept 10 cm below from the cathode. Another anode (upper anode) is a SS flange of 7 cm diameter and is kept parallel to the dust particles containing cathode surface at 15 cm above the cathode. This configuration of anodes and cathode demands minimum voltage to breakdown the argon gas. Both the anodes are kept grounded through a resistance of $R = 100\ \Omega$ to measure the discharge current in each path. At first, plasma is formed in between the cathode and lower anode at about 320 V and later it strikes between the cathode and upper anode. As plasma density crosses a critical limit, dust particles on the cathode surface (sprinkled on the surface before the production of plasma) get negatively charged and are levitated at the plasma–sheath boundary. These particles are horizontally confined due to an inward component of the radial electrostatic field of the sheath formed around the ring at its periphery balancing the repulsive Coulomb force among the charged particles. The vertical levitation of the dust particle is primarily a consequence of the balance between the upward electrostatic force, F_E and the downward gravitational force, F_g. The role of other forces in an equilibrium condition is found to be smaller than the F_E and F_g at least by an order of magnitude. The levitated dust particles are organized into a three-dimensional (bowl shaped) cloud at ~ 40 mm above the cathode at the discharge voltage of 340 V and argon pressure of 0.07 mbar. At the applied voltage beyond 350 V, the particles start to oscillate about its equilibrium position and these oscillations are seen to propagate towards the cathode. At this discharge condition, streaming ions trigger these longitudinal dust cloud oscillations [22, 23] which consist of the alternating compression and rarefaction regions. Theses longitudinal low-frequency oscillations are classified as dust acoustic waves (DAWs) [24]. The measured wavelength and phase velocity are 1.5–2.5 mm and 2–3 cm/sec respectively, while the frequency is lying in the range of 10–15 Hz. After the characterization of DAWs, experiments are performed to study the modification of its propagation characteristics in the presence of electric perturbation, which is applied using a floating cylindrical object (rod) of radius (r) larger than the dust Debye length (λ_D). The floating rod is introduced into the plasma perpendicular to the cathode plane (vertical) and in the plane of cathode (horizontal). In the presence of a vertically aligned floating rod, the DAWs are disappeared in the perturbed region at discharge voltage $V_d \sim 380$–400 V whereas at higher discharge voltage (> 420 V), the DAWs are observed to propagate obliquely in the vertical plane. In the radial plane of the floating rod (horizontal plane), circular DAWs are found to originate at the outer edge of the perturbed region and propagate towards the rod surface. Interaction of the horizontally aligned rod provides the detailed information on the DAWs propagation modification with the discharge parameters. Keeping horizontal rod alignment unchanged, it is observed that dust cloud takes various shapes (concave or cone shape) depending on the position of the rod with respect to the levitated dust cloud. In the presence of a floating rod, sheath around it alters the potential contour (or electric field distribution) of the cathode sheath region because of the coupling of the sheaths formed around the cylindrical and the cathode [25]. As a consequence, the dust grains follow the modified equipotential surfaces to get an equilibrium position in the perturbed region. The direction of streaming ions also changes according to the resultant E–field, therefore, DAWs are found to propagate obliquely. This work has been published in (*Choudhary et al.) Physics of Plasmas 23, 083705 (2016).*

In the second set of experiments, a novel configuration using an inductively coupled diffused plasma to create large volume dusty plasma at low gas pressure is studied. Plasma is produced by passing high frequency (13.56 MHz) current through an inductive coil, which is wound around a glass tube (called source section). Plasma is produced in the source section and after that it diffuses into the experimental chamber. This diffused plasma provides an electrostatic confinement to the negatively charged dust grains. For injecting the dust grains into the potential well, a novel technique using the DC discharge plasma is employed. The dust grains are homogeneously sprinkled on the SS disk, which is kept fixed inside the experimental tube about 30 cm away from the source section. A negative DC voltage is applied to this disk for levitating the dust grains at plasma–sheath boundary. Due to the poor confinement, these particles come into plasma volume and are found to transport in an ambipolar E–field of diffused plasma. These transported particles are found to be confined in the electrostatic potential well, which is formed due to the diffused plasma (ambipolar E–field) and the charged glass wall (sheath E–field) [26]. These confined particles form a 3–dimensional (3D) dusty plasma and remains confined for longer time. One unique aspect of this device is that volume of the dust medium can be controlled precisely by changing the DC bias on the disc. In this configuration, an equilibrium dust grain medium is possible at low pressure ($\sim$ 0.01 mbar) and low rf power (2–4 W). The ambient plasma parameters are measured to estimate the forces acting on the charged particle to understand the dynamics of the dusty plasma. The transport and trapping of particles in a potential well created by inductively coupled diffused plasma are discussed by *Choudhary et al. Review of Scientific Instruments 87, 053505 (2016).*

In the third set of experiments, we have investigated self–oscillatory motion of the dust particles which are confined in an electrostatic potential well of the inductively coupled diffused plasma. It is observed that dust particles show the acoustic vibrations at the higher rf power (P $>$ 8 W) and particles set up into rotational motion below this power. The multiple co–rotating (anti–clockwise) dust vortices are observed in the dust cloud for a particular discharge condition (P = 7.5 W and p = 0.04 mbar). When rf power is lowered, transition from multiple to single dust vortex is observed. The PIV analysis is conducted on the still images to get the velocity distribution of particles in the vortex structure. It is observed that particles have non–uniform velocity distribution in a vortex structure. The occurrence of these vortices is explained on the basis of the charge gradient in the dust column orthogonal to the ion drag force [27]. This charge gradient is a consequence of the plasma inhomogeneity along the axis of dust cloud. The vortex structure has a characteristic size in the dusty plasma so that multiple vortices could be formed in an extended dust cloud with inhomogeneous plasma background. The experimental results on the vortex motion of particles are compared to an available theoretical model [27, 28] and are found to be in good agreement. A manuscript with experimental observations of self excited co–rotating multiple vortices in a dusty plasma with inhomogeneous plasma background is *accepted* for publication in *(Choudhary et al.) Physics of Plasmas, March (2017).*

This thesis addresses novel configuration to create a large volume dusty plasma at low pressure, characteristics of the collective modes with an external potential perturbation, and origin of the co–rotating vortices in a large volume dusty plasma medium. The thesis is organized in the following manner.

Chapter-1: *Introduction.* In this chapter, introduction about the dusty plasma and its occurrence in space and laboratory plasmas are discussed. Basic fundamental properties of dusty plasma, forces acting on dust particle in the plasma, and various configurations to create laboratory dusty plasma are discussed. Also, review of earlier works on the collective modes of dusty plasma and motivation behind the this research work are presented in this chapter.

Chapter-2: *Experimental Setup and Diagnostics.* In this chapter, the experimental setup developed for the study of collective phenomena (waves and vortices) in dusty plasma is presented. A detailed description of vacuum chambers, power supplies, pumping system, cathode and anode design are provided. Experimental configuration to produce the plasma and dusty plasma in both DC and RF (inductively coupled) discharges are presented. Design and operation principle of the various electrostatic probes to diagnose the plasma are discussed in detail. At the end of this chapter, imaging techniques and image analysis using various softwares are discussed.

Chapter-3: *Dust Acoustic Wave and its Propagation Characteristic in Presence of a Floating Object.* This chapter contains the experimental results of dust acoustic waves and its propagation modification by a floating cylindrical object. The chapter begins with the introduction about the dust acoustic wave and its study in various dusty devices. Characterization of plasma and dusty plasma at various discharge parameters are presented. Excitation of dust acoustic waves and its dispersion relation are presented. The interaction of the floating cylindrical rod, which is aligned either vertically or horizontally, with the propagating dust acoustic waves is discussed in detail. The qualitative explanations to understand the oblique nature of the dust acoustic waves in the perturbed region are given. The work is summarized at the end of this chapter.

Chapter-4: *Transport and Trapping of Dust Particles in Diffused Plasma.* In this chapter, transport and trapping of dust particles in a potential well created by inductively coupled diffused plasma are discussed in detail. At the beginning of the chapter, various configurations either in DC or RF discharge is used to confine the dust grains are highlighted. Description of the experimental configuration along with the coordinate representation is provided. Characterization of diffused plasma using electrostatic probes to understand the transport and trapping of particles is described. Calculations of forces acting on the particles to describe the transport and confinement in the diffused plasma are given. The dynamical behavior of the dusty plasma at different discharge conditions is highlighted. Brief summary of the work is given at the end of this chapter.

Chapter-5: *Multiple Co–rotating Vortex Structures.* In this chapter, the results on the origin of multiple co–rotating vortices are discussed. Introduction about the particle rotation in the absence and presence of a magnetic field is highlighted. Experimental configuration to study the self–oscillatory motion of dust particles at various discharge conditions is highlighted. Formation of multiple co–rotating vortices, transition from multiple to single vortex, and particle velocity distribution in a vortex structure are discussed in detail. The quantitative analysis to describe the origin of vortex flow and its multiplicity are discussed with the theoretical model. Summary of presenting work is discussed at the end of this chapter.

Chapter-6: *Conclusion and Future Scope.* This chapter summarizes the major findings of this thesis work, and concludes with a broad outlook for future studies.

List of Figures

1.1 (a) A view of the nearly radial spokes in Saturn's B ring. (Courtesy of Jet Propulsion Laboratory). (b) A view of comets tail showing two distinct tails, namely a thin blue plasma tail and a broad white dust tail (`http://burro.astr.cwru.edu/Academics/Astr221/SolarSys/Comets/west.gif`). (c) A view of the Eagle nebula (`http://www.spacewallpapers.net/wallpapers/albums/Nebula/normal_n7.jpg`). (d) Image of Noctilucent Cloud (NCL) taken during summer at 85 altitude (`http://www.albany.edu/faculty/rgk/atm101/nlc18.jpg`) . . . 4

1.2 (a) Illuminated dust particles (greenish) floating above silicon wafers (Selwyn *et al.* J. Vac. Sci. 1990). (b) Metallic particles with carbonaceous coating from TEXTOR (J. Winter, Phys.Plasmas 2000). 6

1.3 A schematic of charging processes of a dust grain in the ambient plasma. . . . 12

1.4 Schematic diagram illustrating the forces acting on the dust particles during the confinement in an electrostatic potential well. An Arrow indicates the direction of force acting on dust grain. T_1 and T_2 denote the temperatures of neutrals with $T_1 > T_2$. . . . 19

1.5 Schematic representation of the methods used for producing dusty plasma in the laboratory experiments. . . . 20

2.1 (a) Experimental Setup: A1 and A2 indicate the axial ports of the experimental tube. P1 to P7 represent the radial ports of the experimental chamber. (1) Glass chamber, (2) CCD camera, (3) Pirani guage, (4) SS tube for connecting both chambers, (5) gas inlet through needle valve, (6) buffer chamber, (7) gas outlet through rotary pump, (8) Cylindrical lens, and (9) Laser. (b) 3D view of the experimental setup. . . . 30

2.2 Photographs of the cathode and anode used to produce the DC glow discharge plasma. . . . 31

2.3 Schematic diagram of power supply used for characterizing the plasma using a Langmuir probe (i.e., Langmuir probe power supply). . . . 33

2.4 Schematic diagram for producing the DC glow discharge plasma: (1) Upper anode, (2) cathode, (3) lower anode, and (4) high voltage DC power supply. 35
2.5 Paschen breakdown (pd) curve for argon gas. 36
2.6 Current–voltage ($I_d - V_d$) characteristics of the DC glow discharge at argon pressure of 0.07 mbar. 37
2.7 Schematic diagram of the single Langmuir probe. 40
2.8 I–V characteristic of the single Langmuir probe. 41
2.9 Plot shows an extrapolated ion current. 43
2.10 Semilog plot of the electron current collected by the Langmuir probe. 43
2.11 Schematic diagram of the double Langmuir probe. 45
2.12 Schematic representation of the flowing current in the double probe circuit. 46
2.13 I–V characteristic of the double probe. 47
2.14 Schematic diagram of the emissive probe. 48
2.15 The variation of floating potential of the emissive probe with the heating current. 49

3.1 (a) Schematic diagram of experimental configuration:(1) Cylindrical rod, (2) stainless steel(SS) flange (working as an anode), (3) solid-state red laser, (4) plano-convex cylindrical lens, (5) kaolin dust particles, (6) SS disk electrode (cathode) with a ring like step at corner (represented by yellow ring), (7) CCD camera, (8) stainless steel circular electrode (anode), (9) discharge power supply. I_{d1} and I_{d2} represent the currents flowing in separate discharge path. (b) A full view image of the dust cloud with a cathode and anodes. 58
3.2 Variation of plasma density (n) and electron temperature (T_e) with the discharge voltage. The argon gas pressure is set to 0.07 mbar during the measurements. 60
3.3 Variation of sheath thickness (solid rectangle) and dust cloud width (closed circle) with applied discharge voltages. The argon filling pressure during the experiment is set at 0.07 mbar. 62

3.4 (a) Video image of dust acoustic waves in the vertical (Y−Z) plane. (b) Average intensity profile of scattered laser light coming from dust particles (in dotted region) in -$\hat{z}$ direction. The direction of the wave propagation is indicated by the arrow. The data are taken at a discharge voltage and gas pressure of 370 V and 0.07 mbar, respectively. 66

3.5 Time evolution of intensity profile of five video frames taken at time step of 15.2 ms in the vertical plane. Discharge voltage and argon pressure are set at 370 V and 0.07 mbar respectively for this particular set of experiments 67

3.6 A video image of dust acoustic waves in presence of a vertically aligned floating rod. Three distinct regions are observed: (I) Dust void (dotted curve). (II) Stationary dust cloud (region between dotted curve and lines). (III). dust acoustic wave (outside the dotted lines). Argon pressure and discharge voltage are set at 0.07 mbar and 380 V, respectively. 69

3.7 (a) A video image of dust acoustic waves in vertical plane (in absence of rod).(b) Image of modified DAWs in vertical (Y–Z) plane with floating rod where discharge voltage is 470 V. (c) A video image of DAWs in horizontal (radial plane of rod) plane just below the floating rod. The direction of propagation in each sub-figure is shown by the arrow. 70

3.8 Video images of dust acoustic waves with floating rod in horizontal plane: (a) – (d) for discharge voltage (V_d) 400, 430, 490, and 520 V, respectively. The argon gas pressure is set at 0.07 mbar during the measurements. The yellow dotted circles represent the front of the floating rod. Green arrow indicates the direction of the propagating DAWs. 73

3.9 Video images of DAWs with floating rod at various locations in the sheath region: (a) rod is near the edge of sheath. (b) inside the sheath region where dust particles are levitated. (c) below the lower edge of levitated dust cloud. (d) near the cathode surface. The yellow dotted circles represent the front of rod in X-Y plane. The position of floating rod is measured with respect to the cathode surface. The error in measured value of rod position is ∓ 3 mm. Discharge voltage and pressure are set at 410 V and 0.07 mbar for these set of experiments. 75

4.1 (a) 3D view of experimental setup: (1) Left axial port, (2) experimental chamber, (3) SS rod for holding the dust containing disk, (4) dust containing disk (dust reservoir), (5) right axial port, (6) gas feeding valve (attached to buffer chamber), (7) buffer chamber, (8) rotary pump, (9) ICP plasma source tube and (10) inductive coil. (b) Schematic diagram of inductively coupled dusty plasma device (Top view). 83

4.2 (a) A typical plasma glow in the Y–Z plane. The yellow line represents the boundary of glow region. (b) The plasma glow profile in the X–Y plane. The white line indicates the boundary of glow region in this plane. Vertical yellow lines represent the different vertical positions for given a X–value. Argon pressure and input rf power are 0.05 mbar and 10 W, respectively. 84

4.3 Plasma density (n) and electron temperature (T_e) profiles: (a) along the Z–axis of the experimental chamber (at X≈ 0 cm and Y≈ 0 cm). (b) along the Y–axis (at X ≈ 0 cm and Z ∼ 12 cm). (c) along the X–axis (at Y ≈ -2 cm and Z ∼ 12 cm. Argon pressure and rf power are 0.05 mbar and 10 W, respectively. The errors in the measured values of n and T_e are within ± $3{\times}10^7 cm^{-3}$ and ± 0.3 eV, respectively. 87

4.4 Plasma potential profiles along the axis of experimental chamber at X $\approx$ 0 cm and Y $\approx$ -3 cm for different disk bias voltages. The measurements are taken in the absence of dust grains at an argon pressure of 0.05 mbar and rf power of 10 W. The dotted line represents the central region where dust particles get confined during the transport. The measurement errors are within $\pm$ 5%. 88

4.5 Axial plasma potential profiles of the diffused plasma for (a) two different gas pressures p = 0.05 and 0.025 mbar at a fixed rf power P = 10 W and (b) two different rf powers P = 10 and 13 W at a fixed gas pressures, p = 0.025 mbar. The measurements are taken after switching off the DC plasma. The black and green dotted lines (in Fig. 4.5(a)) represent the center of the potential well at 0.05 and 0.025 mbar, respectively. The errors in the measured value of plasma potential are within $\pm$ 5%. 89

4.6 Plasma potential variation along the direction of gravity (along Y–direction) for different X locations at Z $\sim$ 12 cm. The experiments are performed in argon gas at pressure, p = 0.05 mbar and rf power, P = 10 W. The dust cloud lies between the dotted lines. The errors in the measured plasma potential are within $\pm$ 5%. 90

4.7 Plasma potential variation along the axis of source tube (along X–direction) for different Y locations (Y = -2 cm, -4 cm, and -6 cm) at Z $\sim$ 12 cm. The experiments are performed in argon gas at pressure, p = 0.05 mbar and rf power, P = 10 W. The dust cloud lies between the dotted lines. The measurement errors are within $\pm$ 5%. 91

4.8 (a) PIV analysis shows the flow of particles toward the central region (Z $\sim$ 12 cm) when the dust reservoir is biased to -450 V. The direction of arrows indicates the dust particles flow, whereas length corresponds to the magnitude of the velocity vector. The white spots in the image correspond to the flowing kaolin particles. (b) The particle velocity profiles in two directions (Z and Y–directions). During the flow argon pressure and input power are 0.05 mbar and 10 W, respectively. 93

4.9 A snapshot of dust particles distribution in X–Z plane near the center of source tube (at Y ≈ -4 cm). The bright points correspond to the dust particles. Kaolin particles with average radius of ∼ 3 μm are used in this experiment. Input rf power and argon pressure is set to 7 W and 0.06 mbar, respectively. The field of view of an image is 8.94 mm × 2.8 mm 97

4.10 A single video frame of the dust cloud in Y–Z plane near the central region (at X ≈ -2 cm) shows the breaking and merging of dust acoustic wave at pressure p = 0.06 mbar and rf power P = 10 W. For this experiment, kaolin particles of average size ($r_d \sim 3$ μm) are used. The field of view of an image is 46.8 mm × 25.6 mm. 97

5.1 (a) Schematic of experimental configuration (top view). (b) A snapshot of the diffused plasma in the X–Y plane at Z ∼ 12 cm when gas pressure and input power are set to 0.04 mbar and 6 W, respectively. The white closed loop represents the boundary of the left axial port (A1) and the yellow dotted line represents the boundary of the diffused plasma. Confined dust particles at the edge of the glow are indicated by white spots. (c) A full view image of the confined dust cloud in the X–Y plane near the center of source tube (Z ∼ 12 cm). The yellow line with arrow indicates the direction of the rotating particles in the X–Y plane. The circular arc (due to the reflected light) indicates the inner boundary of glass chamber. The position of the dust cloud can be determined by using the reference of yellow dotted lines. The green dotted lines represent the typical measurement axes (along X and Y axis) for a given X and Y values. The yellow dashed line represents the typical axis of the confined dust cloud in this plane. 103

5.2 Video images of the dust cloud in the X–Y plane at Z $\sim$ 12 cm. Images ((a) – (c)) are obtained by the superposition of five consecutive images at a time interval of 66 ms. Fig.5.2(a)–Fig.5.2(c) are observed vortex structures at different input rf power (P) 7.5 W, 6.3 W and 5.1 W, respectively. The yellow solid lines with an arrow indicate the direction of vortex motion of dust grains and dashed line corresponds to the axis of the dust cloud. The vortex representation (I, II, and III) are made based on the number notation from the outer edge of the dust cloud. Kaolin particles are used to perform the dusty plasma experiments at argon pressure 0.04 mbar. 105

5.3 Images show the velocity distribution of dust particles in a vortex structure at different input rf powers (Fig.5.2). Images (Fig.5.3 (a)–Fig.5.3(c)) are obtained after PIV analysis of the corresponding still images. Velocity vectors are showing the direction of the rotating particles in X–Y plane at Z $\sim$ 12 cm. Color bar on the images show the value of dust velocity in mm/sec. Three anti–clockwise co–rotating dust vortices are observed in the extended dust cloud at P = 7.5 W (Fig.5.3(a)). Dust cloud supports only two co–rotating vortices when input power is 6.3 W (Fig.5.3(b)). A single anti–clockwise dust vortex is observed at power of 5.1 W (Fig.5.3(c)). All the measurements are taken at fixed gas pressure of 0.04 mbar . 106

5.4 Radial variation of speed of particle and angular velocity for Vortex-I (Fig. 5.2(b)) at P = 6.3 W and p = 0.04 mbar. Here, r = 0 mm corresponds to X = -2.1 cm, Y = -3.7 cm and r = 6 mm corresponds to X = -1.5 cm, Y = -3.7 cm. Errors in the measured values are within 10%. 107

5.5 Video images of the dust cloud in different X–Y planes. All the images are obtained by the superposition of five consecutive images at a time interval of 66 ms. Fig.5.5(a)–Fig.5.5(c) corresponds to Z = 10 cm, Z = 13 cm and Z = 16 cm, respectively. Yellow lines with an arrow indicate the direction of the rotating particles in the extended cloud. The measurements are taken at fixed gas pressure 0.04 mbar and input rf power 7.5 W. 108

5.6 Video image of dust cloud in a X–Y plane with direction of charge gradient (β) and the ion drag force (F_I). The direction of rotation is represented by a yellow line with arrow. Dust grains rotate in the direction of the gradient of dust charge. 111
5.7 (a) Electron temperature (T_e) variation along the X–axis at Y $\approx$ -3 cm and Z $\sim$ 12 cm for two rf powers, P = 6.3 W and 5.1 W. (b) T_e variation along Y–axis at X $\approx$ -4 cm and Z $\sim$ 12 cm for two rf powers, P = 7.5 W and 6.3 W. All the measurements are taken in the absence of the dust particles at gas pressure, p = 0.04 mbar. . . 112
5.8 (a) Plasma density (n) variation along X–axis at Y $\approx$ -3 cm and Z $\sim$ 12 cm for two rf powers, P = 6.3 W and 5.1 W. (b) plasma density variation along Y–axis at X $\approx$ -3 cm and Z $\sim$ 12 cm for two rf powers, P = 7.5 W and 6.3 W. All the measurements are taken in the absence of the dust particles at gas pressure, p = 0.04 mbar. 113
5.9 (a) Electron temperature (T_e) and (b) plasma density (n) variations along the axis of confined dust cloud at rf powers of 7.5 W and 6.3 W. All the measurements are taken in the absence of the dust particles at gas pressure, p = 0.04 mbar 115
5.10 (a) Plasma potential profile along the X–axis at Y $\approx$ -4 cm and Z $\sim$ 12 cm (b) along the Y–axis at X $\approx$ -4 cm and Z $\sim$ 12 cm for different rf powers. The plasma potential measurements are taken with an emissive probe using floating point method. The argon pressure is kept fixed at 0.04 mbar during the experiments. Errors in the measured value of plasma potential are within $\pm$ 2 V. 116

6.1 A schematic of the experimental setup to produce large aspect ratio (or large volume) dusty plasma at low pressure. 125
6.2 Plasma potential profiles: (a) along Z–axis for Y $\approx$ -4 cm and X $\approx$ 0 cm. (b) along Y–axis for Z $\approx$ 30 cm and X $\approx$ 0 cm. (c) along X–axis for Y $\approx$ -3 cm and Z $\approx$ 30 cm. All the measurements are taken in absence of dust particles at P = 9 W and p = 0.04 mbar. The errors in the measured value of plasma potential are $\pm$ 2 V . . 127

6.3 A video image of the dust cloud in the Y–Z plane at X $\sim$ 0 cm. The experiment is performed with kaolin particles at P = 8 W and p = 0.06 mbar. 127
6.4 A video image of the dust cloud in the X–Y plane at Z $\sim$ 30 cm. Experiment is performed with kaolin particles at P = 6 W and p = 0.03 mbar. The yellow curved lines with an arrow indicate the direction of dust grain rotation. 128
6.5 Transient electron energy distribution function (EEDF) for pulse width of 10 μs and amplitude U_p = 1020 V at 8 cm far away from an exciter. The argon gas pressure was 0.001 mbar. 131

List of Tables

2.1 Specifications of the DPSS Laser. 50
2.2 Specifications of the cylindrical lens. 50
2.3 Specifications of the CMOS and CCD cameras. 51

3.1 Dust acoustic wave characteristics without and with the rod orientations for fixed pressure p = 0.07 mbar and varying discharge voltages. 74

1

Introduction

The purpose of this chapter is to provide an introduction to the subject of dusty plasma. The definition of the dusty plasma, its formation, different examples of its existence in nature, solar system, atmospheric environments, processing plasmas, fusion devices etc., and the importance of the research in the field of dusty plasma is highlighted in Sec. 1.1. Some key features of dusty plasma and its applicability as a model for understanding various phenomena of matters at kinetic level is presented in Sec. 1.2. Sec. 1.3 discusses the fundamental properties of the dusty plasma. The forces acting on the dust grain in the plasma background is discussed in Sec. 1.4. Various electrostatic traps used for dusty plasma formation is presented in Sec. 1.5. Overview of the previous work is highlighted in Sec. 1.6. The motivation behind the research work carried out in this thesis is highlighted in Sec. 1.7. The scope and structure of the thesis is presented in Sec. 1.8.

1.1 Introduction

This section provides the introduction to dusty and its existence in the various universal systems (Saturn ring, comet tails, nebulas, noctilucent cloud etc.) and laboratory plasmas (processing plasmas and tokamak plasmas). It also highlights the importance of this research field to understand the various phenomena in natural occurring plasmas and man made plasmas.

1.1.1 Dusty plasma

An ionized gas consists of negatively charged electrons and positively charged ions in which these charge particles are not free but strongly affected by each other's electromagnetic field and are capable to exhibit the collective motions. Such gas was named as "plasma" by Irving Langmuir in 1929 with his colleague Lewi Tonks [29]. Sometime it is called as fourth state of matter after solid, liquid, and gas. There will also be a fraction of the neutrals in the plasma if the gas is not fully ionized. Plasmas resulting from ionization of neutral gases generally contain equal numbers of positive and negative charge carriers, such plasmas are termed as quasi-neutral. It is believed that that 99 % of the observable matter in our universe is in the plasma state [30, 31], while remaining 1 % representing other matters such as planets and dust particles. The presence of small particles of solid matter, called dust, in the plasma undergo frequent collisions with electrons and ions and acquire the large amount of charge on its surface. The admixture of the electrons, ions and charged dust particles (fraction of μm to tens of μm) are termed as "dusty plasma". In last couple of decades, dusty plasma research has has become an area of keen interest. The initial motivation to drive the research in the field of dusty plasma was primarily due to two main fields: astronomy and industry. Later, dusty plasmas have proven to be a model system for studying the various properties of fluids and solids at microscopic level. This subsection presents some popular examples of astrophysical and laboratory plasmas where dust is ubiquitous ingredient of the plasma.

1.1.2 Dusty plasma in universe and atmosphere

The presence of dust particles in the various astrophysical plasmas has been demonstrated through the remote observations taken by the various space crafts. In the early of 1980's, the images of Saturn's rings were taken by Voyager 1 and Voyager 2, which showed "spokes" moving on the B–ring. Later it was realized that the "spokes in B–ring" most likely were tiny specks of dust moving around the rings [32–35]. The presence of "spokes" in the Saturn's B-ring is shown in Fig. 1.1(a). The formation and evolution of spokes in the Saturn's rings have been explained by various research groups [36–40]. Similar to the Saturn's ring, most of the rings of the Jupiter, Uranus, and Neptune are made of microscopic dust grains [41, 42]. The dust particles were also found in interplanetary space and comets. The interplanetary dust, which is mainly composed of carbonaceous grains, mainly forms the comets and asteroids. The "Comets tail" is an example, which represents the dust grains in the solar system. As a comet approaches the sun, part of comet's ice converts into vapor (tiny dust grains), engulfs the comet nucleus to form a coma. The solar wind (plasma) pushes the cometary coma away from the sun and forms a "cometary dust tail" [43, 44]. An image of "comets tail" is displayed in Fig. 1.1(b). The interstellar medium, materials between the stars, also are composed of interstellar gas and dust. The size of interstellar dust particles is of the order of micron sized. Various things can happen in the presence of dust clouds like blocking of light (dark nebula), the scattering of favorable light (Egg nebula), and reflection of light (reflection nebula). An image of "Eagle nebula" (see Fig. 1.1(c)) again clearly shows the presence of dust cloud [45, 46] in the solar system.

Apart from the solar systems, dust environment is detected in the Earth's atmosphere (in the lower part of the ionosphere). One of the interesting examples is the formation of noctilucent cloud, which is observed in polar regions in summer at 85 km altitude [47,48]. They are made of small ice crystals (0.1 μm in diameter). Fig. 1.1(d) shows an image of noctilucent cloud taken during the summer.

A wide spectrum of the dust environment in the matters of the universe (interplanetary space, interstellar medium, comets, planetary rings, earth atmospheres, etc.) has attracted the scientists to understand the mystery of unusual phenomena happening in the universe. It is obvious that images or data obtained from the natural dusty plasma can give a limited amount of information; therefore, detailed studies of space dust medium are only possible in the controlled laboratory experiments. Various aspects of the universal (natural occurring) dusty plasma such as dust–plasma interaction both on earth and in space, mysterious dark spokes of Saturn's B-rings, collapse of interstellar clouds, periodic burst of submicron sized dust particles (dust streams) ejected from Jupiter, formation of planets, dust collisional fragmentation and vaporization, interaction of streaming dust channels, charging mechanisms of dust of various sizes and shapes, collisions of dust grains with targets, driven and self–generated instabilities in the dust medium etc. [43–45, 49–51] have created the worldwide interest to study the dusty plasma in laboratory experiments.

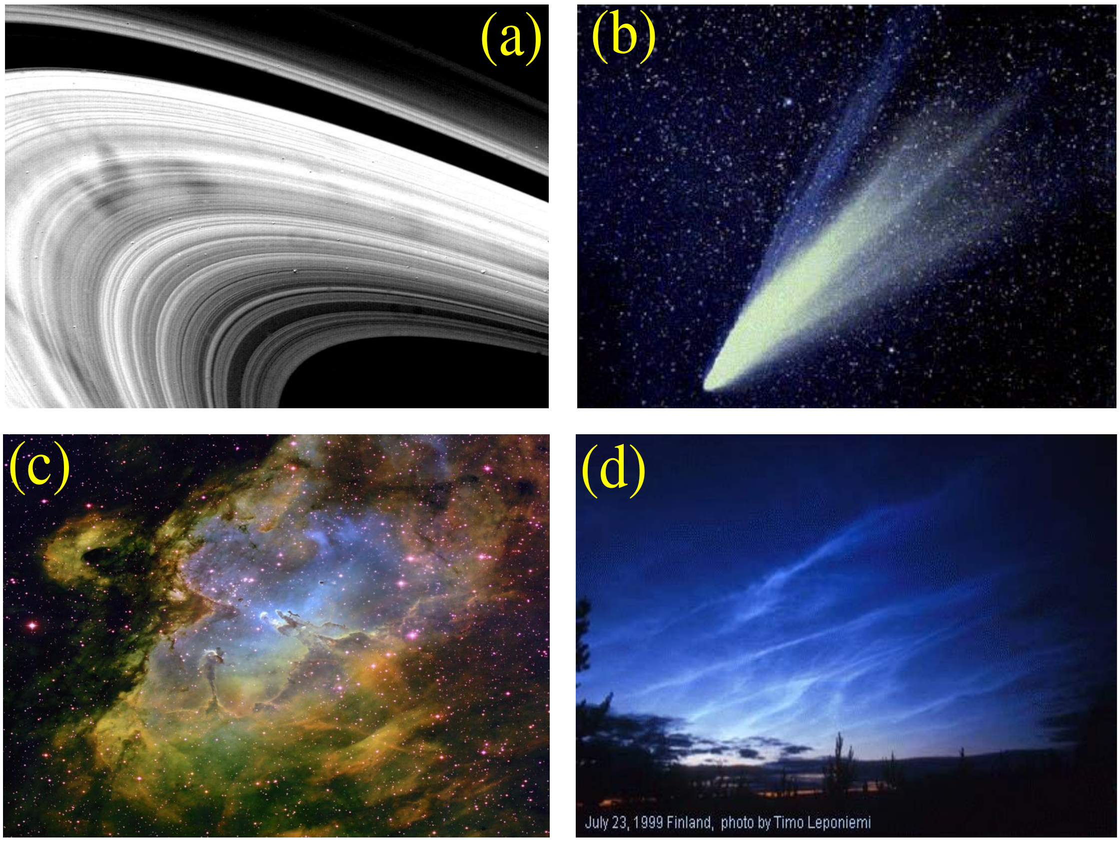

Figure 1.1: (a) A view of the nearly radial spokes in Saturn's B ring. (Courtesy of Jet Propulsion Laboratory). (b) A view of comets tail showing two distinct tails, namely a thin blue plasma tail and a broad white dust tail (http://burro.astr.cwru.edu/Academics/Astr221/SolarSys/Comets/west.gif). (c) A view of the Eagle nebula (http://www.spacewallpapers.net/wallpapers/albums/Nebula/normal_n7.jpg). (d) Image of Noctilucent Cloud (NCL) taken during summer at 85 altitude (http://www.albany.edu/faculty/rgk/atm101/nlc18.jpg)

1.1.3 Dusty plasma in laboratory

In 1991, Selwyn observed the cloud of dust particles over the substrate during the plasma processing [52], which is depicted in Fig. 1.2 (a). Afterward, the interest in the dusty plasma has been emerged in the research related to industrial and technological applications. These particles are either grown by chemical process or ejected from the substrate during the etching process. It was realized that formation of the dust particles in semiconductor fabrication, etching, deposition, sputtering of thin films and microelectronics productions reduce the product quality. For controlling the plasma processes, it is necessary to understand the influence of the dust on the plasma parameters, particles growth phenomena, and transport mechanism of charged dust grains etc. In recent years, studies on the physics of particles formation and growth, particles transport and trapping mechanism, and control over the substrate contaminations have been attractive topics for the dusty plasma community [53–56].

At the same time, some positive aspects of the dusty plasma have been investigated. For instance, performance of solar cell can be substantially improved by incorporating nanometer sized particles in silicon wafer [57] and the presence of dust grains can increase the deposition rate in dust-plasma-enhanced chemical vapor deposition process [54]. This short history of industrial applications of dusty plasma research have attracted attention to understand the dust–induced problems in the material processing technologies.

Also, in last decades, dust particles (few nm to few tens of micron) were found in the bottom of the most of tokamaks and stellarators during the operation [58–61]. An image of dust grains collected from tokamak plasma is depicted in Fig. 1.2(b). Dust in the fusion devices, for instance, International Thermonuclear Experimental Reactor (ITER), is regarded as a potential safety hazard. A wide spectrum of work on dust generation processes, the composition of dust particles, size distribution, surface area, and the total quantity of dust produced have been done to reduce the general hazards of dust [62–64]. Thus, the problem of dust removal from the fusion devices is one of the most important scientific and technical issue. The presence of dust particles ranging from solar systems to fusion devices have created an interest in study of dusty plasma. Hence, currently theoretical, numerical and experimental efforts are being made to understand the behavior of dusty plasmas.

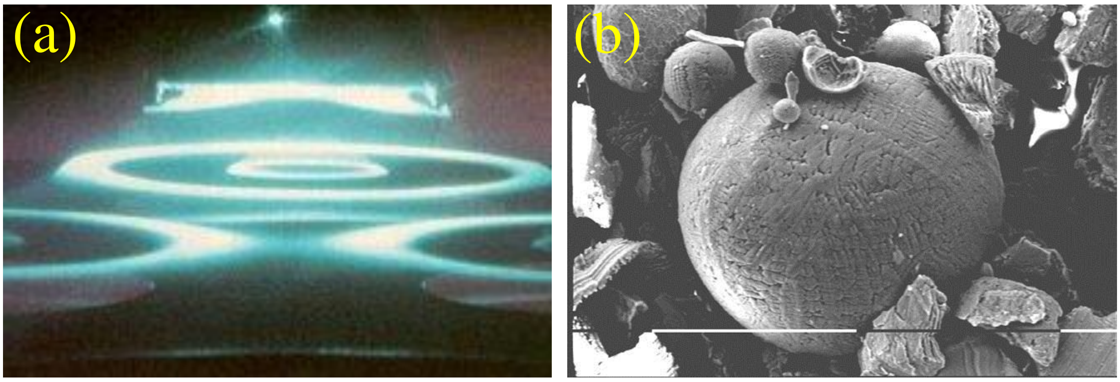

Figure 1.2: (a) Illuminated dust particles (greenish) floating above silicon wafers (Selwyn *et al.* J. Vac. Sci. 1990). (b) Metallic particles with carbonaceous coating from TEXTOR (J. Winter, Phys.Plasmas 2000).

1.2 Key features of laboratory dusty plasma

Dust grains (sub–micron to micron sized) either in space or laboratory plasma acquire an equilibrium charge of the order of $10^3 - 10^5$ times electronic charge [65,66]. The charging mechanism of dust particles involves the collection of electron and ion currents, photoelectron emission by UV radiation, secondary electron emission by highly energetic electrons or ions [43,67,68]. It is to be noted that comparative value of collection currents and emission currents on the surface of dust grains determines the polarity of the dust charge. In the laboratory plasma, where emission processes are unimportant, dust grains always get negatively charged because of the higher electron flux to the dust surface compared to that of ions. On the other hand, when emission processes are significant (due to the UV and cosmic radiations), dust grains are probably positively charged. This is the case in the space plasma, where positively charged dust grains are expected because of the higher emission processes. At first, the charge on dust was considered constant because of the continuous charging processes [69]. Later, charge fluctuations due to discrete currents on the dust surface were predicated [68]. It means the dust charge becomes a time–dependent quantity and can be treated as a dynamical variable, which is coupled self–consistently to other dynamical variables of plasma. The coupling of this additional degree of freedom available to the dusty plasma can lead to various collective phenomena [70].

The dusty plasma has some remarkable features to differentiate from conventional two-component plasma. Firstly, an extremely small charges-to-mass ratio which leads to new plasma eigenmodes at very low frequency ($<$ 100 Hz) [71]. The dust dynamics at such low frequency can be visualized even with naked eyes, which allows us to study the medium characteristics at the microscopic level. Secondly, a large amount of charges on dust grains substantially increases the average potential energy of the dust component compared to its average kinetic energy, which leads the medium to strongly coupled state with liquid-like and solid-like characteristics [72–76]. The coupling parameter (Γ), a ratio of the potential energy to the kinetic energy, determines the physical state of the dust grain medium. Above a critical value of the coupling parameter, $\Gamma_c \sim 170$, dust grains are found to arrange in a crystalline state, called as "Coulomb crystal". These crystals are created in various experimental devices with various lattice configurations such as simple cubic, face-centered cubic, and body-centered cubic structures [73, 77, 78]. The phenomena associated with crystalline state such as melting of coulomb crystal [79, 80], vaporization of the crystalline state [81], phonon excitation in dusty crystal [82, 83] and pure transverse modes [84] have been demonstrated in laboratory experiments with controlled manners.

This medium, where phase transition and crystalline structure are so vividly observed even by naked eyes, is becoming a valuable tool for studying physical processes in condensed matter, such as melting, annealing and lattice defects. Hence, dusty plasma provides a platform to understand the underlying physics at microscopic levels for various multidisciplinary fields (e.g. solid state physics, fluid physics, and life sciences).

1.3 Fundamental properties of dusty plasma

Dust grains, either conducting or non-conducting, undergo frequent collisions with the highly mobile electrons and lumbering ions and get negatively charged. The presence of dust grains affects the dynamics of the ambient plasma species (electrons and ions). Furthermore, these massive charged particles also respond collectively due to the long-range Coulomb interaction. The micro-particles are large enough to be visualized individually which allows experimental investigations with high temporal and spatial resolution. Hence, the dusty plasma phenomena such as waves and instabilities, transport of particles, phase–transition, and vortex motion etc. can be studied at microscopic level. Before going to dusty plasma studies, the basic fundamental properties of the dust–plasma system need to be known. In this section, charging of dust grain, dust Debye length, dust characteristics frequency, Coulomb coupling constant, and forces acting on the dust grain are discussed.

1.3.1 Dust charging processes

When dust particles are exposed to plasma then dust grain acquires charges on its surface under the various charging processes: the collection of plasma species (electrons and ions) from surrounding plasma, photo–ionization due to the incident of UV radiation, secondary electron emission by energetic electrons or ions, and field emission. In most of the laboratory experiments, dust grain charging is dominated by the collection of plasma species rather than other processes. Other charging mechanisms (e.g. photo–ionization or secondary emission) are prominent in the environment of space plasma. The following are the charging processes:

1.3.1.1 Collection of charged species

When dust particles are introduced into the conventional two-component plasma, they are bathed in highly mobile electrons and slowly moving ions. The collision of highly mobile electrons makes its surface more negative, which reduces the coming electron flux and increases the ion flux to the charged surface for balancing both the fluxes. In this situation, both electron and ion currents incident at the dust surface have equal magnitude. And potential on the dust grain is equivalent to the floating potential. This is the case similar to the electrostatic probes used to characterize the plasma. Therefore, dust is considered as a small spherical probe in ambient plasma. For calculating the charging current I_j (j = e and i) to the dust particle carried by the plasma species j, Orbital Motion Limited (OML) [85, 86] approximation is used. This approach (OML) describes the dust charging processes subjected to various assumptions such as dust grain is considered isolated (e.g $\lambda_D << d$) in collisionless ($l_i >> \lambda_D$) plasma and radius of the dust grain (r_d) is small compared to the Debye screening length ($r_d << \lambda_D$). Here, l_i is the ion mean free path and λ_D is the Debye screening length. Assuming that electrons and ions obey the Maxwellian distribution and their streaming velocities (v_e and v_i) are much smaller than their respective thermal velocities (v_{Te} and v_{Ti}), the equilibrium electron and ion currents are expressed as [43,71]

$$I_e = -4\pi r_d^2 n_{e0} e \left(\frac{k_B T_e}{2\pi m_e}\right)^{1/2} exp\left(\frac{e\phi_d}{k_B T_e}\right), \tag{1.1}$$

$$I_i = 4\pi r_d^2 n_{i0} e \left(\frac{k_B T_i}{2\pi m_i}\right)^{1/2} \left(1 - \frac{e\phi_d}{k_B T_i}\right), \tag{1.2}$$

where n_{e0} and n_{i0} are the equilibrium electron and ion densities, T_e and T_i are the electron and ion temperatures, ϕ_d is the surface potential of dust grain, m_e and m_i are the electron and ion masses and k_B is Boltzman constant.

On the other hand, if the ion streaming velocity (v_i) is much larger than the ion thermal speed (v_{Ti}), then the approximate expression for the ion current is

$$I_i \simeq \pi r_d^2 e n_{i0} v_i \left(1 - \frac{2e\phi_d}{m_i v_i^2}\right). \tag{1.3}$$

The charge on the dust grain Q_d is determined using the expression

$$\frac{dQ_d}{dt} = I_e + I_i, \tag{1.4}$$

At an equilibrium, the net current flowing into the dust grain surface becomes zero. It can be expressed as

$$I_e + I_i = 0, \tag{1.5}$$

Using equations (1.1) and (1.2) in equation (1.5), we get the expression

$$1 - \frac{e\phi_d}{k_B T_i} = \left(\frac{T_e m_i}{T_i m_e}\right)^{1/2} exp\left(\frac{e\phi_d}{k_B T_e}\right) \frac{n_{e0}}{n_{i0}}, \tag{1.6}$$

which determines the surface potential ϕ_d of an isolated dust grain. Due to the higher mobility of the electrons compared to that of ions, the dust surface potential ϕ_d is negative, i.e., $\phi_d < 0$. The dust equilibrium charge Q_d is related to its surface potential by the dust grain capacitance C. The relation is expressed as, $Q_d = C\phi_d$. Here, C is the grain capacitance, which is equivalent to the capacitance of the charged spherical body, given by $C = 4\ \pi\epsilon_0 r_d \left(1 + \frac{r_d}{\lambda_D}\right)$ for $r_d << \lambda_D$. It should be noted that the OML approximation yields accurate values for dust charge when the electron and ions are collisionless (i.e., their respectively mean free paths are much larger compared to the plasma screening length). Thus, the

OML approximation is unable to describe the variation of the dust charge with the plasma collisionality. Khrapak *et al.* [87] found that magnitude of the dust charge is quite sensitive to the level of the ion collisionality. The collisions start to affect the ion flux to dust surface when the ratio of the mean free path (l_i) to the dust screen length (λ_D) is of the order of 10, i.e., $l_i/\lambda_D \geq 10$. In this collisional regime, the OML approximation provides an accurate value of the dust charge. The OML model for grains charge calculation applies to the case where the grains are sufficiently far apart, i.e., $\lambda_D << d$. On the other hand, when the spacing between the grains (d) is comparable to or less than λ_D, dust grains are closely packed. In this situation, the difference $\Phi = \phi_d - \phi_p$ between the dust surface potential (ϕ_d) and the plasma potential (ϕ_p) has a smaller magnitude than in the case with $d >> \lambda_D$, and consequently the equilibrium charge on the dust grain is smaller than that for an isolated grain. For the closely packed dust system, we replace ϕ_d in Eq. (1.6) by Φ and $n_{i0}/n_{e0} = (1 - Q_d n_{d0}/en_{e0})$ to obtain the variation of Φ against the ambient plasma density for a fixed dust density n_{d0}. The charge on an isolated grain has been experimentally investigated by Walch *et al.* [66] using the Faraday cup. Barken *et al.* [69, 88] have reported the results of laboratory experiments on the dust charging in plasma column. By varying the ratio d/λ_D, they experimentally demonstrated the predicted charge reduction [89, 90] in the case of closely packed dust grain medium.

1.3.1.2 Secondary electron emission

In the plasma, the embedded dust particles are exposed to electrons and ions with different energies. The bombardment of the energetic plasma particles can release secondary electron from the dust grain surface. The process of secondary electron emission can occur in two ways: (i) by electron impact (ii) by ion impact. During the interaction of energetic electrons/ions with a dust grain, it may undergo the following possible situations: (i) it may be scattered/reflected by the dust grain before it enters into the dust surface, (ii) it may enter into the dust and stick on the dust grain surface, (iii) it may enter into dust grain, interact with scattering center, and exchange a fraction or all of its energy to other electrons which in turn escape from the dust surface. It is to be noted that probability of secondary electron emission through the bombardment of energetic ions is comparatively higher than that of from energetic electrons. If the ions having kinetic energy below 1 kV approach the dust particle, they will be neutralized by the electrons which tunnel through the potential barrier of dust surface. The potential energy released in the neutralization of ions will excite additional electrons which can then be emitted from the dust surface. When the incident ions have energies above 10 kV, the secondary electron yield due to ion impact will be substantially larger than unity. Thus, secondary electron emission can leave the dust particles to be positively charged [43].

1.3.1.3 Photoemission

The flux of incident photons with energy ($h\nu$) larger than the photoelectric work function (W) of the dust grain may eject the electrons from the dust surface. The photoemission of electrons depends on (i) the wavelength (λ) of the incident photon, (ii) the surface area of the dust grain, and (iii) the properties of the dust grain material. This process makes the dust grain positively charged.

1.3.1.4 Thermionic emission

When the dust grains are heated to a high temperature, electrons may be thermionically emitted from the dust grain surface. In this process, dust grains get positively charged by losing the electrons. The thermionic emission may be induced by laser heating or thermal infrared (IR) heating or by hot filaments surrounding the dust grain. This process also makes dust grain positively charged.

1.3.1.5 Field emission

In some cases, the micron or submicron sized dust particles may acquire a very high negative (or positive) potential and emit electrons (or ions) from their surface under the influence of the strong electric field. It has been observed that onset of electron emission from the dust surface occurs when the applied electric field is in between 10^6 V cm^{-1} and 10^7 V cm^{-1}. In this process, dust grain potential is limited by the field emitted electrons for the negatively charged dust grain.

The schematic representation of the various dust charging processes is depicted in Fig. 1.3.

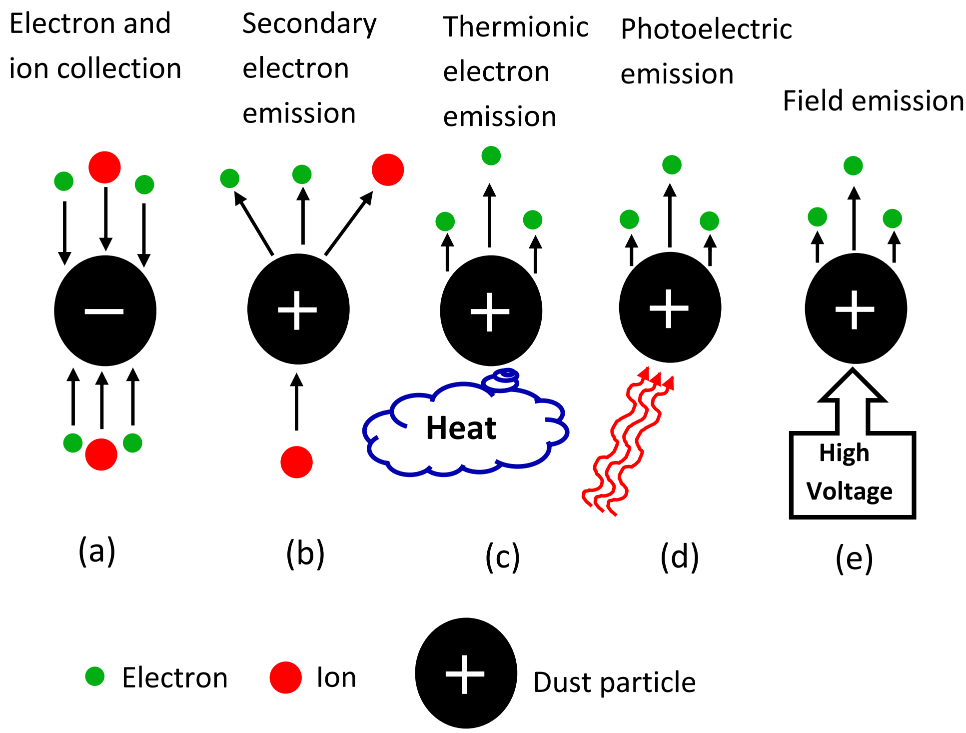

Figure 1.3: A schematic of charging processes of a dust grain in the ambient plasma.

1.3.2 Quasi–neutrality condition

The plasma always obeys the quasi-neutrality condition, i.e., $n_i \approx n_e$. It means that the plasma is macroscopically neutral. But neutrality may not be maintained over the microscopic scale. In an equilibrium, the quasi-neutrality condition is also satisfied in the dusty plasma. It essential means that in the absence of any external perturbation, the net resulting electric charge in the dusty plasma medium is zero. Therefore, an equilibrium charge neutrality condition in a dusty plasma is

$$Q_i n_{i0} = e n_{e0} + Q_d n_{d0}, \tag{1.7}$$

where n_{io}, n_{eo} and n_{do} are the unperturbed ion, electron and dust number density , Q_i $(= Z_i e)$ and Q_d $(=-Z_d e)$ are the ion and dust particle charge. After putting the values, Eq.(1.7) becomes

$$Z_i e n_{i0} = e n_{e0} + Z_d e n_{d0}, \tag{1.8}$$

where ion charge state $Z_i = 1$ and Z_d is the number of the charges residing on the dust grain surface, then Eq.(1.8) becomes

$$n_{i0} = n_{e0} + Z_d n_{d0}. \tag{1.9}$$

When most of the electrons from the plasma are attached to the dust particle surface, then we may have $Z_d n_{d0} >> n_{e0}$. In this case, Eq. (1.9) is replaced by

$$n_{i0} \approx Z_d n_{d0} \tag{1.10}$$

However, It should be noted that a complete depletion of the electrons is not possible [90] because the minimum value of the ratio n_{e0}/n_{i0} turns out to be $(m_e/m_i)^{1/2}$ when $T_e \approx T_i$ and $\phi_d \simeq 0$. In Eq. (1.10), the dusty plasma can be regarded as a two component plasma composed of negatively charged grains and ions. Such situations are met in the space as well in low-temperature plasma.

1.3.3 Debye shielding

A fundamental characteristic of a plasma is its ability to shield the electric field of an individual charged particle or of a surface that is at some non-zero potential. The Debye length is a distance over which the influence of the E-field of an individual charged particle (or of a surface that has non-zero potential) is experienced by other charged particles inside the plasma. This shielding of the E-field in the ambient plasma is well explained by Chen [91]. This Debye length (or screening length) inside a dusty plasma can be quite different than that is observed in electron-ion plasma. It can be formulated by taking an example of charged body in the dusty plasma. If a negatively charged ball is inserted in a dusty plasma, a cloud of ions and positively charged dust particles (if they are present) would surround it. If the plasma is cold then the E-field associated with negatively ball would be completely shielded. On the other hand, if temperature of the plasma species (T_e and T_i) is finite then E-field would leak outside the Debye length. For calculating the approximate sheath thickness (Debye length), the Poisson's equation is solved by assuming that the electrons and ions obey the Boltzman distribution [43]. For dusty plasma, the Debye length is expressed as

$$\frac{1}{\lambda_D^2} = \left(\frac{1}{\lambda_{De}^2} + \frac{1}{\lambda_{Di}^2} \right), \tag{1.11}$$

where $\lambda_{De} = (k_B T_e / 4\pi n_{e0} e^2)^{1/2}$ and $\lambda_{Di} = (k_B T_i / 4\pi n_{i0} e^2)^{1/2}$ are the electron and the ion Debye lengths, respectively. The simplified form of Eq.(1.11) is

$$\lambda_D = \frac{\lambda_{De}\lambda_{Di}}{\sqrt{\lambda_{De}^2 + \lambda_{Di}^2}}, \tag{1.12}$$

here λ_D measures the shielding or screening distance in the dusty plasma. In laboratory experiments, dust grains get negatively charged. In these cases, we have $n_{eo} << n_{i0}$ and $T_e > T_i$, i.e. $\lambda_{De} >> \lambda_{Di}$. Using this condition in Eq. (1.12), we have $\lambda_D \simeq \lambda_{Di}$. It means that shielding or screening length in dusty plasma is mainly determined by the temperature and number density of ions. However, for positively charged dust grain, shielding or screening length is determined by the temperature and density of the electrons.

1.3.4 Characteristic frequency

Similar to conventional two component plasma, dusty plasma also holds the macroscopic space charge neutrality. When the plasma particles are instantaneously displaced from their equilibrium position, a space charge field will be built up to restore the neutrality of the plasma by pulling the charged particles back to their equilibrium positions. But due to their inertia, they will overshoot and will be again pulled back to their equilibrium position by the space charge field of the opposite polarity. Thus, charged particles continuously oscillate around their equilibrium position due to the restoring force and inertial effect. The frequency of such oscillations are known as the plasma frequency, $\omega_{ps} = (4\pi n_{s0} Q_s^2 / m_s)^{1/2}$ associated with the plasma species, s. In the dust-plasma system, electrons oscillate with the electron plasma frequency $\omega_{pe} = (4\pi n_{e0} e^2 / m_e)^{1/2}$, ions oscillate with ion plasma frequency $\omega_{pi} = (4\pi n_{i0} e^2 / m_i)^{1/2}$, and dust grains oscillate with dust plasma frequency $\omega_{pd} = (4\pi n_{d0} Z_d^2 e^2 / m_d)^{1/2}$. In this thesis, we have used $m_d = M_d$ for representing the dust mass. The frequency of such oscillations depends on the mass and charge of the plasma species, which makes the difference of about a thousand times, i.e. $\omega_{pe} >> \omega_{pi} >> \omega_{pd}$. In a dusty plasma, collision frequencies of the charged species with the stationary neutrals are also important for the collective oscillations of the plasma particles. These collisions are characterized by the electron-neutral collision frequency, ν_{en}, the ion-neutral collision frequency, ν_{in}, and the dust-neutral collision frequency, ν_{dn}. The collision frequency for plasma species (electrons (e), ions (i), and dust grains (d)) is defined as

$$\nu_{sn} = n_n \sigma_s^n v_{Ts}, \tag{1.13}$$

where n_n is the neutral number density, σ_s^n is the effective collision cross–section and $v_{Ts} = (k_B T_s/m_s)^{1/2}$ is the thermal speed of the species s (= e, i, and d). The collective oscillations of the plasma particles are damped by the collisions with the neutrals. For studying the collective dynamics of the plasma particles, the collision frequency should be smaller than the plasma frequency, i.e. ν_{en}, ν_{in}, $\nu_{dn} < \omega_p$.

1.3.5 Coulomb coupling constant

In dusty plasma medium the interactions among the highly charged dust grains give rise to many new collective phenomena. The strength of the Coulomb interaction is determined by a coupling constant (Γ), which is defined as the ratio of the potential energy of the dust grains to their kinetic energy. For two dust grains separated by a distance d, having the charge Q_d $(= -Z_d e)$ and thermal temperature T_d, the Coulomb coupling constant is expressed as

$$\Gamma = \frac{Z_d^2 e^2}{d\ k_B T_d} exp\left(\frac{-d}{\lambda_D}\right). \tag{1.14}$$

The inter-particle distance d is related with dust number density (n_d) by $d = \left(\frac{3}{4\pi n_d}\right)^{1/3}$. The factor $exp\left(\frac{-d}{\lambda_D}\right)$ in the expression of Γ is due to the shielding or screening effect. This coupling constant determines the physical state of the dusty plasma medium. The dusty plasma is said to be in the crystalline state when $\Gamma >> 170$, in a liquid state when $1 << \Gamma << 170$, and in the gaseous state when $\Gamma << 1$. In other words, dusty plasma is weakly coupled system for $\Gamma << 1$ while it is strongly coupled for $\Gamma >> 1$. In many laboratory dusty plasma experiments, dust grains are found in a strongly coupled state because of their large electric charge on their surface, low temperature and small inter–particle distance [73, 74, 77, 78].

1.4 Forces acting on the dust grains

In a laboratory plasma, dynamics of the dust grain is governed by the various forces acting on it. These forces are electrostatic (or electromagnetic) force, gravitational force, ion and neutral drag forces, and thermophoretic force. In laboratory plasma, dust grains are confined in either a potential well or in the plasma sheath boundary under the action of these forces. The detailed description of these forces acting on a spherical, non-conducting and isolated dust grain with $r_d << \lambda_D$ is given in this section.

1.4.1 Gravitation force

This force comes into the picture when dust particles have finite mass. For a spherical dust grain of mass M_d , the gravitation force F_g is given by [43, 92]

$$\vec{F_g} = M_d\vec{g} = \frac{4}{3}\pi r_d^3 \rho_d \vec{g}, \tag{1.15}$$

where g is the acceleration of gravity, r_d is radius of dust grain and ρ_d is mass density of the dust grain.

1.4.2 Electrostatic force

Dust particles get negatively charged ($Q_d = -eZ_d$) in the laboratory plasma and experience an electrostatic force F_E due to the electric field E. The electrostatic force is given by [92]

$$\vec{F_E} = Q_d\vec{E} = -eZ_d\vec{E}, \tag{1.16}$$

where $\vec{E} = -\nabla\phi_p$ is the local E-field. It essentially means that this force is directed opposite to the E-field direction.

1.4.3 Ion drag force

The streaming ions in the electric field exert a force on the dust grains in two ways. Firstly, the ions transfer momentum to a dust particle through direct impacts, which is called collection force F_{ic}. Secondly, the ions transfer momentum through Coulomb collisions with the charged dust particle, which is called Coulomb or orbital force F_{io}. The magnitude of the ion drag force F_i is determined using the Barnes formula [92]. This formula is applied under the approximation $\lambda_D/l_i << 1$, where λ_D is the dust Debye (screening) length and l_i is ion mean free path. The dust Debye length is assumed to be $\lambda_D \sim \lambda_{Di}$. The collection force ($F_{ic}$) component is given by

$$F_{ic} = n_i v_s m_i v_i \pi b_c^2, \tag{1.17}$$

where n_i is plasma density and m_i is ion mass. The mean speed (v_s) is given by

$$v_s = \left(\frac{8k_B T_i}{\pi m_i} + v_i^2 \right). \tag{1.18}$$

The collection impact parameter is expressed as

$$b_c = r_d \left(1 - \frac{2q(\phi_d - \phi_p}{m_i v_s^2} \right)^{\frac{1}{2}}, \tag{1.19}$$

where ϕ_d is potential at the surface of the dust particles and ϕ_p is the plasma potential. The orbital force (F_{io}) is given by

$$F_{io} = n_i v_s m_i v_i 4\pi b_{\pi/2}^2 \Gamma, \tag{1.20}$$

where

$$b_{\pi/2}^2 = \frac{qQ_D}{4\pi\varepsilon_0 m_i v_s^2} \tag{1.21}$$

is the impact parameter whose asymptotic angle is $\pi/2$, and

$$\Gamma = \frac{1}{2} ln \left(\frac{\lambda_D^2 + b_{\pi/2}^2}{b_c^2 + b_{\pi/2}^2} \right) \tag{1.22}$$

is the Coulomb logarithm integrated over the interval from b_c to λ_D. Hence, the ion drag force magnitude F_i can be written as

$$F_i = F_{ic} + F_{io} \tag{1.23}$$

So the ion drag force on the confined dust particle in the local E–field (E) can be written as

$$\vec{F_I} = F_i \hat{E} \tag{1.24}$$

Kharpak *et al.* [87] have reported the role of collisionality on the magnitude of ion drag force. They pointed out that effects of the ion–neutral collisions on the ion drag start when the ratio $l_i/\lambda_D \geq 10$. This condition is also satisfied in our experimental operating regime. In another study of Kharpak *et al.* [93], they have incorporated the screening effect (scattering of ions outside the Debye sphere) in deriving the orbital force. However, the contribution of orbital force is very small compared to the collection force. Hence, in this thesis, Barnes formula [92] is used to evaluate the ion drag force.

1.4.4 Neutral drag force

The neutral drag force is the resistance experienced by a dust particle when there is a relative velocity v_r between the dust particles and the neutral gas, i.e. $v_r = v_d - v_n$. In absence of directed gas flow, relative velocity will be v_d. For the dust particles of size smaller than the collision mean free path, i.e., $r_d << \lambda_{mpf}$ and velocities much smaller than thermal velocity of the gas, i.e., $v_d << v_{Tn}$ then the neutral drag force experienced by the dust particle is estimated using the Epstein's expression [94]

$$\vec{F_n} = -m_d \nu_{dn} \vec{v_d}, \tag{1.25}$$

where ν_{dn} is the dust–neutral friction frequency and v_d is dust particle velocity. The expression for ν_{dn} [43] is

$$\nu_{dn} = \frac{8}{3}\sqrt{2\pi} r_d^2 \frac{m_n}{m_d} n_n v_{Tn} \left(1 + \frac{\pi}{8}\right) \tag{1.26}$$

where m_n, n_n, and v_{Tn} the mass, number density, and the thermal velocity of the neutral gas atoms.

1.4.5 Thermophoretic force

The thermophoretic force appears due to a temperature gradient in the neutral gas. The neutral gas atoms present in the high temperature region will exert more momentum on the dust particles than those present in the lower temperature region. Consequently, a force towards the lower temperature region is established. The magnitude of this force is directly proportional to the gas temperature gradient.

The thermophoretic force is [43]

$$\vec{F_{th}} = -\frac{32}{15}\frac{r_d^2}{v_{th,n}}\left(1 + \frac{5\pi}{32}(1-\alpha)\right)\kappa_T \nabla T_n, \tag{1.27}$$

where κ_T is translation thermal conductivity of the gas and T_n is the neutral temperature. The accommodation coefficient $\alpha \approx 1$ for dust particles and neutral gas atoms having temperature below 500 K.

The schematic representation of the forces acting on a dust grain in the plasma is presented in Fig. 1.4.

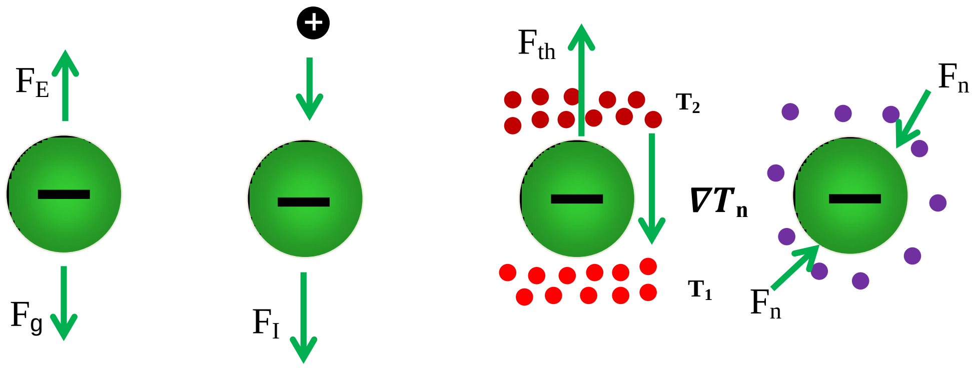

Figure 1.4: Schematic diagram illustrating the forces acting on the dust particles during the confinement in an electrostatic potential well. An Arrow indicates the direction of force acting on dust grain. T_1 and T_2 denote the temperatures of neutrals with $T_1 > T_2$.

1.5 Dusty plasma formation using different electrostatic traps

For the majority of laboratory studies, dusty plasmas are generated in either radio frequency (RF) or direct current (DC) discharge plasmas. In both types of discharges, the dust particles are suspended in regions of high electric field where the electric force balances the gravitational force, i.e., $M_d g = Q_d E$. The strong E-field region can be created using the different discharge configurations, which are displayed in Fig. 1.5. In anode spot trap, dust grains are confined in the anodic plasma where E- field is strong compared to the surrounding plasma [1, 18]. In

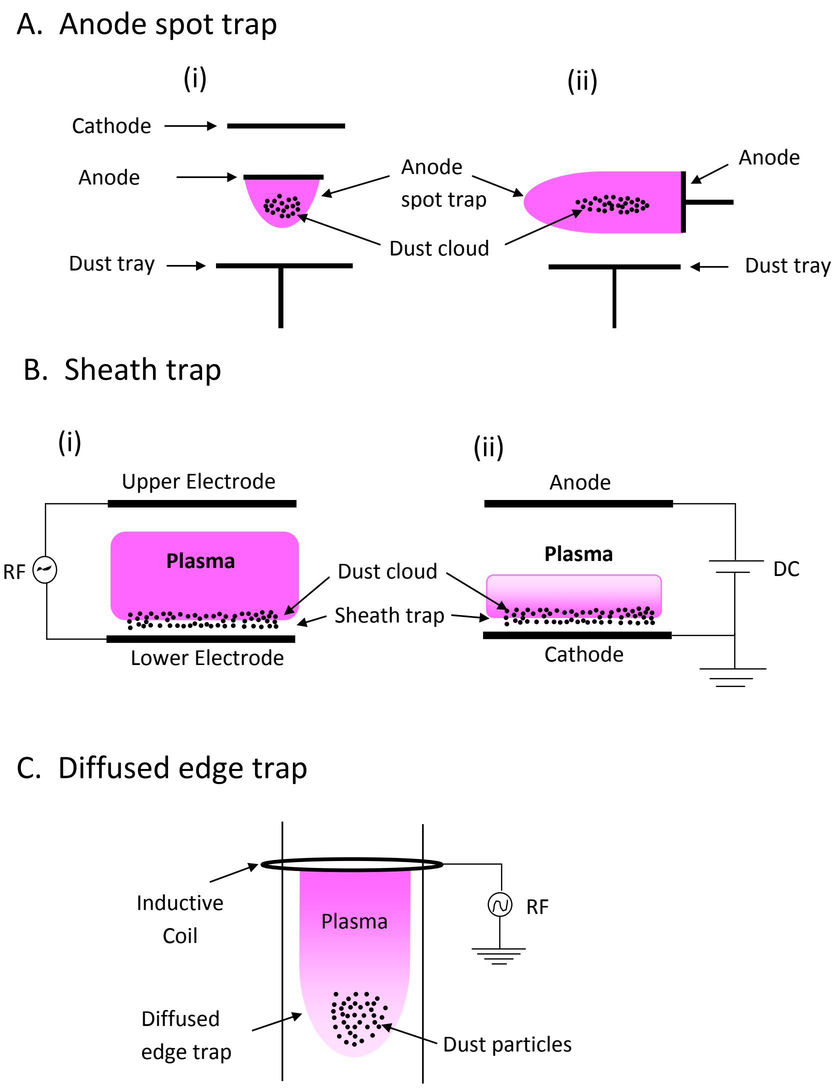

Figure 1.5: Schematic representation of the methods used for producing dusty plasma in the laboratory experiments.

sheath trap, charged grains are levitated near the sheath boundary of the lower electrode in RF discharge [19] and of the cathode in the DC discharge plasma [95]. The strong E-field in the sheath region provides an equilibrium to the massive dust grains. These configurations are widely used to study the physics of dusty plasma. In diffused edge trap, ambipolar E-field of the diffused plasma helps to hold the dust grains against the gravity [20].

1.6 Overview of the earlier work

Dust particles immersed in a low-temperature plasma get negatively charged and constitute a new component of the plasma. The presence of particles in ordinary plasma makes it more complex in two ways: first, these particles alter the properties of some well-known wave modes of the plasma, such as ion–acoustic (IA), or the electrostatic ion cyclotron (EIC) etc. and second, collection of the charged particles supports the various new collective modes, in which dust grain dynamics plays an essential role. Since, the response of dust grains to a self-consistent electric field and/or an external field is very slow because of the large inertia; therefore, its dynamics lies in a very low-frequency regime. Among the various low-frequency wave modes, dust acoustic wave (DAW) is the most studied and popular wave mode in the dusty plasma. The DAW was first predicted theoretically by Rao *et al.* [96] in 1990. Since then it has been studied theoretically by several other groups [44, 97–102] in the weakly/strongly coupled dusty plasma. Apart from the DAW, the dust transverse shear wave (DTSW) [103] and the dust lattice wave (DLW) [104,105], which arise when charged dust particles were considered strongly coupled in the unmagnetized dusty plasma. The DAW has the similarity with the ion–acoustic wave in the ordinary plasma but here the inertia is provided by the charged grains and the restoring force is mainly the electric force arising from charge separation of all three charged species, dust, electrons, and ions, during the compression and rarefaction.

Experimentally, Barken *et al.* [1] in 1994 first investigated the low-frequency dust acoustic mode (DAW) in a Q-machine. These waves were excited in the kaolin dust grains of an average diameter 5 μm, which were confined in an anodic double layer formed in front of a positively biased disk. The experimentally measured wave parameters; phase velocity (v_{ph}) 9 cm/sec, wavelength(λ) 0.6 cm and frequency (f) 15 Hz were in good agreement with the theoretically predicted values. Since then the studies on the self–excited or driven DAWs have been carried out in both DC [1, 2, 24, 106–111] and RF [4, 20, 112–114] discharges. In addition to the DAW, various collective modes in the strongly coupled dust system were investigated in the various ground based [5, 115] and microgravity [116] experiments.

In most of the DC and RF discharges, the low-frequency modes (DAWs) are spontaneously excited due to the ion streaming instability, which occurs when the ion–drift velocity with respect to dust grains exceeds the phase velocity of the wave [117]. Such instabilities develop in the dust plasma system at a low pressure so that the ions drift velocity exceeds or in the order of its thermal speed [22, 118, 119]. At higher pressure, the dust–neutral friction dominates over the energy supplied from the streaming ions; therefore, DAW is no longer excited in the dust medium. Apart from the streaming ions, instabilities associated with charge fluctuations [120] and ionization [121] are considered the possible energy source to excite the DAWs at higher dissipation losses. Fortov *et al.* [122] computed the different growth rates for DAW theoretically by taking into account all the possible reasons for excitation of the DAW.

However, to study the physics behind the instabilities and collective modes, dust cloud dimension must be larger than the characteristic length/size of the collective modes and the confinement time must be longer than the inverse of the dust plasma frequency (ω_d). To study the dusty plasma medium, various configurations in both DC and RF discharges [2, 3, 5, 18–20] to confine an appropriate volume of dust grains for a longer time have been used.

In recent years, the study of stable and unstable dusty plasma with an external electric perturbation, which is applied using a floating or biased object (probe), has been greatly interested. It is realized that a dust-free region (void) is formed around a floating or biased cylindrical object (probe) during the interaction with the grain medium, which was observed in the experiments of Thompson *et al.* [123], Thomas *et al.* [14], Sarkar *et al.* [124], and Klindworth *et al.* [125]. In the experiments of Kim *et al.* [16], they investigated the diffraction of dust acoustic waves during the interaction with a floating cylinder. The interaction of a positively (or negatively) biased cylindrical probe on the crystalline state of the grain medium was reported by Law *et al.* [15]. They observed the circulation of dust grains in the perturbed region of probe. Interaction of the flowing dusty plasma with an electrically biased wire was studied by Meyer *et al.* [126] and found the excitation of a bow like shock structures. The interaction of flowing dusty plasma with a stationary floating wire can excites the nonlinear structures (precursor solitons) behind it [127].

Another example of the collective response of the dust-plasma system is the formation of dynamic structures (or vortices). The rotation of dust component has been an interesting fundamental issue in astrophysics and laboratory plasmas. The rotation of dust component has been observed in various laboratory plasma in the presence and absence of the magnetic field. In the presence of magnetic field (**B**), dust particles are found to rotate only on the imposition of an external magnetic field exceeding a certain critical magnitude. Maemura *et al.* [128] proposed a model to explain the dust grains drift in the presence of a magnetic field (**B**) perpendicular to the discharge electric field (**E**). In the magnetic field, electrons are transported in the $\mathbf{E} \times \mathbf{B}$ direction at a faster speed while the ions are transported with a slower speed in the same direction. The negatively charged particles are drifted in the direction to the $\mathbf{E} \times \mathbf{B}$ with a slower speed to ions. Konopka *et al.* [129] observed the dust cloud suspended in the sheath of an RF discharge rotate in the two fashions: a rigid body rotation and sheared rotation. The azimuthal ion drag due to the $\mathbf{E} \times \mathbf{B}$ drift was considered the possible cause for cluster rotation. The experiments of Sato *et al.* [130] in DC and RF discharge plasmas also demonstrated the rotation of particles in the azimuthal direction under the influence of a vertically magnetic field. Kaw *et al.* [131] have proposed a model to explain the azimuthal rotation of dust particles in the presence of magnetic field. Instead of these studies, various experimental groups have studied the motion of the dust component in the weak magnetic field [12, 132–134]. Since, dust grains are massive therefore strong magnetic field ($\mathbf{B} > 3$ T) is required to magnetized them. A magnetized dusty plasma device (MDPX) is being designed to perform the next experiments on the magnetized dusty plasma [135, 136].

Rotation of dust component and convective vortex motion in the absence of magnetic field in ground-based laboratory plasma as well as under microgravity conditions have been reported by various groups. Law *et al.* [15] observed the dust mass circulation in the crystalline state of grain medium when it is perturbed by a biased probe. The origin of the circulation is attributed to the formation a nonuniform electric field in the crystal region by a biased probe. The extensive studies on the dust rotation and/or vortex motion such as spontaneous dust grains rotation [17], 2D dust vortex flow [137], dust cluster rotation [138], poloidal rotation of dust grains with toroidal symmetry [13], horizontal and vertical vortex motion in the presence of an auxiliary electrode [139], vortex motion in the ice dusty plasma [11] and vortex motion along with wave [9] have been carried out in various ground-based experiments. Under the microgravity conditions, dust vortices were observed around the dust free region [140]. In the absence of magnetic field, the simulation works [8, 141, 142] show that vortex structures are generated due to the non-conservative nature of the forces (ion drag force, electric force, and screened Coulomb force) acting on the dust grains. Also, the dust vortices are induced by the convection of the neutral gas, which can be induced by the temperature gradient at atmospheric pressure and by the thermal creep along the surface at low-pressure [143–145]. Instead of these mechanisms, the spatial variation of the dust charge is also a possible mechanism to convert the potential energy of an external electric field into kinetic energy of the dust grains [27]. Usually, the dust grains achieve electrostatic equilibrium with respect to the plasma by acquiring a negative charge. The charge on the dust particles is not fixed but is coupled self-consistently to the surrounding plasma. It causes instabilities and leads to the excitation of dust collective modes. Vaulina *et al.* [27, 146] have carried theoretical and numerical analysis of the dust–plasma system by considering the gradient of dust charge orthogonal to the non-electrostatic force [9, 27]. They have predicted that charge gradient is a major source to excite the vortex motion. The charge gradient of dust grain arises mainly due to the inhomogeneity in the background plasma parameters.

1.7 Motivation behind the present research work

In the plasma, the presence of dust particles can modify the background plasma parameters (e.g. charge and potential distribution) [147, 148] and usual plasma waves and associated instabilities [88, 149, 150]. Furthermore, the presence of massive charged particles gives rise to new low-frequency collective modes (e.g., waves and vortices), which is a result of the collective motion of the dust grain medium. As is well known that dusty plasma is a dissipative medium thereby to exhibit the collective motion, the dissipation losses must be compensated by available energy in the dust grain system. In dusty plasma, dissipation losses are mainly due to dust–neutral friction, which can be externally controlled by changing the background gas pressure. The instabilities associated to streaming of plasma species (electrons and ions) and inhomogeneous distribution of background plasma parameters (n and T_e) are observed to be responsible available free energy source in the dust plasma system [20, 22, 117, 146]. The dusty plasma system supports various collective modes when the available energy (free energy) overcomes the energy dissipations [1, 9, 20, 146, 151]. It essentially means that small amount of free energy can trigger the low frequency collective modes when the background pressure is low. Furthermore, it is to be noted that collective motion of dust grains is self–consistently linked to ambient plasma parameters thereby the characteristics of the dusty plasma medium strongly depend on the background plasma. The distribution of background plasma species can be modified either by changing the discharge parameters or by external electric perturbation. In both cases, collective dynamics of dust grain medium get affected. To study the collective modes in dusty plasma; dimension of dust grain medium must be larger than the characteristic size of collective modes (wavelength for waves and diameter for vortex) and confinement time must be longer than characteristic time of dust oscillation ($\tau_d = \omega_{pd}^{-1}$). The studies of self–excited or driven collective modes have been carried in various particle confinement configurations (anode trap, cathode trap and diffused edge trap) [3, 20, 151–153]. The previous studies on self–excited collective modes were performed in a small volume dusty plasma at comparatively higher pressure. The collective motion of dust grains in a large volume (or in an extended 2D dust cloud) dusty plasma at low pressure is still an unexplored problem. Making a dusty device to create large volume dusty plasma at low pressure and to study of the self–excited collective modes were the major tasks of the present research work. The characteristics of the dusty plasma medium with an external electric perturbation was also the aim of the doctoral thesis.

1.8 Scope and outline of the thesis

This thesis addresses experimental investigations of the self-excited collective modes and its characteristics in the low pressure (≤ 0.07 mbar) large volume dusty plasma. At first, a conventional DC discharge (cathode-anode) configuration is used to create 3D dusty plasma at comparatively low gas pressure. The excitation of dust acoustic waves and its propagation characteristic with an external electric perturbation, which is applied using a floating cylindrical object, have been studied. Working at even low-pressure (< 0.05 mbar) using DC discharge configuration makes dust grain medium highly unstable, which creates trouble in the study of collective phenomena. For producing an equilibrium dusty plasma at lower pressure (0.05 to 0.01 mbar), a novel configuration using inductively coupled plasma (ICP) is investigated. It is an electrodeless configuration to confine the dust grains. For injecting dust grains into an electrostatic trap, a unique technique using the DC discharge plasma has been explored. The collective dynamics of dust grains confined in an electrostatic trap formed using ICP configuration have been studied at the wide range of discharge parameters. The underlying physics causes the modification in the propagation characteristics of the dust acoustic waves with an external potential perturbation, particles transport and trapping in a potential well of the inductively coupled diffused plasma, and collective dynamics of the large volume dusty plasma have been thoroughly investigated. This thesis consists of six chapters and is organized as follows:

Chapter-2: *Experimental Setup and Diagnostics.* In this chapter, the experimental setup developed for the study of collective phenomena (e.g., waves and vortices) in dusty plasma is presented. A detailed description of vacuum chambers, power supplies, pumping system, cathode and anode design are provided. Experimental configuration to produce the plasma and dusty plasma in both DC and RF (inductively coupled) discharges are discussed. Design and operation principle of the various electrostatic probes to diagnose the plasma are discussed in detail. At the end of this chapter, imaging techniques and image analysis using various software are discussed.

Chapter-3: *Dust Acoustic Wave and its Propagation Characteristic in Presence of a Floating Object.* This chapter contains the experimental results of dust acoustic waves and its propagation modification by a floating cylindrical object. The chapter begins with the introduction about the dust acoustic wave and its characteristics. The characterization of plasma and dusty plasma at various discharge parameters are presented. Excitation of dust acoustic waves, its dispersion relation and its characteristics are presented. The interaction of the floating cylindrical rod, which is aligned either vertically or horizontally, with the propagating dust acoustic waves is discussed in detail. The qualitative explanations to understand the oblique nature of the dust acoustic waves in the perturbed region is discussed in details. The work is summarized at the end of this chapter.

Chapter-4: *Transport and Trapping of Dust Particles in Diffused Plasma.* In this chapter, transport and trapping of dust particles in a potential well created by inductively coupled diffused plasma are discussed in detail. At the beginning of chapter, various configurations either in DC or RF discharge used to confine the dust grains are highlighted. The description of the experimental configuration along with the coordinate representation is provided. The characterization of diffused plasma using electrostatic probes to understand the transport and trapping of particles are presented in this chapter. Calculations of forces acting on the particles to describe the transport and confinement of dust grains in a potential well are given. The dynamical behavior of dusty plasma at different discharge conditions is discussed. Brief summary of the work is given at the end of this chapter.

Chapter-5: *Multiple Co–rotating Vortex Structures.* In this chapter, the results on the origin of the multiple co–rotating vortices are presented. Introduction about the particle rotation in the absence and presence of a magnetic field is highlighted. Experimental configuration to study the self–oscillatory motion of dust particles at various discharge conditions is presented. The formation of multiple co–rotating vortices, transition from multiple to single vortex, and particle velocity distribution in a vortex structure are discussed in detail. The quantitative analysis to describe the origin of vortex flow and its multiplicity are discussed with the theoretical model. Summary of presenting work is given at the end of this chapter.

Chapter-6: *Conclusion and Future Scope.* In this final chapter, an overall summary of the experimental studies on collective phenomena in dusty plasma is provided. Also, the future scopes and possible extension of the presented work is discussed.

2

Experimental Setup and Diagnostics

In this chapter, we provide a description of the experimental setup used for the study of dusty plasma. The various types of power supply used for plasma production and characterization are presented. This chapter also presents various discharge methods to produce dusty plasma and various diagnostics tool to characterize the plasma as well as dusty plasma.

2.1 Introduction

The thesis work is devoted to the study of collective phenomena in a large volume low-pressure dusty plasmas. For getting an appropriate dusty plasma, the experiments are carried out in both DC and RF discharge plasmas. This chapter provides the detailed description of experimental setup, different power supplies used for production and characterization of plasmas, plasma production mechanism using the DC and RF power sources and different kinds of instruments and diagnostics used in the present study of the dusty plasma phenomena such as dust-acoustic waves and its propagation characteristics, dust particles transport and trapping in a potential well and the collective modes (waves and vortices) in a large volume dusty plasma. At first, a DC discharge configuration is used to create an appropriate 3D dusty plasma at a comparatively low pressure and experiments are performed to study the propagation characteristic of the dust acoustic modes in presence of an external electrostatic perturbation. Later, to avoid the limitations of the DC discharge configuration and to create a large volume dust grain medium at low pressure, an inductively coupled (RF) discharge configuration is employed. The studies on collective modes (waves and vortices) are performed in the dusty plasma medium created by an inductively coupled discharge. The technical specifications for the particular experimental configuration is discussed in an appropriate chapter.

This chapter is organized as: Sec. 2.2 describes the experimental assembly (vacuum chambers), gas pumping system, electrode geometry and the power supplies used for plasma generation and characterization. The plasma and dusty plasma production using the DC and RF power sources are discussed in Sec. 2.3. Sec. 2.4 deals with an operation and the measurement techniques to characterize the plasmas using the various electrostatic probes (single Langmuir probe, double probe and emissive probe). The optical imaging of the levitated dust cloud, storage of images, and image analysis techniques are discussed in Sec 2.5. It includes the specifications of different optical accessories (Laser, cylindrical lens and CCD/CMOS cameras) and image analysis computer software (ImageJ and MATLAB based PIV software).

2.2 Experimental setup

In this section, the experimental setup used for the study of collective phenomena in a dusty plasma medium is discussed. The setup mainly consists of a main experimental chamber, buffer chamber, pumping system, power supply etc. and these are described in the following subsections.

2.2.1 Vacuum vessels and pumping system

The entire experiments of this thesis work are carried out in a cylindrical borosilicate glass chamber of diameter 15 cm and length 60 cm. This chamber has seven radial and two axial ports, which are used for different purposes. The radial ports P1 and P3 have the length of 13 cm and an inner diameter of 7.5 cm, P2, P4 and P5 have the length of 8 cm and an inner diameter of 5 cm, P6 has the length of 8 cm and an inner diameter of 7.5 cm, and P7 has the length of 8 cm and an inner diameter of 10 cm. A buffer chamber made of stainless steel (SS) of 15 cm in diameter and 20 cm in length is attached to the experimental chamber through a stainless steel tube. The length and the inner diameter of the SS tube are 2.5 cm and

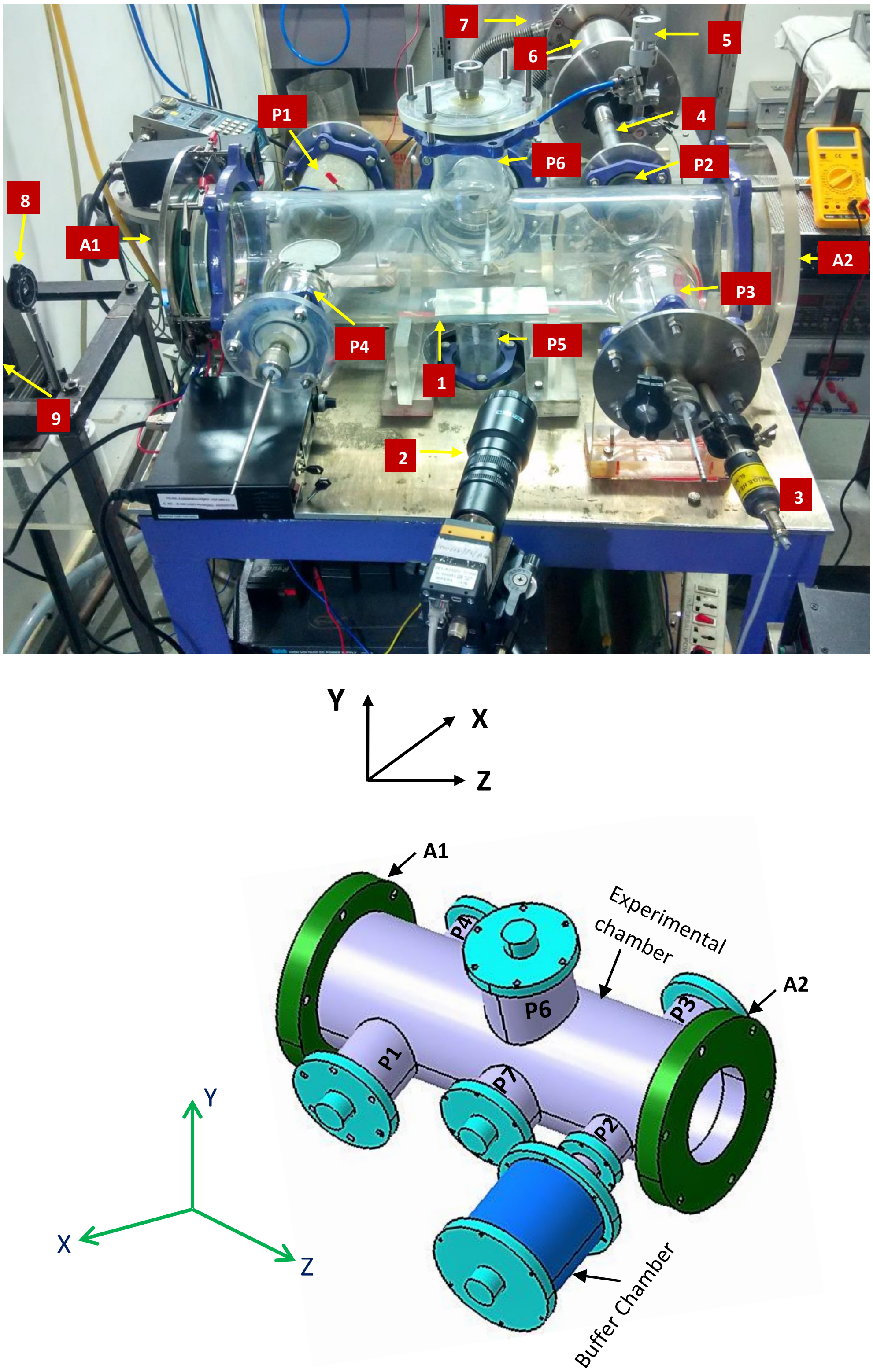

Figure 2.1: (a) Experimental Setup: A1 and A2 indicate the axial ports of the experimental tube. P1 to P7 represent the radial ports of the experimental chamber. (1) Glass chamber, (2) CCD camera, (3) Pirani guage, (4) SS tube for connecting both chambers, (5) gas inlet through needle valve, (6) buffer chamber, (7) gas outlet through rotary pump, (8) Cylindrical lens, and (9) Laser. (b) 3D view of the experimental setup.

15 cm, respectively and attached to the radial port (P2) as shown in Fig. 2.1(a). The pumping system and gas injection valve are attached to the buffer chamber. To evacuate the experimental chamber up to $\sim 10^{-3}$ mbar, a rotary pump with pumping speed of 350 Liter/min is used. One of the radial ports (P3) is used to measure the pressure inside the experimental chamber with the help of a digital Pirani gauge (model-DHPG-020). The chamber is filled with argon gas (99.99 % pure) by a precision gas dosing valve (Pfeiffer make) at a working pressure (p) of 0.01–0.1 mbar. Other radial ports are used to diagnose the plasma (or dusty plasma) using the electrostatics probes (imaging diagnostics). The axial ports (A1 and A2) are used to illuminate the dust particles by Laser light and to capture the scattered light coming from the dust grains. The 3D view of experimental setup is presented in Fig. 2.1(b).

2.2.2 Cathode and anode

A DC glow discharge is initiated by applying the dc voltage between a cathode and anodes. A stainless steel (SS) disk-shaped electrode of 10 cm diameter having a plane surface on one side and a step of 5 mm width and 2 mm height around its periphery on the other side (see Fig. 2.2) is used as a cathode. The radial port (P7) is utilized to hold the cathode through a cylindrical rod (5 mm in diameter) in the glass chamber. A both sided planar SS disk of 4 cm diameter (see Fig. 2.2) is used as anode (lower anode). The bottom radial port (P5) is utilized to hold this anode below the cathode. Another anode (upper anode) is a SS flange of 7.5 cm diameter. This anode is kept parallel to particles containing cathode surface and is placed 15 cm above the cathode.

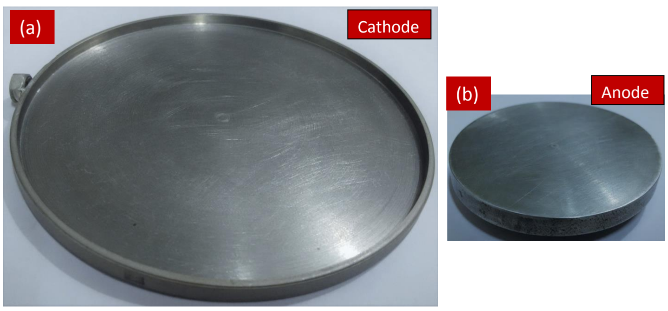

Figure 2.2: Photographs of the cathode and anode used to produce the DC glow discharge plasma.

2.2.3 Power supplies

Power supply is an electronics device, which is used to supply the electric energy to a load. In our experiments, various types of power supply are utilized for production of plasma as well as its characterization. In this section, we provide detailed description of the various power supplies.

2.2.3.1 High voltage regulated DC power supply

To breakdown the gas between the cathode and anode, a high voltage DC power supply (Aplab make H1010S) is used. The output voltage and current rating of supply are 100–1000 V and 1 A, respectively. In the measurement of plasma potential V_p, an emissive probe is used. For heating the filament of emissive probe, a DC regulated power supply (Aplab make L3230) of voltage rating 0 to 32 V and current rating 0 to 30 A is used.

2.2.3.2 Langmuir probe power supply

This supply gives a sweep output voltage (-50 V to + 50 V) at 50 Hz frequency with a DC shift of -1.2 V to -40 V that is used to bias the Langmuir probe to get the I–V characteristic. The working principle of the electric circuit of this supply is described by the schematic diagram (see Fig. 2.3) along with the probe, which is given as:

1. **Voltage source to bias Langmuir probe** This circuit consists of a ramp generator that generates a ramp voltage of +50 V to -50 V with a frequency of 50 Hz. This ramp voltage is given to probe along with a dc shift of -1.2 V to -40 V. When the probe is exposed to the plasma it acquires a potential known as the floating potential. Langmuir probe draws electron or ion current according to the positive or negative potential applied with respect to the floating potential. The dc shift is adjusted accordingly to obtain the required electron or ion current.

2. **Sensing resistor** The biasing voltage to the Langmuir probe is applied through a variable sensible resistor. The resistance can be varied from 1 kΩ to 10 kΩ depending on plasma parameters. The potential drop developed across the resistor is measured using a differential amplifier.

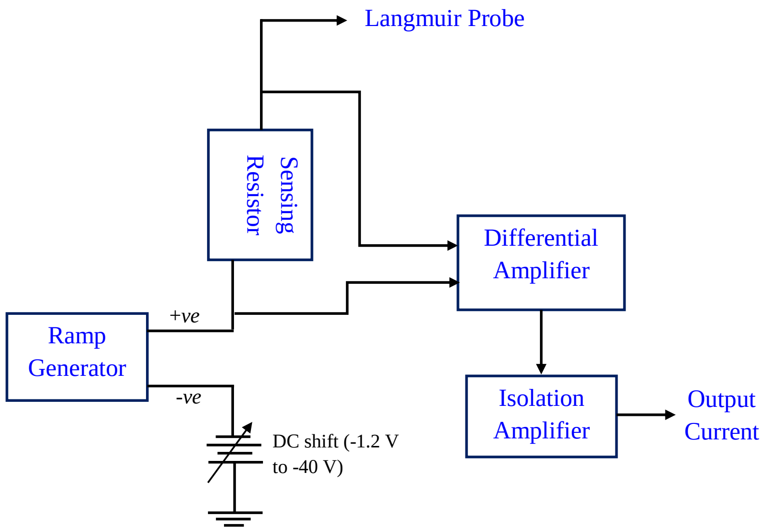

Figure 2.3: Schematic diagram of power supply used for characterizing the plasma using a Langmuir probe (i.e., Langmuir probe power supply).

3. **Differential amplifier** The voltage drop across the sensing resistor is fed to the input of the differential amplifier circuit. The circuit is developed by using IC OPA27. It is an ultra low noise and very high precision amplifier. The differential amplifier circuit measures the potential difference across the sensing resistor and gives an output, proportional to the current drawn by the probe corresponding to the applied voltage.

4. **Isolation amplifier** In our case, the entire circuit described above is kept floating at a high voltage (+50 V to -50 V ramp with a -1.2 V to -40 V dc shift). To measure such current in an oscilloscope with respect to normal ground, the isolation amplifier is used (using IC ISO106B). It isolates two grounds and gives the same voltage drop across the probe resistance with respect to normal ground at the output side. The current obtained at the output of the isolation amplifier and the applied voltage are measured with the help of an oscilloscope (Tektronix TDS 2024, 200 MHz and 2 GS/s). The applied voltage to the probe is attenuated through a 10X probe. These data are stored on a data storage device. The stored data are used to construct the I–V characteristic to determine the plasma parameters such as density (n), floating potential (V_f) and electron temperature (T_e).

2.2.3.3 RF power supply

In the case of RF discharge (inductively coupled discharge), to initiate the gas breakdown in one of the radial ports (P1) of the experimental tube, an RF source of 13.56 MHz and 100 W is used.

2.3 Plasma and dusty plasma production

The basic requirement to study the collective motion of the dust grain medium is a suitable plasma source that can produce equilibrium plasma at low gas pressure (0.01–0.1 mbar) and provides the strong electric field to confine the negatively charged particles. The plasma properties such as density, electron temperature, plasma potential etc. depend significantly on different techniques adopted in producing the plasma. In the first set of experiments, the DC plasma source is used to produce the large volume (3D) dusty plasma. In the DC discharge (cathode trap), poor confinement and cathode spots (sparking) are problematic to study the dynamics of dusty plasma at low pressure. In view of these limitations, an RF plasma source is used to create dusty plasma at low pressure. In both DC and RF discharges, the properties of the plasma as well as dusty plasma is found to be different. In this section, we will discuss the DC and RF discharge configurations to produce plasma and dusty plasma in the laboratory.

2.3.1 DC glow discharge plasma

Laboratory plasma is formed when gas is ionized by passing an electric current through it. For passing the current, either constant current sources or constant voltage sources can be used. For carrying out the experiments in the present thesis, a constant DC voltage source is used. When an electric field is applied to the parallel plates (cathode and anode) of inter spacing d containing argon gas, at sufficiently high fields the gas suddenly breakdown and transforms to conducting gas. The schematic diagram for producing the DC glow discharge plasma is depicted in Fig. 2.4. It is supposed that few electrons are always available in the gap of the electrodes either by the action of cosmic ray or as a consequence of field emission from asperities on the surface where electric field is strong. The free electrons gain energy in the E–field and start to drift in the gap. These drifted electrons collide

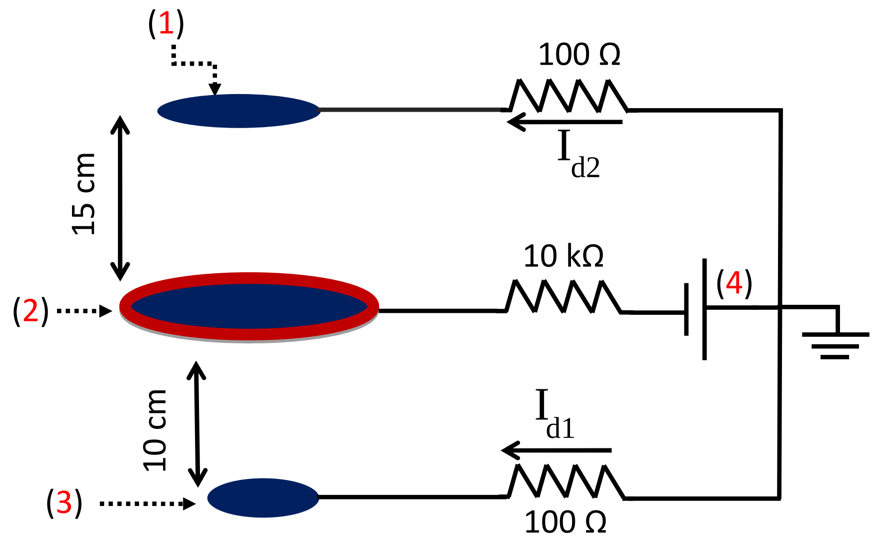

Figure 2.4: Schematic diagram for producing the DC glow discharge plasma: (1) Upper anode, (2) cathode, (3) lower anode, and (4) high voltage DC power supply.

with the background gas neutral atoms and transfer the momentum to gas through an elastic and non–elastic collision processes. In the non–elastic process such as ionization, electron–ion pair is formed. In this E–field, the electrons drift toward the anode and the ions drift toward the cathode. The bombardment of ions to cathode releases energy because of the recombination of ions and electrons, which helps to remove the electrons from the cathode. The emission of electrons from the cathode is called the secondary electron emission. The electrons emitted in this process start to drift in the E–field and produces the electron-ion pair. The newly produced electrons also gain energy in the E–field and take part into the ionization processes. Such process is called as multiplication. Hence, both secondary electron emission and multiplication processes are being continued to sustain the gas discharge [56, 154–156].

The Paschen's law [157] tells about the breakdown of gases in presence of electric field. According to this law, breakdown of gases depend on the gas pressure (p) and the distance between electrodes (d). For planar geometry, Paschen's law is expressed as

$$V_B = \frac{A(pd)}{ln(pd) + B}, \tag{2.1}$$

where V_B is breakdown voltage for gas in volt. A and B are constants which depend on gas composition. If we plot Eq.(2.1), V_B verses pd, then the obtained curve is called Paschen curve. In our experiments, gas breakdown is initiated in

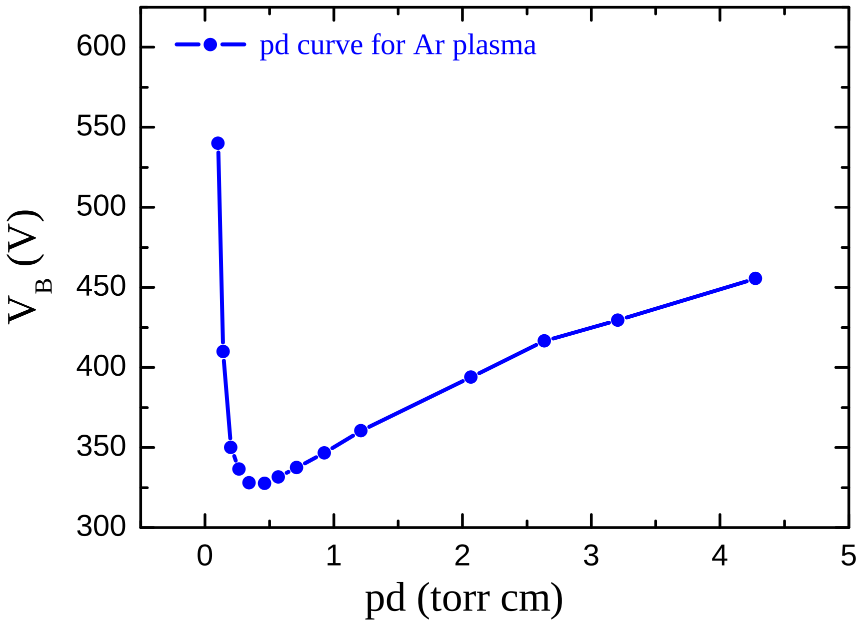

Figure 2.5: Paschen breakdown (pd) curve for argon gas.

the gap of cathode and anodes at different argon gas pressures. The Paschen curve is constructed for the gas breakdown between cathode and lower anode, which is shown in Fig. 2.5. This curve classifies the operating regions of p and V_B for the experiments presented in this thesis. The obtained value of minimum breakdown voltage for argon gas is $\sim$ 320 V at pd value of $\sim$ 0.5 Torr-cm. The breakdown voltage (V_B) increases on the either side of the minimum value of pd.

After breaking down the gas, charge species (electrons and ions) are drifted towards the opposite polarity electrode, resulting in current flow through conducting gas. The plasma (discharge) current (I_d) variation with the applied voltage (V_d) between cathode and anodes, which is called I–V characteristics, is used to understand the basic properties of the ionized gas. The current flowing through the ionized gas is calculated by the measured value of voltage drop across 100 Ω resistance. The variation of I_d in both the discharge paths with applied voltage at argon pressure, p = 0.07 mbar are depicted in Fig. 2.6. It is clearly seen in Fig. 2.6 that at first, I_{d1} (represented by closed rectangles) starts flowing at 320 V whereas I_{d2} (represented by closed circle) is initiated at 340 V. It indicates that plasma initially forms in between the cathode and the lower anode at about 320 V and later it strikes between the cathode and upper anode. The value of I_{d1} is found to be higher than I_{d2} at any discharge condition. It is also observed that

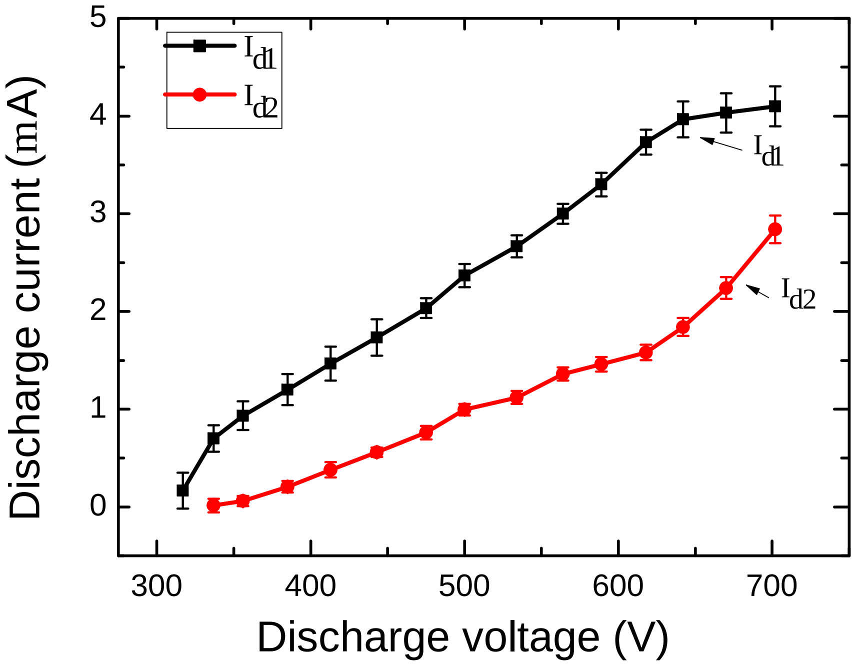

Figure 2.6: Current–voltage ($I_d - V_d$) characteristics of the DC glow discharge at argon pressure of 0.07 mbar.

current flowing in each path depends on the nature of the gas, dimensions of each electrode and material used for the electrode. It is to be noted that the value of current shows the conducting strength of the ionized gas. In the normal glow region, plasma conductivity or ionization rate increases with the applied voltage, which results in increase the density of the charge carriers (electrons and ions).

As discussed above, the electrons are repelled from the cathode while positive ions are drawn towards it. Around the cathode there is a region, which contains an excess of the positive ions than electrons is called cathode sheath. In fact, the cathode is perfectly screened from the positive ions. The potential is less negative near the cathode and at a certain distance is equal to the potential of the plasma. Due to this potential gradient, there is a strong electric field in the sheath region [158]. The E-field present in the cathode sheath region helps to hold the dust grains against the gravity, consequently, a 3D dusty plasma is formed when poly-dispersive particles are used. The detailed characteristics of the dusty plasma are presented in Chapter 3.

2.3.2 Inductively coupled discharge plasma

An inductively coupled discharge is an example of an RF discharge, which is used to produce the plasma in the laboratory. For initiating the rf breakdown, high frequency (13.56 MHz) electric current (I) is passed through an inductive coil. As high-frequency current passes through the inductive coil, the time varying magnetic field with the coil which is directed along the axis of the source tube (P1 or P5) induces the azimuthal electric field in the argon gas. It is supposed that a few electrons are always present in the background gas due to the cosmic ray. These electrons pick up energy in the circulating electric field. When the energy of the electron exceeds the ionization potential of atomic gas then it ionizes neutral atoms by electron impact ionization processes. In this process, an electron-ion pair is formed. After the end of this process, two slow electrons are produced. These electrons again gain energy in the electric field and resulting in ionize the gas atoms. This process (multiplication) is being continued; therefore, gas becomes non-conducting to conducting [158,159]. This discharge is described as "electrodeless discharge" because there is no requirement of cathode or anode. The solid enamel copper wire of 2.5 mm diameter is used to make an inductive coil of required turns. The input impedance of circuit is 50 Ω, therefore the calculated inductance of an inductive coil to couple maximum power is $\sim 0.6\ \mu$H. In our case, an inductive coil of equally spaced five turns (wrapped around the source section P1) of inductance $\sim 0.8\ \mu$H is used to couple the rf power.

For producing dusty plasma, inductively coupled plasma is allowed to diffuse into the experimental chamber. An electrostatic potential well is formed due to the diffused plasma and particles are found to confine in it. Details on the particles confinement or dusty plasma formation using an inductively coupled diffused plasma is discussed in Chapter 4.

2.4 Plasma diagnostics

The electric probe methods are widely used diagnostics to measure the plasma parameters such as plasma density (n), electron temperature (T_e), floating potential (V_f) and plasma potential (V_p). This section deals with design, operation and techniques to measure the plasma parameters using the single Langmuir probe, double probe, and emissive probe.

2.4.1 Single Langmuir probe

The Langmuir probe is one of the most common and widely used plasma diagnostics to measure the parameters of the bulk plasma. It measures plasma parameters such as floating potential (V_f), plasma potential (V_p), plasma density (n), ion current density (J_i) and electron temperature (T_e). The Langmuir probe is a conducting wire, planar disk, or sphere of small radius. When it is inserted into the low-temperature plasma, it drains the current which depends on the relative potential of the probe with reference to plasma potential. The variation of probe current (I_p) with external potential (bias voltage) on the probe is called as I-V characteristic of the Langmuir probe. In 1923, I. Langmuir developed a theoretical model [160], based on OML theory, to estimate the collected current by a probe at various relative potentials. This theory deals with the following assumptions: First, current collected by the probe (I_p) should be smaller in magnitude than the current flowing between cathode and anode (I_d). Second, the probe act as a perfect absorber of ions and no secondary electrons are emitted from its surface. Third, electrons or ions should not undergo the collision with neutrals inside the space charge region (sheath) of the probe. Before using the single Langmuir probe to characterize the plasma, following necessary conditions have to be taken into consideration:

1. The size of the probe should be made sufficiently small enough to minimize the local perturbation.

2. Th material used to construct the probe should have high melting point and less sputtering rate.

3. In the bulk plasma, the condition $\lambda_{e,i} >> r_p >> \lambda_{De}$ should be satisfied, where $\lambda_{e,i}$ is mean free paths for electrons (ions), λ_{De} is a screening length.

4. The electrons of the bulk plasma should obey the Maxwellian distribution.

Keeping in mind all the necessary criteria of the Langmuir probe theory, we have used a cylindrical probe of length 7 mm and radius 0.25 mm made of tungsten. In some cases, we have used a planar probe made of a SS disk (planar) of radius 4 mm

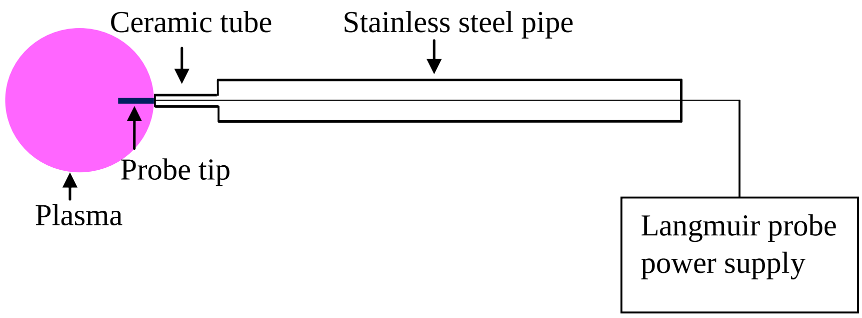

Figure 2.7: Schematic diagram of the single Langmuir probe.

to characterize the plasmas. The probe is connected to a conducting wire which comes out through a BNC connector mounted on an SS 304 shaft of outer diameter 5 mm. The SS shaft is introduced into the vacuum chamber through a vacuum feedthrough so that position of the probe can be set at a desired location inside the chamber. The schematic diagram of a single Langmuir probe (cylindrical) is shown in Fig. 2.7.

The current collected by the Langmuir probe (I_p) is measured at different probe bias voltages (V_b). The variation of I_p with V_b is termed as the I-V characteristic of the probe, which contains information about the bulk plasma. The I-V characteristic of the probe taken at discharge parameters (p = 0.05 mbar and P = 8 W) is presented in Fig. 2.8. The collected current is divided into three regions. These regions A, B and C corresponds to mainly ion current, both electron and ion currents and only electron current, respectively. Probe bias voltage at which it doesn't draw any current is called floating potential (V_f). The V_f and V_p are floating and plasma potential with respect to the grounded reference. The current collection to probe is determined by the difference of plasma potential and probe potential. When the bias voltage V_b on the probe is sufficiently negative with respect to the plasma potential V_p, i.e., $V_b << V_p$, the probe collects mainly positive ions and the corresponding current is called ion saturation current I_{is}. The region A in Fig. 2.8 represents the ion saturation current. In the intermediate potential range $V_f < V_b < V_p$, the probe collects both electron and ion currents. It is called transition region of the I-V characteristic, which is denoted by region B. For $V_b = V_f$, ion I_i and electron I_e currents are equal. When the probe bias V_b reaches to the plasma potential V_p, i.e., $V_b = V_p$, the I–V characteristic exhibits a "knee" because at this point probe repelling ions and attracting electrons. For $V_b >> V_p$,

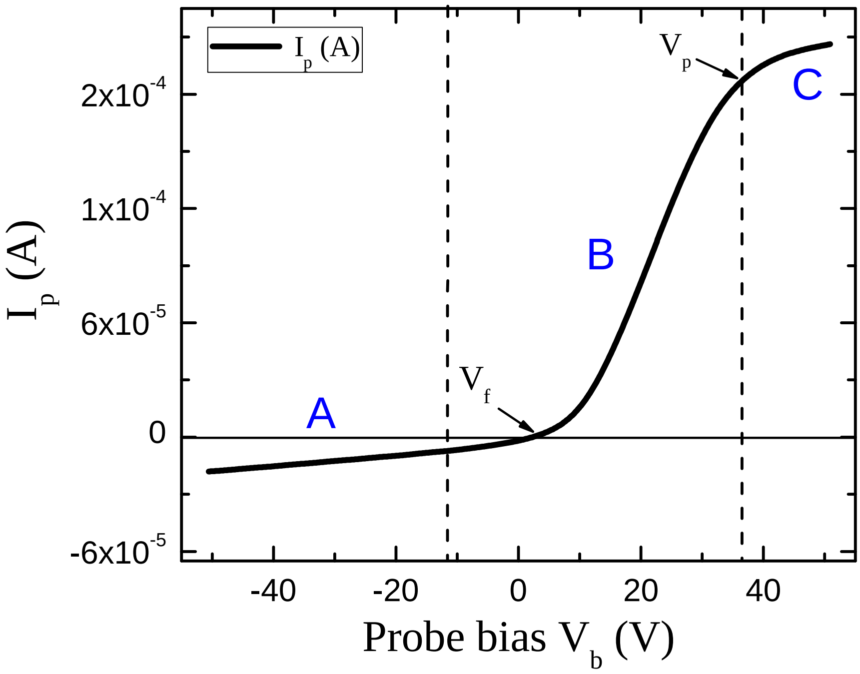

Figure 2.8: I–V characteristic of the single Langmuir probe.

probe mainly collects electrons and corresponding current is called electron saturation current, I_{es}. The region C of the I-V characteristic represents the electron saturation current. For the Maxwellian ion distribution at the temperature T_i, the dependence of the ion current on the probe bias is given by [158, 161–163]

$$I_i(V_b) = \begin{cases} -I_{is}exp[e(V_p - V_b)/k_BT_i], & \text{for } V_b \geq V_p \\ -I_{is}, & \text{for } V_b << V_p, \end{cases} \tag{2.2}$$

where e is the electron charge and k_B is the Boltzmann constant. When $T_e >> T_i$, ion saturation current is given by

$$I_{is} = 0.6 n_i e A_p C_s, \tag{2.3}$$

where n_i is the ion density at the sheath edge, A_p is collecting area of the probe and C_s is ion acoustic speed or Bohm speed. Bohm speed [158, 164] is the speed at which ions enter the sheath region and expression is given as:

$$C_s = \sqrt{\frac{k_B T_e}{m_i}}, \tag{2.4}$$

where m_i is the ion mass. It indicates that the ion saturation current is determined by the electron temperature. As the probe is biased towards the plasma potential, the electron current increases whereas the ion current decreases because of the reduction in the strength of the repulsive electric field. In this regime ($V_b < V_p$), for a Maxwellian electron velocity distribution, the electron current increases exponentially with increasing V_b. When the probe bias voltage is more positive than the plasma potential ($V_b > V_p$), it collects electron saturation current I_{es}. The electron current as a function of the probe bias is expressed as [161–163,165]

$$I_e(V_b) = \begin{cases} I_{es}exp[-e(V_p - V_b)/k_B T_e], & \text{for } V_b \leq V_p \\ I_{es}, & \text{for } V_b > V_p, \end{cases} \tag{2.5}$$

where $I_{es} = \frac{1}{4} n_e e A_p v_{e,th}$ is electron saturation current. Taking the logarithm of electron current in the retarded region (expression 2.5 for $V_b \leq V_p$), we get

$$ln(I_e) = \frac{eV_b}{k_B T_e} + \left(ln(I_{es}) - \frac{eV_p}{k_B T_e} \right) \tag{2.6}$$

This is an equation of the straight line. Inverse of the slope of the linear region of the plot between logarithm of the electron current (lnI_e) and the potential on the probe (V_b) will give the electron temperature and is given by

$$T_e = \frac{dV_b}{d(lnI_e)} \tag{2.7}$$

After obtaining the electron temperature and ion saturation current from I-V characteristics and putting the values in Equation (2.3), plasma density ($n = n_i \simeq n_e$) in bulk plasma can be calculated.

In our laboratory plasma, ion saturation current, I_{is}, doesn't remain constant but it grows linearly with the probe potential V_b. In such cases, erroneous measurements of I_{is} and $ln(I_e)$ are expected. Therefore, ion current (I_i) is extrapolated back to floating potential (V_f) (Fig. 2.9) to get a better measure of I_{is} before the

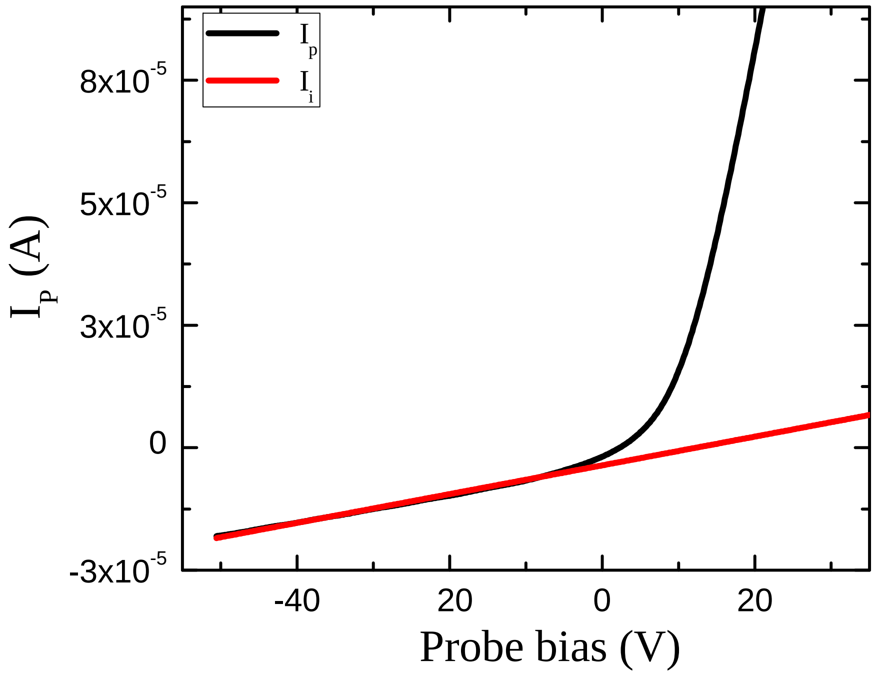

Figure 2.9: Plot shows an extrapolated ion current.

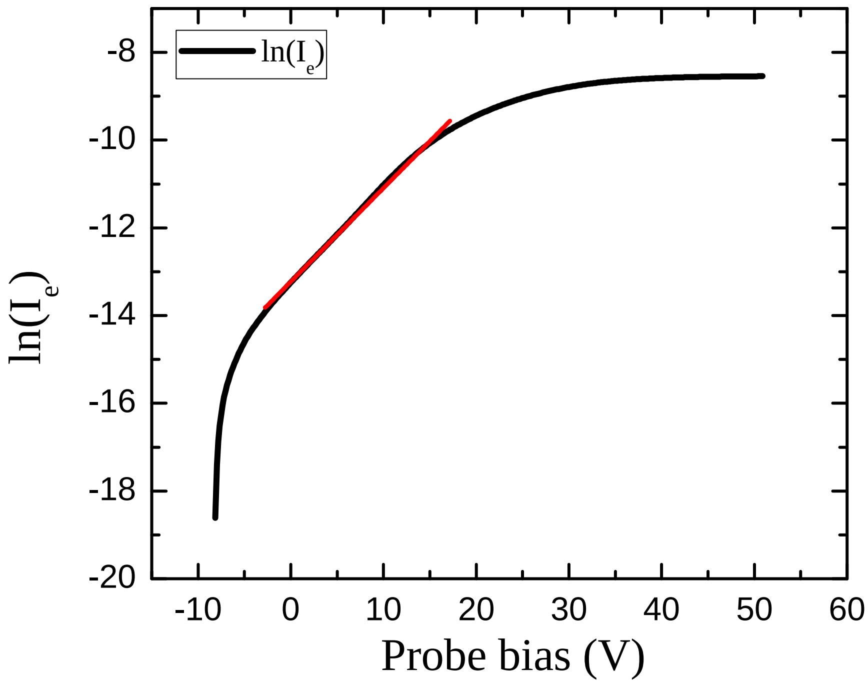

Figure 2.10: Semilog plot of the electron current collected by the Langmuir probe.

expansion of sheath around the probe [164]. Further, the extrapolated ion current is subtracted from the entire probe current ($I_e + I_i$) for getting the better data for the semilog electron current curve [166], which is depicted in Fig. 2.10. The inverse of the slope of fitted line (red line) of $ln(I_e)$ vs V_b plot gives the T_e. Thus, plasma density and electron temperature are calculated using the above said procedures for a given discharge parameters.

2.4.2 Double probe

In the inductively coupled (RF) discharge plasma, the time varying potential influences the electron retardation region of the I-V characteristic of a single Langmuir probe which can cause an overestimated value of T_e [167]. To avoid this situation, double probe method [158, 168] is used to measure the T_e and n. It can also be used to measure the same of plasma, where the reference point is not available. The theory of the current collection is similar to that of the single Langmuir probe (SLP) but the current is limited to the ion saturation current for both positive and negative voltages. Therefore, the plasma perturbation or theoretically uncertainties at larger electron current (in the case of SLP) are avoided. A double probe consists of two identical single Langmuir probes with two assumptions: First, tips of probes should be far enough from each other so that overlapping of the sheath of an individual probe does not occurs. Second, both probes should not be so far that they sample the different plasma regions.

To characterize the inductively coupled diffused plasma, a double probe made of two identical tungsten wires of 9 mm length and 0.5 mm diameter with interspacing of 7 mm is used. Both wires are fed through separately in each bore of a two bore ceramic tube of length 20 mm and an outer diameter of 6 mm. These wires (probes) are connected with copper wire inside the each of bore, which comes out through a BNC connector mounted on an SS 304 shaft of outer diameter 5 mm. Both the ceramic tubes and SS shaft are connected with a Teflon bush. The SS shaft is introduced into the experimental chamber through a vacuum feedthrough. An approximately 8 mm tip of each symmetric wire (probe) is exposed to the plasma for the collection of charged particles.

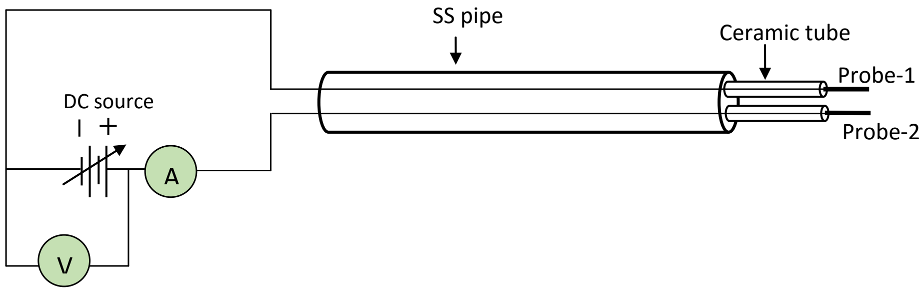

Figure 2.11: Schematic diagram of the double Langmuir probe.

A DC voltage source (series of DC battery of rating 12 V and 0.5 A) and a potentiometer (0–100 kΩ) in the series of a 5 kΩ are used as a floating DC voltage source. For manual scanning of the current flowing into the probes for applied dc voltage difference of -35 V to +35 V is measured across a 5 kΩ resistor. The schematic diagram of a double Langmuir probe with its electrical circuit arrangement is displayed in Fig. 2.11. The working principle of the double probe is based on the Kirchhoff's current law, which states that at any instant the total net current of positive ions and electrons flowing to the system from the plasma must be zero. The details on the current flowing in circuit (I_d) at various differential voltage ($V_d = V_2 - V_1$) is reported by Johnson and Malter [168]. Fig. 2.12 shows the schematic representation of the flowing current in the double probe circuit. The V_1 and V_2 represent the probe potential with respect to the plasma potential.

The electron and ion currents flowing through probe-1 (I_{p1}) and probe-2 (I_{p2}) are represented by $I_{e1}, I_{e2}, I_{i1}, I_{i2}$, respectively. Since, the system is floating; therefore, the total current through the probe circuit is zero [158, 169]

$$\Sigma I_p = I_{p1} + I_{p2} = I_{i1} - I_{e1} + I_{i2} - I_{e2} = 0 \tag{2.8}$$

Now the current in loop can be written as

$$2I = I_{i2} - I_{e2} + I_{e1} - I_{i1} \tag{2.9}$$

From Eq. (2.8) and (2.9), we get the current I in the loop

$$I = I_{e1} - I_{i1} = I_{i2} - I_{e2} \tag{2.10}$$

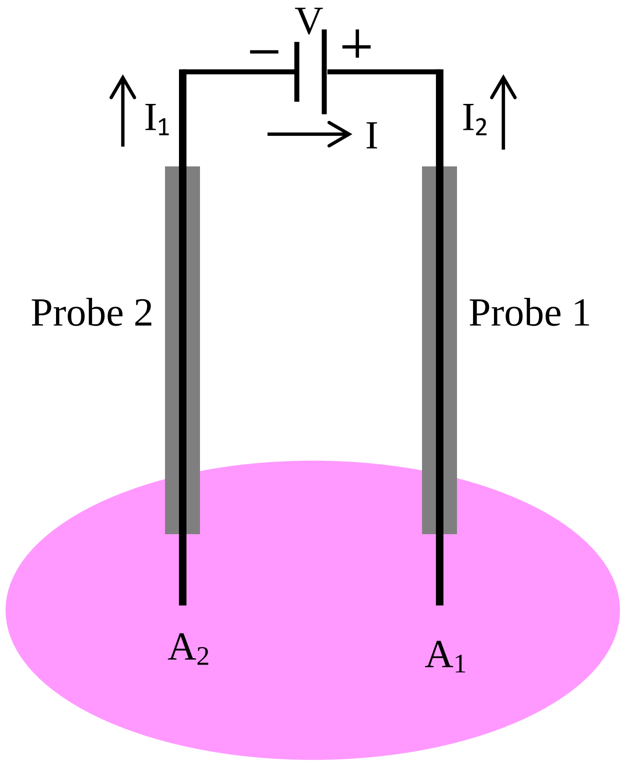

Figure 2.12: Schematic representation of the flowing current in the double probe circuit.

The electron currents are given as

$$I_{e1} = A_1 J_{e0} exp\left(\frac{-eV_1}{k_B T_e}\right), I_{e2} = A_2 J_{e0} exp\left(\frac{-eV_2}{k_B T_e}\right), \tag{2.11}$$

where $A1$ and $A2$ are the area of the probe–1 and probe–2 and J_{e0} is the electron random current density. The plasma environment around the both probes is considered same.

Substituting Eq. (2.11) into (2.10), then Equation (2.10) becomes as:

$$\frac{I + I_{i1}}{I_{i2} + I} = \frac{A_1}{A_2} exp\left(\frac{eV_d}{k_B T_e}\right), \tag{2.12}$$

where $V_d = V_2 - V_1$ is the difference voltage between both probes. Since, both probes are symmetric, i.e., $A_1 = A_2 = A$; therefore, $I_{i1} = I_{i2} = I_{is}$, then the simplified form of Eq. (2.13) using the identity of $tanhx$ is

$$I = I_{is}\ tanh\left(\frac{eV_d}{k_B T_e}\right), \tag{2.13}$$

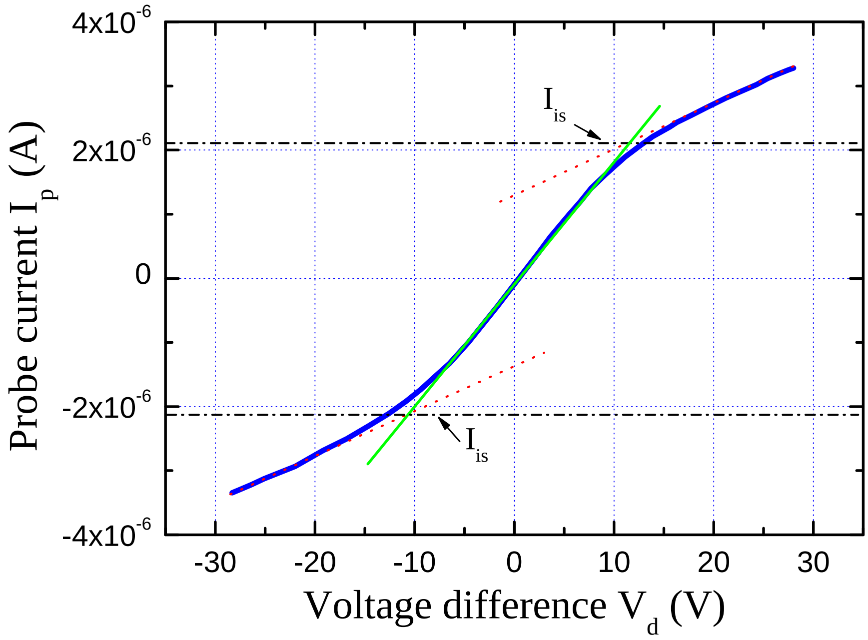

Figure 2.13: I–V characteristic of the double probe.

Differentiating Eq.(2.14) with respect to V_d near the zero point in Fig. 2.13, i.e., at $V_d = 0$, we get

$$\left(\frac{dI}{dV_d}\right)_{V_d=0} = \frac{eI_{is}}{2k_BT_e} = \frac{I_{is}}{2T_e(eV)} \tag{2.14}$$

The I-V characteristic of the double probe observed at discharge parameters (p = 0.04 mbar and P = 7 W) is depicted in Fig. 2.13. We can calculate the electron temperature (T_e) by just finding the slope of the green line passing through the origin (at $V_d = 0$) of the I-V characteristic as shown in Fig. 2.13. The plasma density (n) is determined by using the measured value of ion saturation current (I_{is}) and electron temperature (T_e) in Eq. (2.3).

2.4.3 Emissive probe

An accurate measurement of the plasma potential from the I-V characteristic of a cold probe is sometimes difficult to get the information of the electric field; therefore, an electron emitting probe (emissive probe) has been used to measure the plasma potential or space potential [164, 170]. The measurements are taken from the emissive probe are not sensitive to plasma flow and beams because it directly depends on the plasma potential rather than electron kinetic energy. An

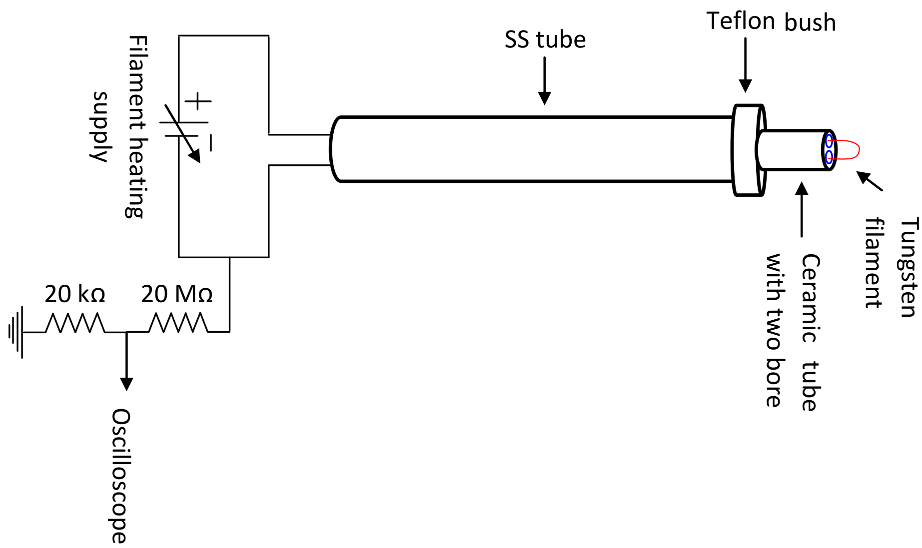

Figure 2.14: Schematic diagram of the emissive probe.

emissive probe is essentially a hot tungsten wire (in hairpin form) inserted into the plasma to measure the plasma potential. There are three methods for measuring the plasma potential such as floating potential method [171, 172], inflection point method [173] and separation technique [174]. In our experiments, the simplest method "floating potential method" is adopted to measure the plasma potential [175]. In this method, floating potential of the probe (V_f) is shifted to the plasma potential (V_p) when it starts to emit [170].

To construct an emissive probe, a tungsten wire of 10 mm length and 0.125 mm of diameter is bent in the form of a hairpin. The tungsten wire tips are inserted in a miniature two bore ceramic cylinder. The copper wire inside the ceramic cylinder makes compression contact between the leads of the wires connected to the heating power supply and the tungsten filament. A DC floating power supply (30 V and 30 A) is used to heat the tungsten loop (emissive probe). The floating potential of the emissive probe is estimated from the measured potential (voltage) drop across a 20 kΩ resistor, which is connected in series with a 20 MΩ resistor. Fig. 2.14 shows the schematic diagram of an emissive probe with electrical circuit arrangement.

Initially, when the probe is cold then there is no electron emission from the filament. When it is heated then it emits electrons into the plasma and with increasing filament heating current, electron emission increases. As the more elec-

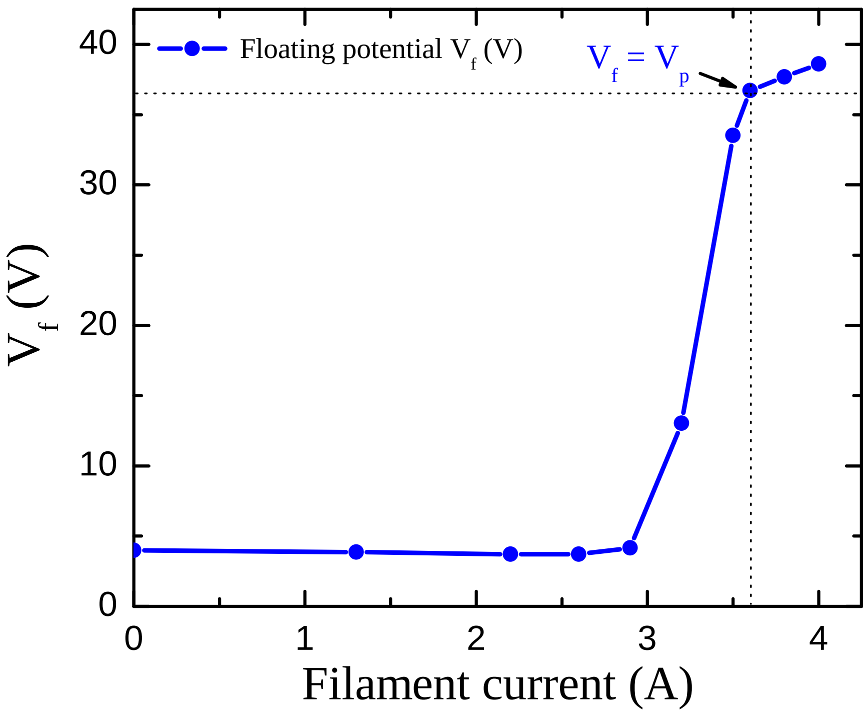

Figure 2.15: The variation of floating potential of the emissive probe with the heating current.

trons are emitted from the filament surface, the potential on it becomes more positive. Hence the potential difference between the probe and the plasma decreases. When heating is more then filament potential (V_f) reaches close to the plasma potential (V_p) and electron emission from heated filaments stops because the emitted electrons will be confined near the filament surface regime and creates a space charge, which will not allow further electrons to emit from the filament surface. This value of floating potential is equivalent to the plasma potential at that location. After this strong emission point, increasing the emission only slightly changes the floating potential due to the space charge effect [170]. This characteristic is shown in Fig. 2.15. The floating potential get saturated at the filament current of $\sim$ 3.6 A which gives the plasma potential, V_p of $\sim$ 37 V at this location.

2.5 Dust grain diagnostics

Video imaging is a primary diagnostics tool to characterize the dust grains dynamics. It involves the processes starting from the illumination of dust grains to transformation of data to the computer. In our case, there is a provision to capture the digital images directly rather than videos. These still images are further processed using standard image analysis software (ImageJ) and MATLAB based software (PIV). To understand the dust grains dynamics, following steps are taken into account

2.5.1 Imaging

The levitated or confined dust particles are illuminated by using the combination of a Laser and plano–convex cylindrical lens. Specifications of the Laser (model-LSR635NL-100) used for the present experiments are given in table 2.1. The output of the Laser is in the form of a beam of $\sim$ 3 mm diameter. For converting this beam in the shape of a sheet (for illuminating a large number of dust particles in a plane), a plano–convex cylindrical lens is used. The circular Laser beam is converted into a sheet when it passes through a cylindrical lens. There is a provision to convert the beam into a vertical or horizontal sheet of Laser light. The specifications of the cylindrical lens (Newport corporation make) is given in table 2.2.

Table 2.1: Specifications of the DPSS Laser.

Laser type	Diode–Pumped Solid State (DPSS) red Laser
Wavelength (λ)	633$\pm$0.5 nm
Output power	0–100 mW (variable)
Beam diameter	$\sim$ 3 mm

Table 2.2: Specifications of the cylindrical lens.

Lens material	BK7 MgF_2 coated
Focal length (f)	25 mm
Back focal length (BFL)	17.74 mm
Lens diameter	25 mm
Clear aperture	24 mm
Radius (R)	$\sim$ 13 mm
Center thickness	11 mm

Table 2.3: Specifications of the CMOS and CCD cameras.

Camera type	CMOS (Lt-225C)	CCD (GEV–B2320C)
Sensor type	Color CMOS	Color CCD
Resolution (pixels)	2048 × 1088	2336 × 1752
Frame rate	170 fps	16 fps (max. 122 fps)
Pixel size	5.5 μm × 5.5 μm	5.5 μm × 5.5 μm
Wavelength range	350–900 nm	350–900 nm
Bit depth	8 or 12–bit	12 bit
Electronic shutter	26 μ s to 4000 ms	1 μ s to 16 s
Data interface	USB.3	GigE Vision
Transfer rate	> 1500 mbps)	> 1600 mbps
On-board memory and RAM	128 MB	128 MB and 256 MB

The Laser sheet is introduced into the experimental chamber for illuminating the dust cloud through one of the axial or radial ports. The scattered light is captured by a CCD or CMOS camera. The intensity of the scattered light is determined by Mie–scattering theory [176], which is applicable for the particle size larger than the wavelength of the incident radiation. The intensity of the scattered light is maximum in the forward direction than in reverse (or in other) direction and it is more for the bigger sized particles. In the present experimental work, color CMOS (Lumenera make Lt-225C) and CCD (IMPERX make GEV-B2320C) cameras are used to capture the dust dynamics at a comparative fast time scale and slow time scale, respectively. The specifications of both cameras are given in table 2.3.

2.5.2 Magnification of the object

A macro zoom lens (model-ZOOM 7000 NAVITAR) of variable focal length (18–108 mm) is attached to the CCD camera for a close look of the dust grains dynamics during the experiments. The zoom lens has the capacity to magnify the object 6X time, which comes from the ratio of their longest (108 mm) to shortest (18 mm) focal lengths. The maximum field of view at minimum zoom mode is $\sim$ 150 mm × 75 mm and it reduces to $\sim$ 25 mm × 12.5 mm at maximum zoom mode. The magnification strength of the zoom lens increases with the increase in the focal length of the lens system. It is possible when a C–ring of 3 mm width is inserted between the CCD camera and zoom lens.

2.5.3 Data storage

The CCD or CMOS camera has an inbuilt analog to digital converter, which digitizes the analog signal of the CCD camera to binary data. These digitized data are first stored in the on–board (head) memory of camera and later transfered to the computer through the Ethernet cable (GigE vision). A HP make workstation Z420 (RAM-16 GB, 64-bit operating system) is used to capture the continuous digital data for good quality of the digital video recording. To increase the data transfer rate, a Solid–State Drive (SSD) instead of Hard Disk Drive (HDD) is used to store the digital data. These digital data (images) are displayed on the monitor of the computer in the format of MPEG and can be saved in SSD of the computer in the JPEG or BMP format. The video capturing software has many facilities for the recording and storage of the video images. It is possible to change the digital gain, exposer time, resolution of images etc. This data capturing software has an option to save the data in the form of a video or digital images.

2.5.4 Image analysis

After capturing the video images of the dust cloud, it is analyzed to extract the meaningful information from the images. A java based software named as **ImageJ** [177] is used to analyze these images. This software is useful to edit the images such as subtracting the background noise, conversion from RGB to 8–bit gray images, brightness and contrast modification, making a composite image, mathematical operations on still images etc. The time-dependent phenomena of the dusty plasma medium are extracted by either superimposing the consecutive frames (images) or intensity plot of the consecutive frames using the ImageJ software. The wave parameters are measured from the pixel intensity vs. pixel position plot of consecutive frames. The spatial separation between two peaks gives the wavelength (λ) while shifting distance of wave over the consecutive frame gives the phase velocity (v_{ph}) of the wave. The frequency of the wave (f) is estimated from the known values of wavelength and phase velocity by the relation ($f = v_{ph}/\lambda$). In addition to ImageJ software, MATLAB based programs are also used to extract the wave parameters, to calculate the inter–particles distance or dust density, and to get the information on physical state of the dusty plasma.

Another MATLAB based open access software, Particles Image Velocimetry, called openPIV [178] is used to identify the directional flow of the dust particles. Normally, PIV technique is a cross-correlation technique for determining the displacement of particles between the pair of images. Thus, the direction as well as magnitude of the velocity vector can be determined using the PIV analysis [21] on the still images. For conducting the PIV analysis, images with illuminated dust grains are decomposed into similar interrogation cells with the dimensions of $m \times m$ pixels. There should be a finite number of particles within each cell. To calculate the displacement vector, cross-correlation is constructed for the corresponding cells on two images. From their displacement and the known time interval, 2D velocity vectors can be computed. These velocity vectors are based on the cross–correlation of the intensity distribution over small interrogation cells of the images with grain flow. By progressively decreasing the interrogation cell size, a better resolution can be achieved; therefore, multi–pass correlation technique is used.

3

Dust Acoustic Wave and its Propagation Characteristics in Presence of a Floating Object

In this chapter, experimental observations of self-excited dust acoustic wave and its propagation characteristics in presence of a floating object (an electric perturbation) in the DC glow discharge plasma are presented. The qualitative description on modification of propagation characteristics of the waves on the basis of coupling between the sheath around the cylindrical object and the cathode sheath is also discussed.

3.1 Introduction

The investigation of the waves in dusty plasma medium has attracted considerable interest in the last couple of decades because the self-excited waves are an important element of the self-organization in nature [179]. Similarly, the patterns are observed in plastic deformation flows [180], hydrothermal flow [181], rhythmic patterns of mobile marine sand, [182] and sand ripples [183]. Also, many fundamental quantities for characterization of the dusty plasma can be obtained from the analysis of wave propagation characteristics. The dust acoustic wave (DAW) is very low frequency (< 100 Hz) collective mode of the dusty plasma, which has been widely studied theoretically and experimentally [1, 2, 4, 20, 96, 113, 184]. It is a modified version of the usual ion acoustic wave of conventional two-component plasma but here inertia is provided by the massive charged dust grains and the thermal pressure to sustain the wave is provided by the electrons and ions. To understand the underlying physics of the propagation characteristic of such low-frequency modes, various experimental configurations have been employed to create the dusty plasma in both DC and RF discharges [3, 20, 110, 111, 185].

In the laboratory plasma, these modes are either excited by external means [2,186,187] or they occur spontaneously below a critical neutral pressure [1,107,110, 114]. It has been experimentally shown in most of the studies that the self-excited dust acoustic waves in DC or RF discharge dusty plasma are the consequence of the streaming ions through the dust cloud [22, 23, 117–119], dust charge variation in the confined dust cloud [188], or spatial charge gradient of dust particles [27]. At higher neutral gas pressure, the dissipation losses due to the dust–neutral collisions increases and dust modes get damped. Hence, the spontaneous excitation of DAW is possible below a certain threshold pressure. Close to the threshold pressure, the observed waves have linear characteristics but below the threshold, the dust mode can acquire large amplitude due to the less damping and nonlinear effects. As it has been discussed that instabilities associated with streaming ions through dust cloud cause the excitation of dust acoustic modes. The self-excited waves usually propagate parallel to the ion streaming direction. It essentially signifies the role of ion dynamics over the collective dynamics of dusty plasma in the DC glow discharges. Due to an external time-dependent electric perturbation, these modes get synchronized because of an external time varying potential perturbation that modulates the ion density [189, 190]. In the case of the stationary (time-independent) electric perturbation, which can be applied using a floating or biased object, different kind of dust motions have been reported in the various dusty plasmas.

In general, it is observed that a dust-free region (void) is formed around a floating object inserted inside the dusty plasma. The interaction of an electrically floating metal cylindrical object with a dusty plasma, which is formed in an anode trap was investigated by Thompson *et al.* [123]. When the object was at rest, a dust-free cavity (void) is formed around an object. At the moderate speed (subsonic speed) of the probe, a similar dust-free region was observed. The dust void around a negatively biased cylindrically probe and its size dependence on the bias voltage was examined by Thomas *et al.* [14]. The dust cavity around a biased probe in an rf produced plasma under the microgravity condition was studied by Klindworth *et al.* [125]. Kim *et al.* [16] experimentally investigated the interaction of dust acoustic waves with a floating cylinder in the DC discharge and they reported the diffraction of these waves. Interaction of flowing dusty plasma, confined in an rf sheath, with a stationary biased wire gives rise to some nonlinear collective modes [126]. When dust medium is strongly coupled (crystalline state) then observed collective dynamics of the dust grain medium due to the electric perturbation through a biased probe was different. The biased probe alters the crystalline state of grain medium and as a result, dust grains were found to circulate in the perturbed region [15]. The modification of dust dynamics during the floating or biased object interaction with a dust plasma system is mainly a consequence of the modification of the spatial potential or electric field distribution and ion number density distribution in the interaction (perturbed) region. Most of the previous studies on the dust acoustic waves and its interaction with the object were carried out in anode trap dusty plasma, which has been discussed in Chapter 1. The detailed nature of the dust acoustic waves and its propagation characteristics in presence of an external electric perturbation in the DC glow discharge (cathode trap) 3D dusty plasma is still an unexplored problem.

In this Chapter, the excitation of dust acoustic waves in a DC discharge (cathode trap) plasma and its propagation characteristics in presence of an external electric perturbation, which is applied using a floating object, have been studied. The chapter is organized as follows: Sec. 3.2 deals with the detailed description of the experimental setup. Sec. 3.3 describes the plasma production and its characterization. A detailed description of dusty plasma production and its characterization are provided in Sec. 3.4. The experimental observation of dust acoustic waves and its characteristics are discussed in Sec. 3.5. Sec. 3.6 highlights the detailed characteristics of DAWs in presence of a floating rod. A brief summary of the work along with a concluding remark is provided in Sec. 3.7.

3.2 Experimental setup

Experiments of dust acoustic waves are performed in a borosilicate glass tube with an inner diameter of 15 cm and length of 60 cm. A rotary pump and gas dosing valve are attached to a stainless steel (SS) buffer chamber, which is connected to the glass tube. The details of the experimental setup is described in section 2.2. The schematic diagram of an operating configuration is presented in Fig. 3.1. A SS cylindrical rod of 5 mm diameter is inserted in the experimental chamber over the cathode using a Wilson feedthrough. The experimental chamber is evacuated $\sim 10^{-3}$ mbar pressure using a rotary pump and the argon gas is then fed into the chamber. The chamber is then again pumped down to the base pressure of $\sim 10^{-3}$ mbar. This process is repeated several times to reduce the impurities from the vacuum vessel. Finally, the operating pressure is set to 0.07 mbar by adjusting the gas dosing valve. The selection of operating pressure at 0.07 mbar is discussed in section 3.4.

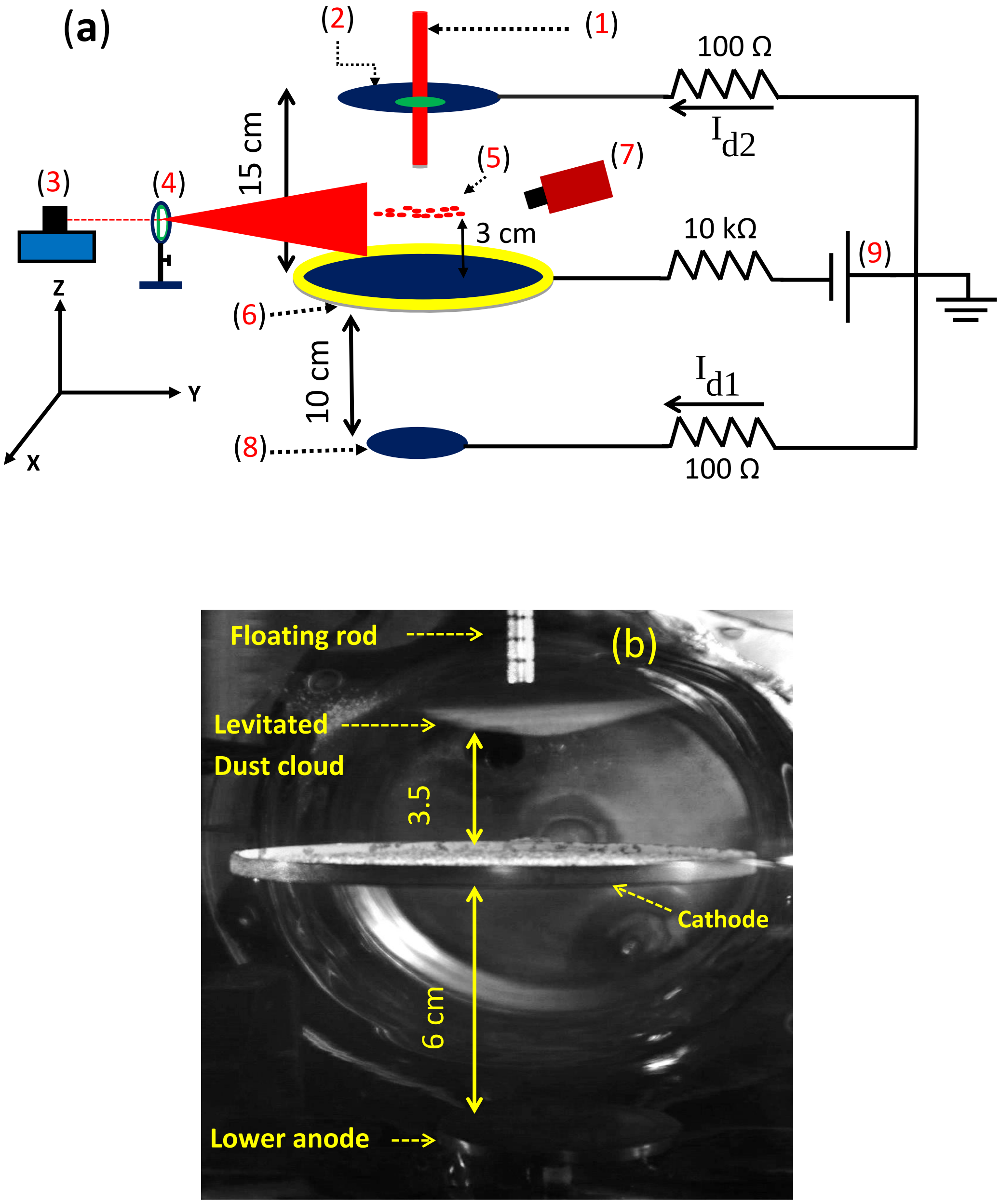

Figure 3.1: (a) Schematic diagram of experimental configuration:(1) Cylindrical rod, (2) stainless steel(SS) flange (working as an anode), (3) solid-state red laser, (4) plano-convex cylindrical lens, (5) kaolin dust particles, (6) SS disk electrode (cathode) with a ring like step at corner (represented by yellow ring), (7) CCD camera, (8) stainless steel circular electrode (anode), (9) discharge power supply. I_{d1} and I_{d2} represent the currents flowing in separate discharge path. (b) A full view image of the dust cloud with a cathode and anodes.

3.3 Plasma production and its characterization

To produce the dusty plasma using cathode trap, the DC glow discharge is initiated by applying the DC voltage between a cathode and anodes, as shown in Fig. 3.1(a). The plane surface of the cathode is parallel to the lower anode, which is kept 10 cm below from the cathode. The upper anode is a SS flange of 7 cm diameter, which is kept parallel to the dust particles containing cathode surface at 15 cm. This configuration of anodes and cathode demands minimum voltage to breakdown the argon gas. Both the anodes are kept grounded through a resistance of R=100 Ω to measure the discharge current in each path. The experimental chamber is purposefully made of dielectric material and all the axial and radial ports are closed by toughened glasses and/or perspex flanges to avoid other discharge current paths. There is an advantage to using this discharge configuration for performing dusty plasma experiments, which is explained below. The dust particles are sprinkled homogeneously over the cathode surface which acts as a dielectric covered electrode. For the breakdown of gas, negative bias is applied to the cathode with respect to the grounded anodes. In the absence of the lower anode, 30−40 V more bias voltage is required to breakdown the gas and as a result, it becomes difficult to form an appropriate dusty plasma at lower gas pressure. The mechanism for the gas breakdown has been described in section 2.3.

The plasma parameters at various discharge conditions are measured using a single Langmuir probe (discussed in subsection 2.4.1). The variations of plasma parameters with discharge voltage are displayed in Fig. 3.2. The plasma density (n) and the electron temperature (T_e) change from $\sim 1{\times}10^8$ to $7{\times}10^8$ cm^{-3} and $\sim$ 3 to 5 eV respectively with the change of discharge voltage from 380 to 540 V at a constant pressure, p = 0.07 mbar. The measured values show that the plasma density increases, whereas the electron temperature decreases with the increase of discharge voltage. For a given discharge condition, the plasma parameters are measured outside the sheath region where dust particles are found to be confined. Since, the dust cloud is not too much extended in the vertical direction ($-\hat{z}$) to the cathode surface; therefore, plasma parameters are considered to be nearly uniform along the width of dust cloud. The measured plasma parameters at given discharge condition are used to estimate the parameters of the dusty plasma.

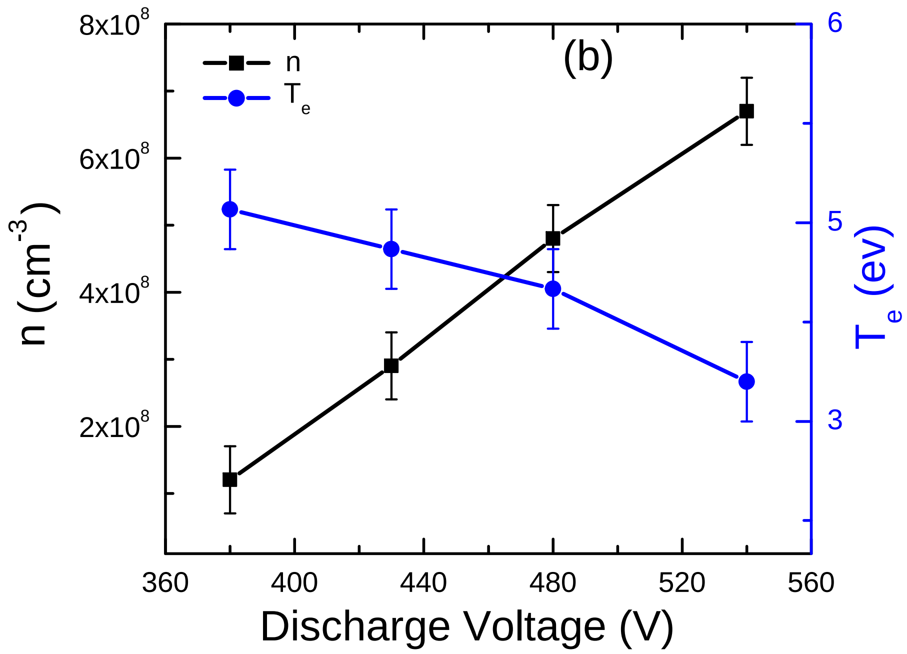

Figure 3.2: Variation of plasma density (n) and electron temperature (T_e) with the discharge voltage. The argon gas pressure is set to 0.07 mbar during the measurements.

3.4 Dusty plasma and its characterization

In course of dusty plasma experiments, kaolin dust particles with mass density (ρ) of 2.6 gm/cm^3 and radii (r_d) ranging from $\sim$ 0.5 to 5 μm are sprinkled over the cathode surface. For producing the dusty plasma, DC glow discharge is initiated between the cathode and anodes at argon pressure of 0.07 mbar. The discharge current–voltage characteristics in the presence of dust particles follow the similar trend as shown in Fig 2.6 but with slightly lower values of discharge current (I_{d2}). In the background of plasma, dust particles get negatively charged because of impinging of more electrons than ions on the surface of dust particles. The negatively charged dust particles get lifted up from the cathode surface and levitated at the interface of plasma and cathode sheath region. The cathode geometry (ring at its periphery) provides the radial confinement to the levitated dust particles. The levitated dust cloud is then illuminated by a red laser of 632 nm wavelengths and power range from $1-100$ mW. The Laser beam is converted into a Laser sheet using a plano-convex cylindrical lens of the focal length of 25 mm, which can be oriented in vertical as well as in horizontal plane. This laser sheet is efficient enough to illuminate ~ 3 mm wide vertical (or horizontal) slice of the dust cloud. Due to the poly-dispersive nature of the particles, the heavier dust particles levitate at the bottom whereas the lighter particles levitate at the top of the sheath by balancing the electrostatic force and the gravitational force. An image that shows a snapshot of the levitated dust cloud over the cathode is shown in Fig. 3.1(b). During the experiments, we always shine the mid-plane of the dust cloud by the Laser sheet; therefore, particle of average size ($r_d \sim 3$ μm) are considered for the theoretical estimations of wave properties [1,5,110]. The dynamics of the particles in vertical as well as in horizontal plane are recorded at 130 frames per second (fps) by a color CMOS camera of resolution 1088×2048 pixels. The data is then transferred to a high-speed computer for the purpose of further analysis using different software.

The effect of discharge parameters on the levitated dust cloud is also necessary to understand the propagation characteristics of DAWs. Therefore, the sheath thickness and the width of the dust cloud are measured at given pressure for various discharge voltages. The sheath thickness is estimated by measuring the distance between the cathode and the topmost layer of the levitated dust particles, whereas the difference of topmost and the bottommost layers gives the width of dust cloud. The sheath thickness is found to decrease with the increase of the applied discharge voltage as shown in Fig. 3.3 (represented by solid rectangles). The sheath thickness (s) in our experiments varies from ~ 40 to 30 mm in the range of discharge voltage 400 V to 490 V. As sheath thickness reduces, the electric field gradient at sheath edge increases; therefore, the dust cloud get suppressed. The variation of the width of the dust cloud with discharge voltage is shown in Fig. 3.3 (represented by a closed circle).

The observed larger sheath dimension is expected at low pressure [191]. However, this approach fails to give an exact value when the experiments are performed with large number of particles. In that case, the dust particles can enter into the plasma due to the mutual repulsion. Although, an approximate sheath dimension can be estimated using this approach with an error of 5-10%. According to the Child-Langmuir law [56], the cathode sheath thickness is a direct function of the electron Debye length λ_{De}. In order to relate the measured sheath thickness in terms of λ_{De}, a theoretical model given by Sheridan and Goree [192] is used. This model describes the sheath around a negatively biased electrode introduced

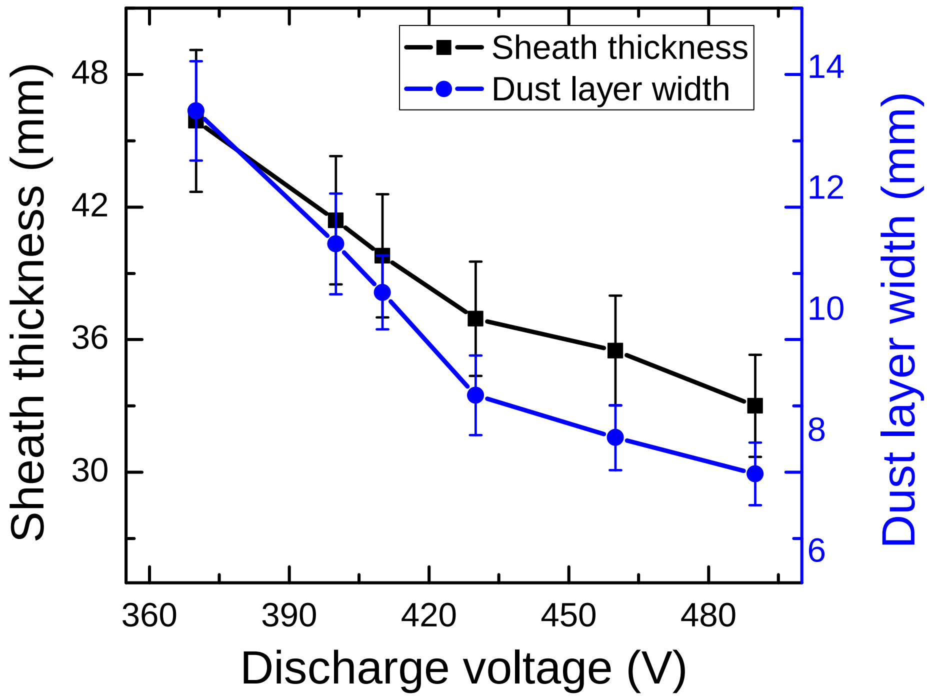

Figure 3.3: Variation of sheath thickness (solid rectangle) and dust cloud width (closed circle) with applied discharge voltages. The argon filling pressure during the experiment is set at 0.07 mbar.

into the plasma in the collision dominated regime. In their model, the collision parameter ($\alpha = \lambda_{De}/\lambda_i$) defines the number of collisions in a Debye length λ_{De}, where λ_i is mean free path for ions to transfer their momentum to the neutrals. At a background pressure of 0.07 mbar, λ_i comes out to be ~ 0.6 mm, which gives $\alpha \sim 2-1$ for the range of $\lambda_{De} \sim 1.2-0.6$ mm (estimated from the plasma parameters given in Fig. 3.2(b)). According to our experimental conditions, the above model estimates the sheath thickness $\sim$ 40 to $60\lambda_{De}$ for the value of $\alpha \sim 1-2$. The measured sheath thickness in our experiment also shows a similar value $\sim$ 35 to $50\lambda_{De}$ for the same discharge condition, which is in close agreement with the estimated value from the theoretical model [192]. If the collision parameter, α is set to zero (collisionless sheath) in this model, simplified Child's law [193] can be recovered which has widely been used for various plasmas with different electrode configurations. For an example, Lisovskiy *et al.* [191] employed the Child-Langmuir law to compare the higher value of sheath thickness obtained in the experiments for a collision dominated sheath around a powered cathode, which is similar to our experiments.

3.5 Results on the dust acoustic waves

In this section, excitation and propagation of the self-excited dust acoustic waves and its dispersion relation are discussed.

3.5.1 Excitation of dust acoustic waves

The dust particles are found in equilibrium state approximately at 40–45 mm above the cathode at $V_d = 340$ V and $p = 0.07$ mbar. If the discharge voltage is increased slightly beyond the $\sim$ 350 V, an appearance of DAW in the dust cloud is found. This wave originates in the upper part of the levitated dust cloud and propagates towards the cathode (along the gravity). A typical video image of this self-excited DAWs in the Y-Z plane at $V_d = 380$ V and $p = 0.07$ mbar is depicted in Fig. 3.4(a). The stable dust cloud shows the excitation of spontaneous dust acoustic wave when the ratio E/p crosses a threshold value [22]. This ratio increases either with the increase of electric field (or the discharge voltage) or decrease of gas pressure. At higher pressure and higher discharge voltage, the wave could not be excited due to frequent ion-neutral collision; whereas, at higher discharge voltage and lower pressure, the dust acoustic wave gets highly unstable [110]. Hence considering these two points, a constant pressure, p = 0.07 mbar, is chosen to perform the experiments at a range of discharge voltage of 350 V to 550 V. The average intensity profile of scattered Laser light coming from dust grains (Fig. 3.4(a)) is shown in Fig. 3.4(b). It is observed from Fig. 3.4(b) that the wave initially gets excited with smaller amplitude on the top and then propagates with increasing amplitude.

3.5.2 Dispersion relation of dust acoustic wave

The dust acoustic wave was modeled as a linear, one-dimensional compressional wave in which the charged dust grains are considered as medium for the propagation of waves [43, 96]. The dust acoustic wave dispersion is derived by assuming that the electron and ion densities are given by Boltzmann distributions $n_e = n_{e0}e^{e\varphi/k_BT_e}$ and $n_i = n_{i0}e^{-e\varphi/k_BT_i}$, with electron and ion temperatures T_e and T_i, respectively. All the species (electrons, ions and dust grains) are taken to be at rest and homogeneous in zero order and dust charge $Q_d = -eZ_d$ is assumed to be constant. The dust grain medium is assumed to be composed of the cold dust grain ($T_d = 0$). Furthermore, it is assumed that the dust grain obeys the continuity and momentum equations and are closed by Poisson's equation. These equations are

$$\frac{\partial n_d}{\partial t} + \frac{\partial n_d v_d}{\partial z} = 0, \tag{3.1}$$

$$n_d \frac{\partial v_d}{\partial t} + n_d v_d \frac{\partial v_d}{\partial z} = -\frac{n_d Q_d}{M_d} \frac{\partial \varphi}{\partial z}, \tag{3.2}$$

$$\frac{\partial^2 \varphi}{\partial z^2} = -\frac{1}{\epsilon_0} \left(e n_i - e n_e - n_d Q_d \right), \tag{3.3}$$

where n_e, n_i, and n_d are the electron, ion, and dust densities respectively, v_d is the dust fluid velocity, M_d is the mass of dust grain, φ is the electrostatic potential or wave potential, and k_B is the Boltzmann constant. These equations take the form after first order linearization with above mentioned assumptions

$$\frac{\partial n_{d1}}{\partial t} + \frac{\partial n_{d0} v_{d1}}{\partial z} = 0, \tag{3.4}$$

$$M_d \frac{\partial v_{d1}}{\partial t} = e Z_d \frac{\partial \varphi}{\partial z}, \tag{3.5}$$

$$\frac{\partial^2 \varphi}{\partial z^2} = -\frac{e}{\epsilon_0} \left(n_{i1} - n_{e1} - n_{d1} Z_d \right), \tag{3.6}$$

where $n_{e1} \approx n_{e0} \frac{e\varphi}{k_B T_e}$ and $n_{i1} \approx -n_{i0} \frac{e\varphi}{k_B T_i}$ are electron and ion number density perturbations, respectively. Assuming $n_{d1} = \hat{n}_{d1} exp(-i\omega t + ikz)$, $v_{d1} = \hat{v}_{d1} exp(-i\omega t + ikz)$ and $\varphi = \hat{\varphi} exp(-i\omega t + ikz)$ are the first-order dust density, dust fluid velocity and wave potential, respectively. Here, ω is the wave frequency and k is the wave vector. The dispersion relation of dust acoustic wave is obtained after combining the fourier transforms of the linearized forms of Eq.(3.4)-Eq.(3.6)

$$\omega = \left(\frac{\lambda_D^2 \omega_{pd}}{1 + k^2 \lambda_D^2} \right)^{1/2} k, \tag{3.7}$$

where λ_D is the dust Debye length and ω_{pd} is the dust plasma frequency. Under the long wavelength limit, where $k^2 \lambda_D^2 \ll 1$, the wave dispersion relationship reduces to

$$C_{DA} = \frac{\omega}{k} = \omega_{pd} \lambda_D = \left(\frac{n_{d0} Z_d^2 e^2}{\epsilon_0 M_d} \right)^{1/2}. \tag{3.8}$$

For the laboratory plasma, where $T_i << T_e$, the dust acoustic speed (phase velocity) reduces to

$$C_{DA} = v_{ph} = \left(\frac{k_B T_i}{M_d} \frac{n_{d0} Z_d^2}{n_{i0}} \right)^{1/2}. \tag{3.9}$$

3.5.3 Characteristics of dust acoustic waves

The spontaneously excited DAWs in the DC glow discharge is mainly due to the ion streaming towards the cathode [22, 23]. The streaming of ions through the cathode sheath is understood in our experiments by quantitative analysis of ion current density at various cathode bias voltages. In the DC glow discharge plasma, the voltage drop across the electrodes is nearly equal to the voltage drop across the cathode sheath. The current drawn by the cathode is mostly due to positive ions, whereas the contribution of electron current is negligible [154]. In present set of experiments, the ion current density varies from $\sim 0.27 \times 10^{-5}\ A/cm^2$ (for $I_{d2} = 0.2\ mA$) to $\sim 1.48 \times 10^{-5}\ A/cm^2$ (for $I_{d2} = 1.1\ mA$) with the increase of bias voltage from 380 V to 540 V (see Fig. 2.6). The current density for ions at cathode sheath edge can be estimated from the measured ion density and electron temperature (using Fig. 3.2) as: $J_i = 0.6en_ic_s$ [56], where c_s is Bohm velocity of ions. Therefore, the current density of ions at sheath edge comes out to be $\sim 0.3 \times 10^{-5}\ A/cm^2$ and $\sim 1.6 \times 10^{-5}\ A/cm^2$ at 380 V and 540 V, respectively. The above estimation shows that the ion flux at cathode sheath edge (entering flux) is approximately equal to that of at the cathode surface for a given bias voltage. This quantitative analysis indicates the conservation of ion flux inside the cathode sheath. Hence, according to the cathode sheath model [56, 194, 195], the acceleration of ions is expected after entering the sheath edge at a given discharge condition. This cathode sheath model is still valid in presence of small particles with certain modifications [196]. Therefore in case of dusty plasma, the ion flux remains constant (with a different value) throughout the cathode sheath, which essentially signifies the acceleration of ions towards the cathode. These streaming ions are the source of free energy to excite the DAWs.

For a given discharge condition when the ions drift towards the cathode through the dust cloud, the strength of ion drag force increases with the increase of ion velocity and particle size [92]. It results in the increase of density fluctuations of DAWs during the propagation towards the cathode. In present sets of experiments,

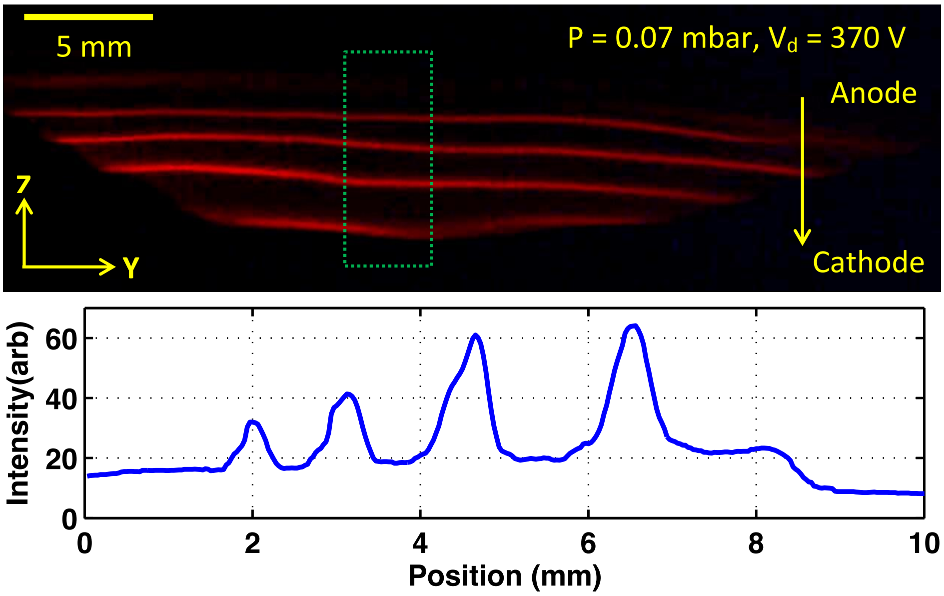

Figure 3.4: (a) Video image of dust acoustic waves in the vertical (Y−Z) plane. (b) Average intensity profile of scattered laser light coming from dust particles (in dotted region) in -$\hat{z}$ direction. The direction of the wave propagation is indicated by the arrow. The data are taken at a discharge voltage and gas pressure of 370 V and 0.07 mbar, respectively.

intensity profile of an equilibrium dust cloud (from topmost to bottommost layer) changes up to ∼1.3 times either due to the presence of bigger dust particles in the equilibrium dust cloud or/and the higher dust density, which can also cause the wave to propagate with higher amplitude. Hence, the higher dust density fluctuations (or amplitude) of DAWs happens during the propagation toward the cathode is either due to the higher equilibrium dust density or/and the presence of bigger dust particles or/and higher drift velocity of ions.

For the detailed characterization of DAWs, few consecutive frames are considered. The time evolution of average intensity profile is shown in Fig. 3.5. The red dashed line in the figure indicates the trajectory of a particular crest of the DAW. The phase velocity (v_{ph}) and wavelength (λ) are found to be $\sim$ 2–3 cm/sec and $\sim$ 1.5–2.5 mm, respectively. The wave frequency (f_d) is estimated from v_{ph} and λ. And it comes out to be $\sim$ 10–15 Hz. It is clear from the figure that distance between two consecutive crests increases with time as the higher (smaller) amplitude wave moves with faster (slower) velocity [5]. The estimated phase velocity (v_{ph}) of the DAW is found to be $\sim$ 3.4 cm/sec for the parameters T_e = 4 eV, T_i = 0.025 eV, M_d (for an average radius $r_d \sim$ 3 μm) $\sim 3\times10^{-13}$ kg, $n_{d0} \sim 1\times 10^4$

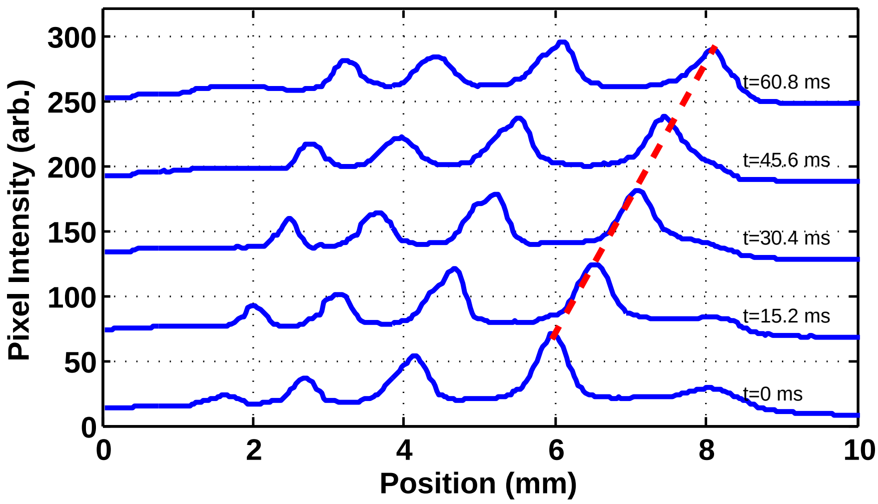

Figure 3.5: Time evolution of intensity profile of five video frames taken at time step of 15.2 ms in the vertical plane. Discharge voltage and argon pressure are set at 370 V and 0.07 mbar respectively for this particular set of experiments

cm^{-3}, $n_{i0} \sim 1\times\ 10^8\ cm^{-3}$, and $Z_d \sim 3\times 10^4$. Therefore, theoretical predicted value of the phase velocity is in close agreement with the measured phase velocity of DAWs in the experiments. As we have discussed, the spontaneous DAWs are observed to propagate from anode to cathode (along the gravity) which essentially in the direction of ion flow. At lower discharge voltage, DAWs are not found to excite because of the smaller values of ion flux and ion drift velocity. When the discharge voltage is increased beyond 350 V, the flux and drift velocity of ions increase due to the more ionization (Fig. 3.2) and higher sheath E-filed (Fig.3.3), which results in the excitation of DAWs. The excitation of DAWs is possible if ion–drift velocity (v_i) becomes in the order or higher than the ion thermal velocity (v_{Ti}) [22, 117, 118], i.e., $v_i \geq v_{Ti}$. In our experiments, the ion thermal speed, $v_{Ti} = \sqrt{(8kT_i/m_i\pi)} \sim 3.9\times10^4$ cm/sec where m_i ($= 6.7\times10^{-26}$ kg) is the mass of argon ions. The ion drift velocity (v_i) can be estimated from, $v_i = \mu_i$E, where μ_i and E are the ion mobility and the sheath electric field, respectively. The sheath electric field is estimated from an equilibrium condition of dust particles, where the gravitational force is exactly balanced by the electrostatic force. Hence at an equilibrium, $eZ_dE = M_dg$, where e ($= 1.6\times10^{-19}$ C) is the electronic charge and g ($= 9.8m/sec^2$) is the acceleration due to the gravity. For a given values of $M_d \approx 3\times10^{-13}$ kg and $Z_d \sim 3\ \times10^4$, the estimated electric field $E \approx 6$ V/cm. The mobility of argon ions $\mu_i \sim 1.8\times10^3$/p(torr) $cm^2s^{-1}V^{-1}$ [197]. At p = 0.07 mbar,

$\mu_i \sim 3.5{\times}10^4\ cm^2 s^{-1} V^{-1}$; therefore, the estimated ion$-$drift velocity, v_i, becomes $\sim 2 \times 10^5$ cm/sec for $E \approx 6$ V/cm. The ratio of v_i/v_{Ti} is ≈ 5. Hence, the above estimation also assures that the ion-dust streaming instability is mainly responsible for the excitation of the DAWs. It is also found that at higher pressure (≥ 0.2 mbar), the ion-neutral collision frequency increases; as a result, the oscillations of dust particles get suppressed due to the frequent ion–neutral collisions (or ion-dust streaming instability suppression) and therefore the waves could not be excited.

3.6 Characteristics of dust acoustic waves in presence of a floating object

In this section, results on the propagation characteristics of dust acoustic waves in presence of a vertically as well as horizontally aligned floating cylindrical object (rod) are presented.

3.6.1 Vertically aligned floating rod

After thoroughly characterization of DAWs, the experiments are carried out to study the modification of its propagation characteristics in presence of a stationary electric perturbation, which is applied by using a floating object. In this set of experiments, a cylindrical rod is chosen as a floating object and introduced inside the plasma perpendicular to the cathode plane as mentioned in section 5.2. The dimension of the rod is taken in such a way that $r \gg \lambda_D$. where, r is the radius of the rod and $\lambda_D \approx \lambda_{Di}$ is the dust Debye length. In our discharge regimes, λ_D varies from 0.04 mm to 0.08 mm. In this regime, it is found that a wire of radius $r \sim \lambda_D$ does not affect (perturb) the dust cloud; therefore, the radius of the rod is chosen bigger in dimension ($r = 2.5$ mm) so that its influence on DAW can be observed. The effective changes in the dust cloud or DAW in presence of a floating cylindrical rod are examined for different discharge voltages at a particular pressure, p = 0.07 mbar. A dust–free region (void) around the floating rod is observed at lower discharge voltage when dust cloud does not exhibit wave structures. This is the case when discharge voltage is ~ 350 V at the pressure, $p = 0.07$ mbar. However, the detailed study of the dust-free region (void) around the floating rod is not the scope of the present study.

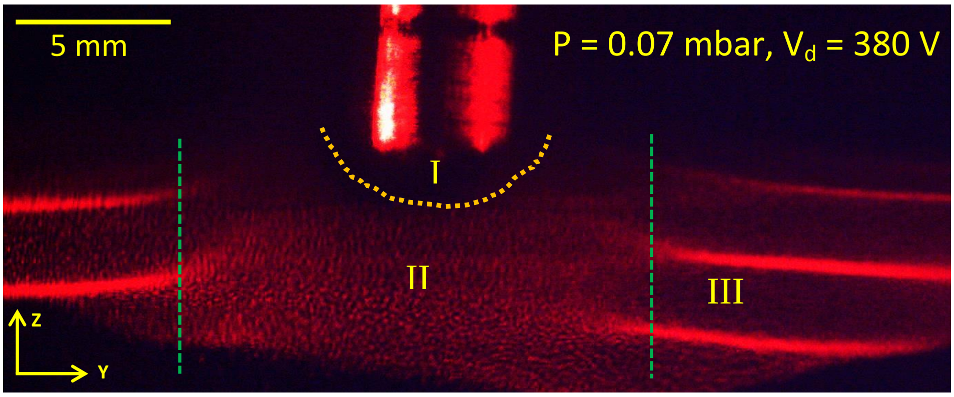

Figure 3.6: A video image of dust acoustic waves in presence of a vertically aligned floating rod. Three distinct regions are observed: (I) Dust void (dotted curve). (II) Stationary dust cloud (region between dotted curve and lines). (III). dust acoustic wave (outside the dotted lines). Argon pressure and discharge voltage are set at 0.07 mbar and 380 V, respectively.

At higher discharge voltage (beyond 380 V), the DAWs exhibit the similar kind of characteristics as discussed in subsection 3.5.1 (Fig. 3.4). When floating rod ($V_f \approx -12$ V) is moved near the upper layer of the dust cloud, the waves get modified in the perturbed region. To study the modification of wave properties, the horizontal (in the X–Y plane) as well as the vertical (in the Y–Z plane) slices of images near the floating rod are captured. A typical image of dust cloud in (see Fig. 3.6) the Y–Z plane shows the influence of cylindrical rod on the propagating DAWs. Few consecutive frames are used to analyze the dynamical behavior of the dust grains near the rod. Three distinct regions are found when the rod is brought near the topmost layer of the dust cloud. These regions are classified as: region–I, dust free region near the rod (between the rod and dotted curve), region–II, stable dust cloud (between the dotted curve and dotted lines) and region–III, dust acoustic wave (outside the dotted lines). The length of dust-free region (length from rod surface to dotted curve) is ≈ 2 mm, whereas the length of the perturbed region (length from rod surface to dotted line) is extended up to $\sim 6-7$ mm. Outside the dust free region (in region–II), the dust grains only show the random motion instead of participating in the propagation of DAW. The boundary of different regions changes with the change of discharge parameters and dimension of the rod.

In the presence of a floating rod, the sheath around it modifies the potential distribution or electric field distribution of the cathode sheath. The resultant

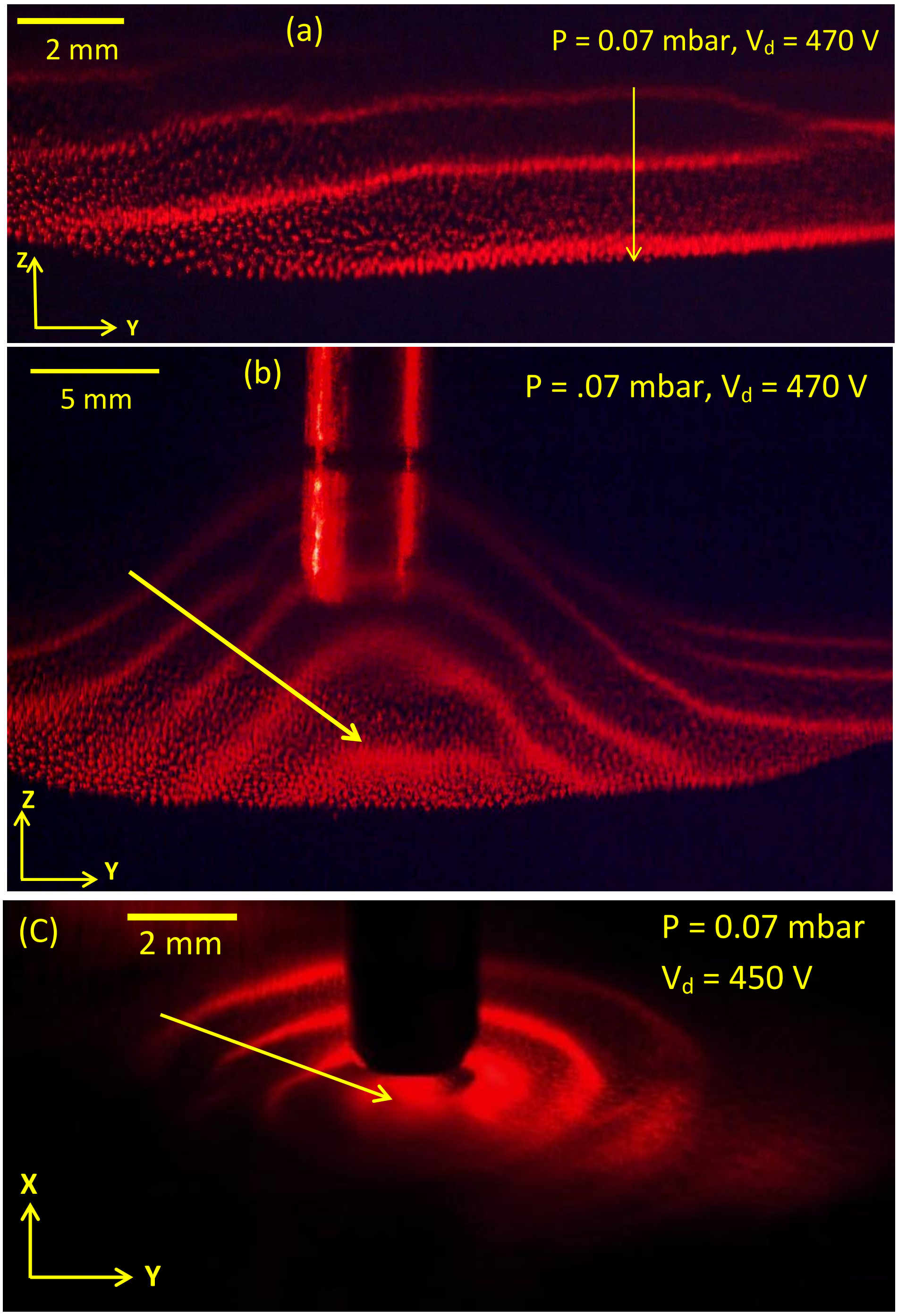

Figure 3.7: (a) A video image of dust acoustic waves in vertical plane (in absence of rod).(b) Image of modified DAWs in vertical (Y–Z) plane with floating rod where discharge voltage is 470 V. (c) A video image of DAWs in horizontal (radial plane of rod) plane just below the floating rod. The direction of propagation in each sub-figure is shown by the arrow.

electric field in the perturbed (interaction) region is the consequence of the coupling between the sheaths formed around the rod and the cathode, which has been investigated in details by Barnat *et al.* [25] in a two component plasma. As a result, dynamics of ions as well as dust particles get modified in the overlapping sheath region. In the region-I, dust grains are expelled near the rod surface due to the strong sheath electric field which causes the formation of dust void [14, 123]. The random motion of dust grains in the region–II is a result of the suppression of ion streaming towards the cathode (along the direction of gravity). It is observed that the instabilities in dust cloud are triggered above a critical electric field [118]. In presence of the rod, the electric field becomes weaker [25] (in the region–II) that causes the suppression of ion-streaming instabilities in the dust cloud and transforms the wave crests into stable dust cloud. In the region–III, the influence of floating rod is negligible therefore the dust cloud exhibits the usual dust acoustic waves.

With the further increase of discharge voltage (beyond 450 V), the DAWs become unstable (see Fig. 3.7(a)) due to the higher value of E/p as reported by Merlino *et al.* [22] but still propagate in the direction of streaming ions (along the gravity$(-\hat{z})$). With the increase of discharge voltage, the sheath thickness reduces to nearly 28 mm (Fig. 3.3), which causes to increase the sheath electric field. Thus, the ratio of E/p increases for a given pressure. In this case, the observed average wavelength and velocity of DAW are $\sim$ 2 mm and $\sim$ 4 cm/sec, respectively.

In this particular discharge condition, when the floating rod with floating potential of $V_f \approx -8$ V is moved from plasma to the upper layer of the dust cloud; a unique feature in the dust cloud adjacent to the object is observed. A typical image of modified DAW in the Y–Z plane $\approx$ 2 mm away from the rod is shown in Fig. 3.7(b). It is observed that the dust particles are lifted up a height of few mm from the previous equilibrium position (*i.e.*, in absence of the rod) adjacent to the floating rod as depicted in Fig. 3.7(b). It means that the dust particles are now levitated at a new equilibrium position in presence of the rod and DAWs are originating because of collective oscillatory motions of charged dust particles around their equilibrium position. In addition, the linear wavefronts of DAW become curved in nature and are found to propagate in the Y–Z plane. It is to be noted that the average wavelength and phase velocity of DAW are $\sim$ 2.5 mm and $\sim$ 3 cm/sec, respectively. It is worth mentioning that wavelength of DAWs increases, whereas the velocity decreases when the rod is brought nearer to the dust cloud. For further characterization of DAWs, the images are taken in the horizontal (X–Y) plane. In this plane, the circular wavefront of DAWs originates at the outer edge of the perturbed region and propagates in the inward direction (or towards the rod surface). A typical video image of DAWs just below the rod in the horizontal plane is shown in the Fig. 3.7(c). Hence, it is concluded from Fig. 3.7(b) and Fig. 3.7(c) that the floating rod modifies the propagation characteristics of DAWs, which are found to propagate obliquely (along the radial ($-\hat{r}$) and gravity ($-\hat{z}$)).

It is well known that the dust grains always follow the equipotential contours, where the electrostatic force acting on them is exactly balanced by the gravitation force. In the presence of a floating rod, the cathode sheath electric field gets modified [25] and dust grains now follow the modified equipotential contour to get an equilibrium position. Hence, the dust particles are lifted up by few mm adjacent to the rod in the perturbed region. In addition to that, the dynamics of the ions gets changed due to the change of sheath electric field. Initially (in absence of the rod), the direction of ion streaming is in $-\hat{z}$ direction whereas in presence of the rod, the ion flow direction become oblique; having velocity components along the radial direction ($-\hat{r}$) of cathode plane and gravity ($-\hat{z}$). As discussed in section 3.5 that the streaming ions are mainly responsible for exciting the dust acoustic waves in the present set of experiments; therefore, its propagation direction is changed to oblique according to the motion of ions.

3.6.2 Horizontally aligned floating rod

To get more insights of the wave-rod interaction, a set of experiments is performed with a horizontally aligned floating rod, which is kept always perpendicular to the Y–Z plane. To study the propagation characteristics of DAWs, the images are taken in the Y–Z plane for a particular location of X. A series of experiments are carried out to study the propagation characteristics of DAWs for various discharge voltages (V_d) at a fixed gas pressure (0.07 mbar). It is to be noted that the position of the floating rod is always kept just above the upper layer of dust cloud (near the cathode sheath edge) even though the dust cloud position changes with the change of discharge voltage. The change of propagation characteristics of DAWs are shown in Fig. 3.8(a-d) for different discharge voltages. In this range of discharge voltage,

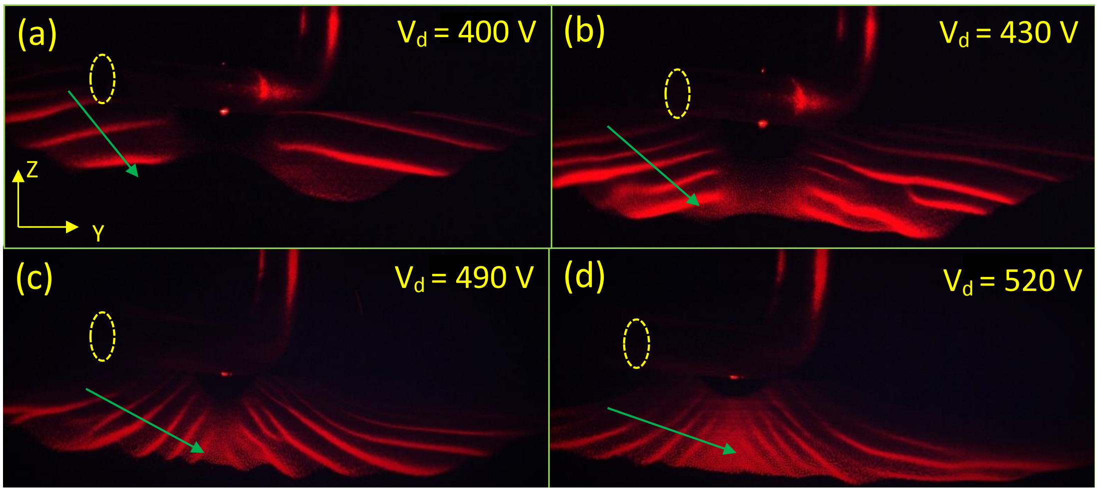

Figure 3.8: Video images of dust acoustic waves with floating rod in horizontal plane: (a) – (d) for discharge voltage (V_d) 400, 430, 490, and 520 V, respectively. The argon gas pressure is set at 0.07 mbar during the measurements. The yellow dotted circles represent the front of the floating rod. Green arrow indicates the direction of the propagating DAWs.

the average wavelength and phase velocity of DAWs also change from $\sim$ 2.6–1.7 mm and $\sim$ 3.3–4.2 cm/sec, respectively. It is clear from these figures that the DAWs propagate obliquely with two velocity components (along the Y and Z) in presence of the rod. The Z-component dominates over the Y-component at lower discharge voltage (at 400 V), whereas Y-component dominates over the Z-component at higher discharge voltage (at 520 V). An arrow in Fig. 3.8(a) to Fig. 3.8(d) indicates the propagation direction of DAWs, which is obtained by analyzing the consecutive frames for different discharge voltages. It is also observed that dust particles are lifted up by few mm near the rod and this effect becomes significant for higher discharge voltage (see Fig. 3.8(c) and Fig. 3.8(d)). Similar to the earlier case (with vertical aligned rod), a dust free region always present near the rod. The size of the dust-free region reduces with the increase of the discharge voltage. It is also found that the dust particles just below the rod always show random motion at a discharge voltage of 380–420 V.

In the case of horizontally oriented floating rod, sheath around it interacts with cathode sheath. It is expected that modified (resultant) sheath electric field changes with the change of discharge parameters. At lower discharge voltage (400 V), a thick sheath region (strong E-field) around the rod repels the dust grains and a dust free region is formed (Fig. 3.8(a)). With the increase of discharge voltage (at

520 V), the sheath thickness around the rod decreases significantly and as a result, the void size reduces (see Fig. 3.8(d)). The size of the dust-free region depends on the magnitude of the electrostatic and ion drag force acting on the dust grains. The size of dust void reduces with increase in the ion-drag force compared to the electrostatic force. Increase of discharge voltage (from 400 V to 520 V) causes a considerable change in the sheath electric field, which results in a significant change in the ion dynamics. It is observed that at lower discharge voltage, the velocity component of ions along Y-direction becomes smaller compared to that at higher discharge voltage. As a result, the DAW propagates almost in the vertical direction (along the gravity) at lower discharges voltage, whereas obliquely at higher discharge voltages. This effect is clearly seen in Fig. 3.8.

The wave characteristics in absence and presence of a floating rod at pressure p = 0.07 mbar for various discharge voltages and orientations are summarized in Table 3.1. The tabulated values show that the wavelength of DAWs decreases, whereas the phase velocity and the frequency increase with the increase of the discharge voltages in all the cases. In the presence of floating rod (vertical/horizontal), the wavelength of DAWs increases and phase velocity decreases than that observed in absence of the rod at same plasma parameters.

Table 3.1: Dust acoustic wave characteristics without and with the rod orientations for fixed pressure p = 0.07 mbar and varying discharge voltages.

Rod location/orientation	Bias voltage (V_d) in V	Wavelength (λ) in mm	Phase velocity (v_{ph}) in cm/sec	Frequency ($f = v_{ph}/\lambda$) in Hz
(a) In absence of the rod	370	2.5 ± 0.4	2.5 ± 0.4	10 ± 1.6
	470	2.0 ± 0.4	4.0 ± 0.8	20 ± 5
(b) Vertical orientation				
Z $\sim$ 3.7 cm	450	2.6 ± 0.4	3.0 ± 0.5	11 ± 1.8
Z $\sim$ 3.3 cm	470	2.5 ± 0.5	3.2 ± 0.6	12 ± 3
(c) Horizontal orientation				
Z $\sim$ 4.0 cm	400	2.5 ± 0.5	3.3 ± 0.6	13 ± 3.5
Z $\sim$ 3.7 cm	430	2.1 ± 0.4	3.6 ± 0.7	17 ± 4.4
Z $\sim$ 3.3 cm	490	1.9 ± 0.3	4.1 ± 0.6	21 ± 4.2
Z $\sim$ 3.0 cm	520	1.7 ± 0.3	4.3 ± 0.7	25 ± 5

Finally, we have further examined the propagation characteristics of DAWs by keeping the floating rod at various Z-locations (measured from cathode surface) for a given discharge condition, V_d = 410 V and p = 0.07 mbar. Fig. 3.9(a-d) shows the propagation characteristics of DAWs in presence of rod at Z $\sim$ 32, 25, 17 and 10 mm, respectively. It is to be noted that Z $\sim$ 32 mm corresponds to the location just below the topmost dust layer. As the floating rod is moved from Z $\sim$ 32 to 25 mm, the rod reaches almost to the middle of the dust cloud and modifies the propagation characteristics of DAWs, which is shown in Fig 3.9(b).

It is seen in Fig. 3.9(b), a dust free region of length $\approx$ 2 mm is formed around

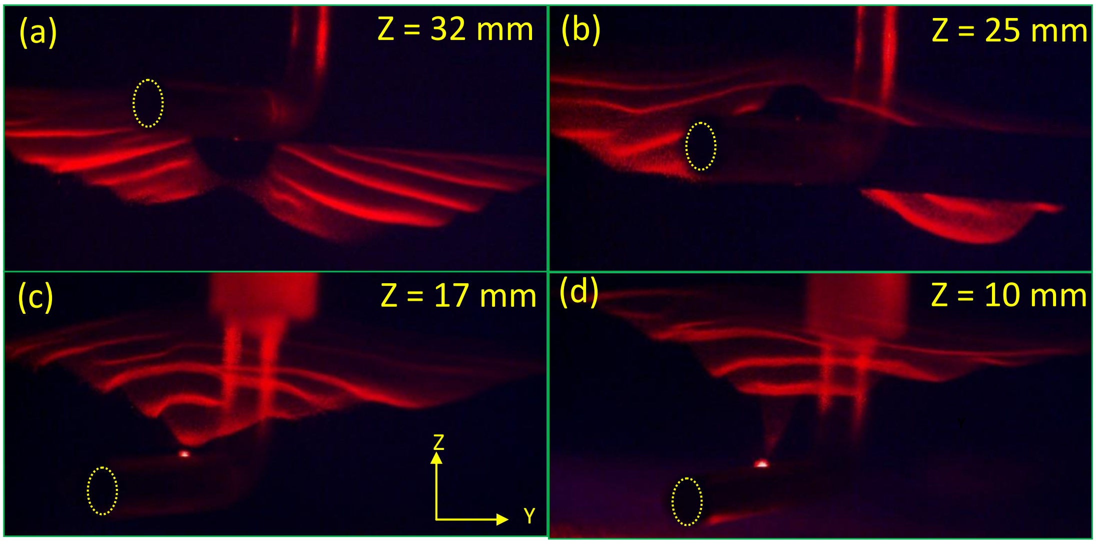

Figure 3.9: Video images of DAWs with floating rod at various locations in the sheath region: (a) rod is near the edge of sheath. (b) inside the sheath region where dust particles are levitated. (c) below the lower edge of levitated dust cloud. (d) near the cathode surface. The yellow dotted circles represent the front of rod in X-Y plane. The position of floating rod is measured with respect to the cathode surface. The error in measured value of rod position is $\mp$ 3 mm. Discharge voltage and pressure are set at 410 V and 0.07 mbar for these set of experiments.

the cylindrical rod; whereas in the outside of the void region, DAW fronts become concave in nature. It is observed that at Z $\sim$ 17 mm, the dust cloud takes cone-like structure above the floating rod and DAWs propagate obliquely as discussed in earlier section. In the case of Fig 3.9(d), the floating rod is moved deeper to the cathode sheath (Z $\sim$ 10 mm) where the electric field is most strong compared to three previous locations. In the absence of rod, dust particles normally are not found at $\sim$ 10 mm; whereas, in presence of the rod particles are found to exhibit the oscillatory motion. Interestingly at this location, the dust particles follow the floating rod inside the sheath in the form of a cone-like structure, which is shown in Fig. 3.9(d).

The observed results with floating rod at different locations provide a strong evidence of sheath E-field modification around the floating rod while it interacts with the dust cloud. In Fig. 3.9(b) (when the rod is kept at the edge of cathode sheath), the variation of E-field around the rod is similar to that is reported by Barnat *et al.* [25]. The strong E- field near the rod pushes the dust grains against ion drag force and as a result dust void is formed. Outside the void region, weak E-field gives rise to the curved shape dust cloud along with the DAWs. In Fig. 3.9(c) and 3.9(d), the cone-shaped profile of unstable dust cloud is the result of modified E-field above the rod [25]. The electric field gets weaker around the floating rod when it is placed inside the sheath region. This lower electric field provides an equilibrium to the dust particles above the rod; therefore, the dust acoustic waves are found to propagate towards the rod surface inside the confined dust cloud.

3.7 Summary and conclusions

In this Chapter, we have reported the experimental observations of self-excited dust acoustic waves and its propagation characteristics in the absence and presence of a floating cylindrical object. The DC glow discharge dusty plasma is produced in a glass chamber in the background of argon gas. Plasma and dusty plasma parameters are measured/estimated in a wide range of discharge conditions. In our experiments, the cathode sheath E-field serves two purposes. Firstly, it provides an electrostatic force that balances the dust particles against gravity. Secondly, the electric field drives the strong downward ion flow results in the excitation the DAWs in the dust cloud. A thoroughly investigation on the propagation of dust acoustic waves is carried out with and without a floating rod. The main findings of our experimental observations are summarized as follows:

1. The dust acoustic waves are excited spontaneously in an equilibrium dust cloud above a threshold discharge current and below a critical background neutral gas pressure. The low-frequency waves are found to propagate along the direction of flow of ions (towards cathode). A detailed characterisation of DAWs is made by measuring the velocity and the wavelength.

2. The propagation characteristics of self-excited DAWs are modified during the interaction of a floating cylindrical object either kept vertically or horizontally. The modification of DAWs in presence of the rod is extended up to $> 100\lambda_D$ from the surface of the object.

3. In presence of a floating rod (aligned vertically), the DAWs disappear in the perturbed region at lower discharge voltage ($V_d \sim 380 - 400$ V) whereas; at higher discharge voltage (above $V_d \sim 420$ V), the DAW are found to propagate obliquely. The obliqueness of DAWs changes with the change of discharge parameters.

4. In the case of the horizontally aligned rod, the DAWs gets excited in a cone shaped dust cloud in the cathode sheath region. Displacement of dust grains in downward (upward) direction confirms that the cathode sheath electric field becomes weaker (stronger) in presence of the floating objects.

The excitation of dust acoustic waves and the modification of its propagation characteristics in presence of a floating object is explained in terms of streaming ions inside the dust cloud. In absence of the rod, the streaming ions towards the cathode exert a pressure on the levitated dust grains and turn the dust medium into an unstable state, resulting in the excitation of DAWs which are found to propagate in the direction of streaming ions or gravity. In presence of the rod (kept either vertically or horizontally), the sheath around it alters the potential profile of cathode sheath. It happens due to the coupling between the sheaths formed around the cylindrical rod and the cathode. In this coupling, the spatial distribution of potential or electric field gets modified in the perturbed region. In the perturbed region, dust grains follow the modified equipotential surfaces to get an equilibrium position; therefore, they are lifted up near the rod. The direction of streaming ions changes according to modified (resultant) sheath electric field and as a result, the DAWs are found to propagate obliquely.

Study of the dusty plasma at lower pressure (<0.05 mbar) in DC discharge configuration is found to be more problematic. At low pressure, dusty plasma is highly unstable and poorly confined due to the high voltage cathode spots. The volume of the dusty plasma at low pressure does not remain constant for longer time due to the poor radial confinement. For the formation of an equilibrium 3D dusty plasma at low pressure, a new configuration needs to be explored. Next chapter provides the detailed descriptions of the novel configuration for producing the dusty plasma at low pressure.

4

Transport and Trapping of Dust Particles in Diffused Plasma

In this chapter, a novel configuration using inductively coupled discharge to study the dynamical behavior of large volume dusty plasma is discussed. In this configuration, dust particles are confined in an electrostatic potential well which is created by inductively coupled diffused plasma. For injecting dust particles into plasma volume, a unique technique using DC glow discharge is employed. The volume of the dusty plasma can be controlled by tuning the plasma and discharge parameters. The detailed description of the particles transport, confinement of particles in the potential well and characteristics of the dusty plasma are presented.

4.1 Introduction

It has been discussed in Chapter 1, the dusty plasmas can be used as a platform to understand the underlying physics at microscopic level for various multidisciplinary fields such as physics of fluid flows, crystalline properties of solids, waves and instabilities in complex fluids, phase transitions of solids etc. The study of the collective phenomena (e.g. waves and vortices) in the dusty plasma helps to understand the various structures observed in astrophysical plasma [43, 51, 198]. However, to study the collective dynamics of dusty plasma, the dust grain medium of dimension larger than the characteristic size of collective modes is required. In the last couple of decades, various configurations have been used to create the electrostatic trap which enables to confine the dust grains for longer time against gravity.

In some of the experimental dusty plasma devices [1, 2, 18, 187] which are operated in DC discharge mode, the dust particles are trapped into the anodic plasma which sits nearly 50–60 volts above the plasma potential. The dust particles are introduced in the anodic electrostatic trap either using a floating tray or by a dust dispenser. The trapped dust particles exhibit 3D dust structure along with associated waves and instabilities. However, these configurations provide the confinement of dust grains but unable to maintain a steady state equilibrium below a critical pressure ($p < 0.08$ mbar). At higher pressure ($p > 0.1$ mbar), even though the equilibrium dusty plasma is possible but its volume is not too large [199]. Apart from this anode trap, standing strata also provides an electrostatic trap to confine the dust particles in which one can explore the waves and crystallization properties of dust medium [200–202]. In strata, the dust grains are confined at lower edge and forms a dust cloud of 5–20 mm in diameter at a higher pressure (p $>$ 0.1 mbar). Furthermore; in the DC glow discharges, cathode sheath electric field provides a force to hold the dust grains against gravity. In the cathode trap, an equilibrium dusty plasma volume is only possible when the pressure is more than 0.1 mbar otherwise spontaneous dust acoustic modes will be triggered [5, 110]. A dusty device, PK-4 [203], working with DC discharge configuration is being used to study the waves, instabilities and order structures in dusty plasmas at ground level as well as at microgravity level.

It has been observed in many experiments that an equilibrium dusty plasma can be formed in rf discharges even at low pressure ($<$ 0.02 mbar). In rf (capacitive coupled) discharges, dust particles are confined at the sheath edge of the powered electrode with an additional confinement ring installed at a lower electrode. Since, sheath electric field decreases monotonically from the electrode surface to the plasma which allows dust grains to form a 2D dust layer (in the case of mono dispersive particles) above the rf electrode [19, 77, 204]. However, 3D dust structure with less extent (nearly 10 mm) is formed above the rf electrode which still suits to perform the wave experiments [3, 205]. Moreover, the large volume dusty plasma is possible at microgravity level using the rf configuration but the ion drag repels dust grains from the center region, resulting in dust cavity forms [206]. In another rf discharge configuration, diffused edge of inductively coupled plasma has been used to confine the dust particles at low-pressure [20, 114]. In this configuration, an equilibrium small 3D dusty plasma can be created at lower pressure.

The previous studies conclude that self–excited collective modes and instabilities, driven linear and nonlinear collective modes, transient response of an equilibrium dusty plasma etc. are still unexplored problems in a large volume low-pressure dusty plasma. Along with the stable confinement, it is also necessary to control the dust density during the experiments. For producing an appropriate dusty plasma, a novel configuration using the inductively coupled discharge at low pressure has been investigated. Also, a unique technique using the DC glow discharge has been explored to introduce the dust grains into the potential well. This Chapter is organized as follows: Details of experimental device and techniques are presented in Sec. 4.2. Sec. 4.3 describes the characteristics of the diffused plasma. The physics of dust transport and trapping are discussed in Sec. 4.4. A brief summary of the work along with a concluding remark is provided in Sec. 4.5

4.2 Experimental device and techniques

For producing the dusty plasma at low pressure, the dusty plasma device shown in Fig. 4.1(a) is used. The detailed description of the experimental device has been given in section 2.2. The dusty device is made of the experimental chamber and buffer chamber. The rotary pump and gas inlet are attached to the buffer chamber. This assembly prevents directed gas flow induced neutral drag on the dust particles during the experiments. A schematic of the experimental device is shown in Fig. 4.1(b). In this experimental configuration, Z = 0 cm and Z = 60 cm correspond to the left and right axial ports, respectively. X = 0 cm and Y = 0 cm indicate the points on the axis passes through the center of the tube. The center of source tube is located at Z$\sim$ 12 cm, whereas the dust reservoir is located at Z $\sim$ 45 cm. A stainless steel disk of 6 cm diameter is used as a dust reservoir and mounted at one of the radial ports (Z $\sim$ 45 cm) of the chamber by a cylindrical rod. Before closing the chamber, the dust particles are sprinkled on the disk homogeneously. The experimental chamber is evacuated at $\sim 10^{-3}$ mbar pressure using a rotary pump and subsequently, the argon gas is fed into the chamber. Then the chamber is pumped down again to the base pressure. This process is repeated three to four times to reduce the impurities from the vacuum chamber. Finally, the operating pressure is set to 0.03 – 0.1 mbar by adjusting the gas dosing valve.

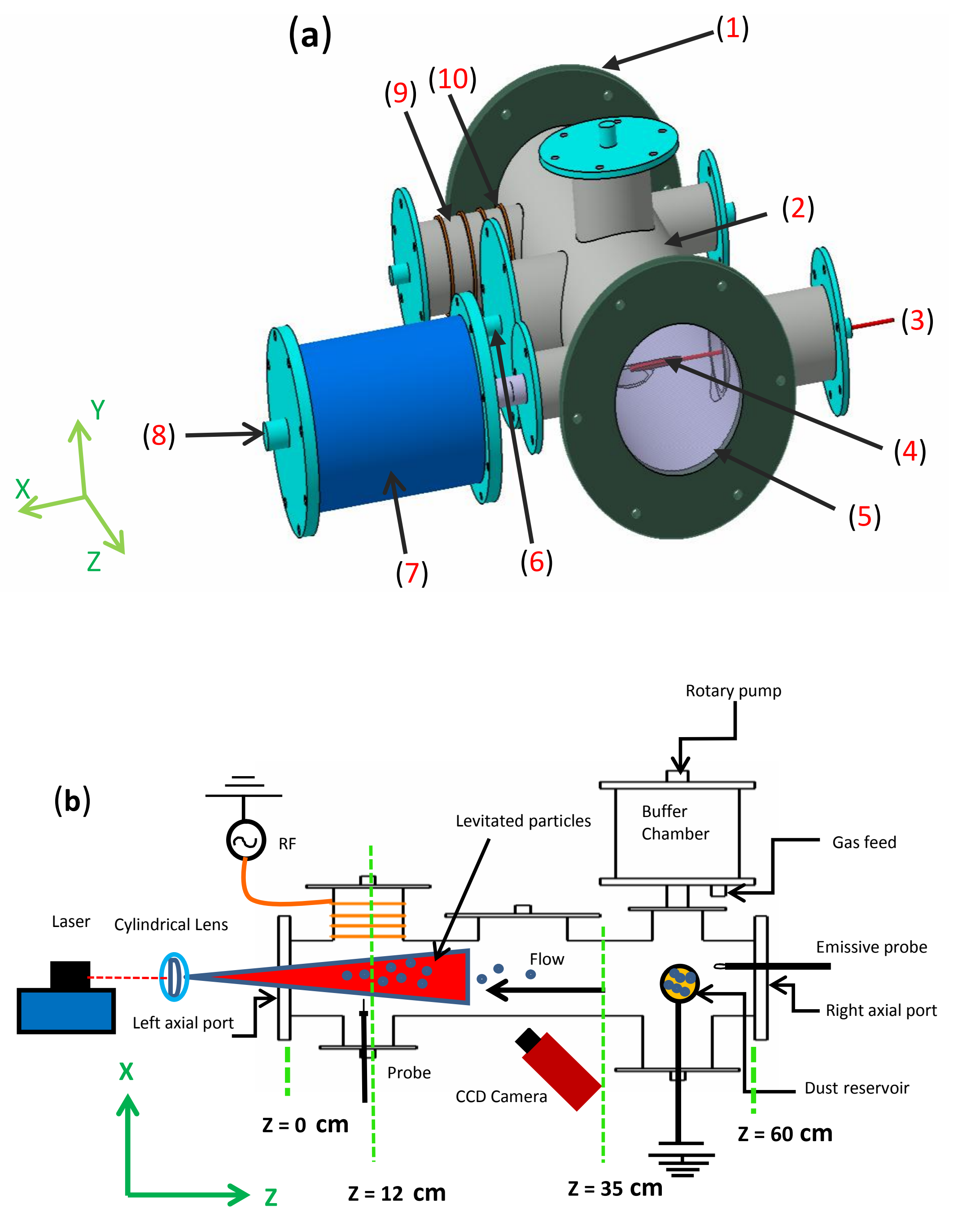

Figure 4.1: (a) 3D view of experimental setup: (1) Left axial port, (2) experimental chamber, (3) SS rod for holding the dust containing disk, (4) dust containing disk (dust reservoir), (5) right axial port, (6) gas feeding valve (attached to buffer chamber), (7) buffer chamber, (8) rotary pump, (9) ICP plasma source tube and (10) inductive coil. (b) Schematic diagram of inductively coupled dusty plasma device (Top view).

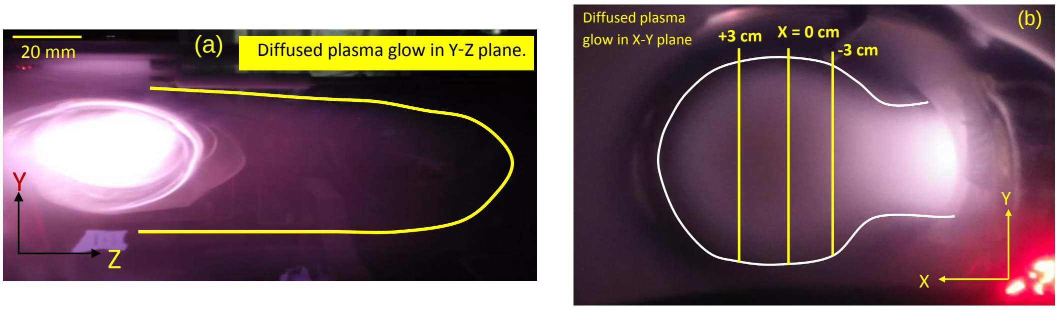

Figure 4.2: (a) A typical plasma glow in the Y–Z plane. The yellow line represents the boundary of glow region. (b) The plasma glow profile in the X–Y plane. The white line indicates the boundary of glow region in this plane. Vertical yellow lines represent the different vertical positions for given a X–value. Argon pressure and input rf power are 0.05 mbar and 10 W, respectively.

An inductive coil made of copper wire (5 turns) is wound on the source tube (P1), which is connected to the experimental chamber as shown in Fig. 4.1. An inductively coupled radio frequency (of 13.56 MHz) discharge is initiated inside the source tube by coupling of input rf power. The plasma production through an inductively coupled power has been discussed in subsection 2.3.2. The plasma is formed in the source section and diffuses in the main experimental chamber. The typical views of diffused plasma glow in the Y–Z and X–Y planes are shown in Fig. 4.2(a) and Fig. 4.2(b), respectively. This glow boundary changes with the change of discharge parameters. This diffused plasma forms an electrostatic trap for negatively charged dust grains, which will be discussed in subsequent sections. For injecting the kaolin dust particles (2.6 gm/cm^3 and $r_d \sim 0.5$ to 5 μm) into this electrostatic trap, the dust-containing disk (dust reservoir) is negatively biased (about -300 V or above) to form a DC glow discharge (secondary plasma) around the disk. In this plasma background, dust particles get negatively charged and are lifted up and found to trap at the cathode sheath edge. However, due to poor confinement and high voltage cathode spots, trapped dust particles leave this region and spread into the bulk plasma. As these charged particles reach the edge of diffused plasma, they start to drift and confine in the electrostatic potential well. The mechanism of dust transport and trapping in the diffused plasma are discussed in more details in subsequent sections.

These dust particles are illuminated by the combination of a tunable red diode Laser and a cylindrical lens. The dynamics of the dust particles are captured by a Lumenera make CMOS camera having the frame rate of 130 fps and spatial resolution of 1088 $\times$ 2048 pixels. A standard zoom lens of variable focal length (from 18 mm to 108 mm) is used for the magnification purpose during the experiments. The maximum field of view at minimum zoom mode is $\sim$150 mm $\times$ 75 mm and it reduces to $\sim$25 mm $\times$ 12.5 mm at maximum zoom mode. There is a provision to image the dust cloud in all the planes of the experimental chamber (X–Y, Y–Z, and X–Z) by changing the orientation of the cylindrical lens and camera. The series of images are then stored in a high–speed computer and later analyzed with the help of ImageJ software and MATLAB based PIV software.

4.3 Characterization of diffused plasma

To understand the dust particles transport and trapping in an inductively coupled diffused plasma in more details, it is necessary to characterize the diffused plasma. The electrostatic probes namely, single Langmuir probe, double probe, and emissive probe are used to characterize the diffused plasma at a wide range of discharge parameters. The construction and working principle of the electrostatic probes have been discussed in section 2.4.

4.3.1 Plasma density and electron temperature variation

Fig. 4.3 shows the variation of plasma density (n) and electron temperature (T_e) along the axes (X, Y, and Z axis) of the experimental chamber at an rf input power, P = 10 W and argon pressure, p = 0.05 mbar. Fig. 4.3(a) shows the variation of plasma density and electron temperature in the direction of the experimental chamber (along the Z–axis) at Y $\approx$ 0 cm and X $\approx$ 0 cm. Plasma density initially increases from $\sim 4{\times}10^8 cm^{-3}$ (at Z $\sim$ 1 cm), reach to a maximum value of $\sim 7{\times}10^8 cm^{-3}$ (at Z $\sim$ 12 cm) and then falls monotonically to $\sim$1 $\times 10^8 cm^{-3}$ (at Z $\sim$ 30 cm). An axial electron temperature profile shows similar trend as much as like the plasma density. The electron temperature in Z-direction changes from a maximum value of $\sim$ 8 eV to a minimum value of $\sim$ 3 eV. The variation of n and T_e in vertical direction (along the Y–axis) at X $\approx$ 0 cm and Z $\sim$ 12 cm is shown in Fig. 4.3(b). Both n and T_e decrease from these peak values (at Y$\approx$ 0 cm) toward the wall of the experimental chamber. The variation of plasma density and electron temperature along the axis of source tube (along the X–axis) at Z$\sim$ 12 cm and

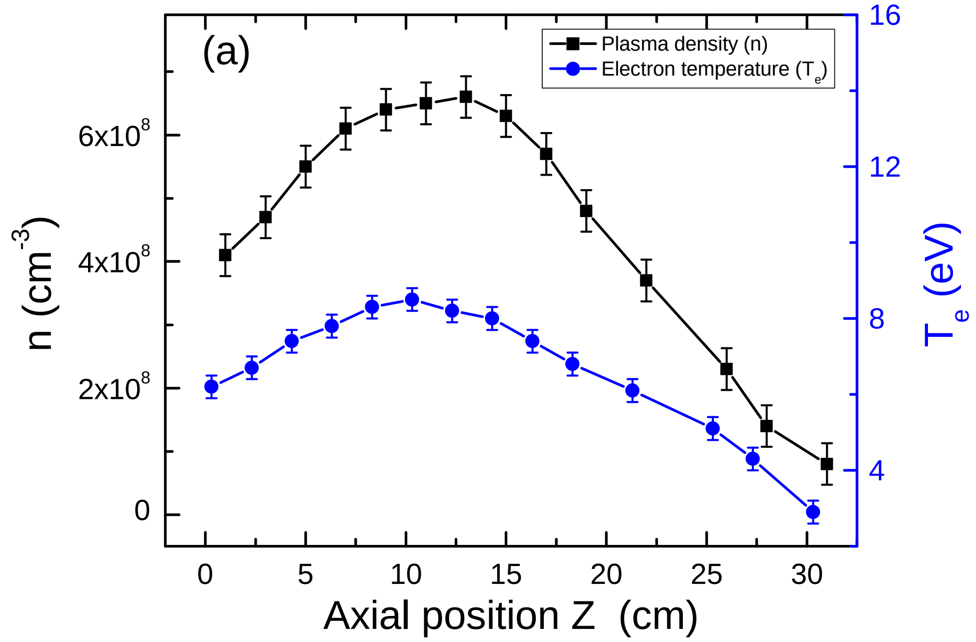
(a)
Plasma density (n)
Electron temperature (T_e)
n (cm^-3)
6x10^8
4x10^8
2x10^8
0
T_e (eV)
16
12
8
4
0
5
10
15
20
25
30
Axial position Z (cm)

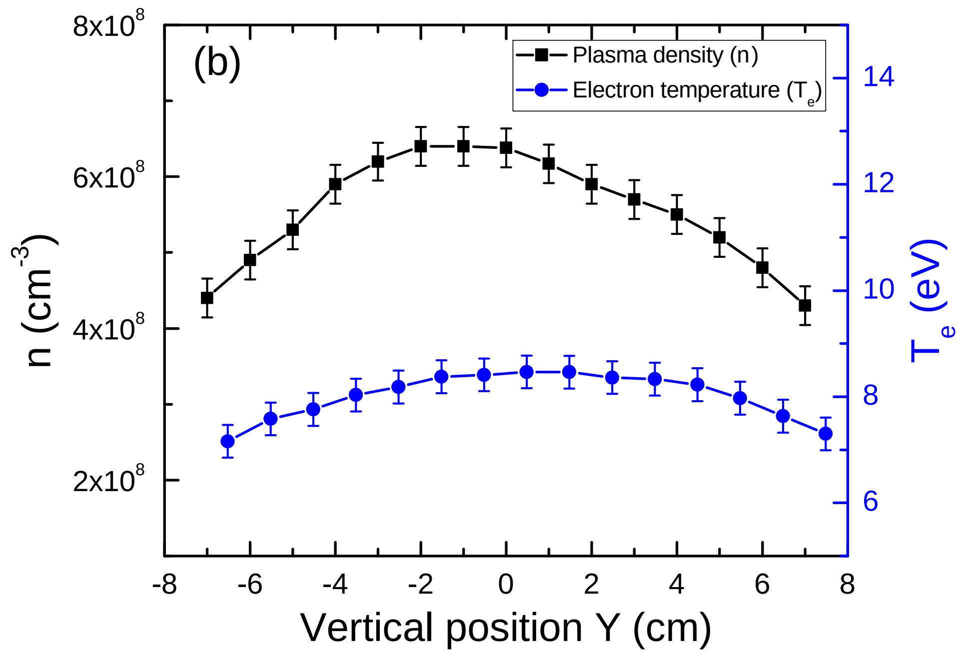
(b)
Plasma density (n)
Electron temperature (T_e)
n (cm^-3)
8x10^8
6x10^8
4x10^8
2x10^8
T_e (eV)
14
12
10
8
6
-8
-6
-4
-2
0
2
4
6
8
Vertical position Y (cm)

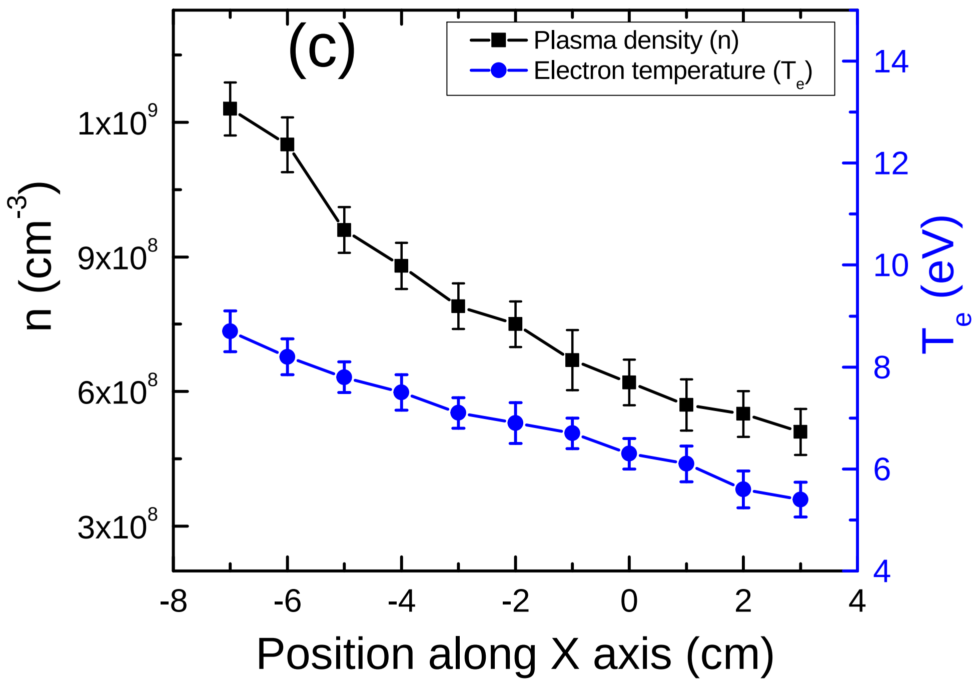

Figure 4.3: Plasma density (n) and electron temperature (T_e) profiles: (a) along the Z–axis of the experimental chamber (at X≈ 0 cm and Y≈ 0 cm). (b) along the Y–axis (at X ≈ 0 cm and Z ∼ 12 cm). (c) along the X–axis (at Y ≈ -2 cm and Z ∼ 12 cm. Argon pressure and rf power are 0.05 mbar and 10 W, respectively. The errors in the measured values of n and T_e are within ± $3{\times}10^7 cm^{-3}$ and ± 0.3 eV, respectively.

Y≈ -2 cm is depicted in Fig. 4.3(c). The plasma density is higher ($\sim 1{\times}10^9 cm^{-3}$) near the mouth of source tube (at X = -7 cm) and decreases monotonically ($\sim 5{\times}10^8 cm^{-3}$) towards the chamber wall (X = 3 cm). Similar trend is observed for T_e with the changes in T_e from ∼ 9 eV to 5 eV. All these figures essentially indicate that n and T_e decrease monotonically along the direction of diffused plasma.

4.3.2 Plasma potential variation

The plasma potential along the axes (X, Y and Z axis) is measured using an emissive probe in a wide range of discharge parameters to study the dust grain dynamics. The simplest method, i.e., floating potential method is followed to measure the plasma potential. Use of an emissive probe to measure the plasma potential is discussed in section 2.4. Fig. 4.4 displays the variation of plasma

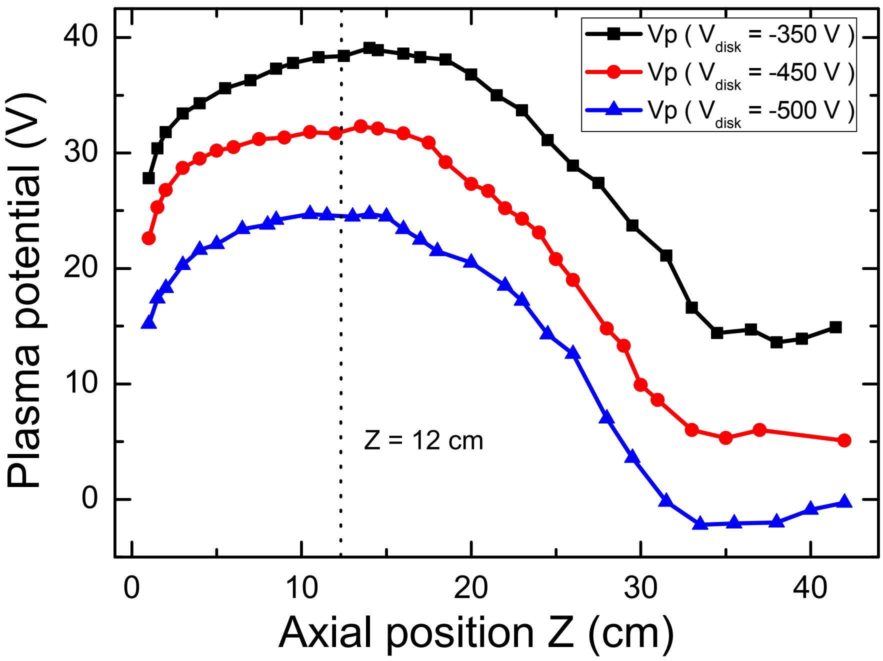

Figure 4.4: Plasma potential profiles along the axis of experimental chamber at X ≈ 0 cm and Y ≈ -3 cm for different disk bias voltages. The measurements are taken in the absence of dust grains at an argon pressure of 0.05 mbar and rf power of 10 W. The dotted line represents the central region where dust particles get confined during the transport. The measurement errors are within ± 5%.

potential along the axis of the experimental chamber for a given location, X≈ 0 cm and Y ≈ -3 cm, at different disk bias voltages. For these measurements, the background neutral gas pressure (p = 0.05 mbar) and input rf power (P = 10 W) are kept constant. It is clearly seen in Fig. 4.4 that the measured plasma potential decreases on both sides if one goes away from the potential well localized at Z ∼ 12 cm. The change in plasma potential becomes insignificant beyond Z ∼ 30 cm. This measurement implies that the gradient in plasma density and electron temperature along axial direction (see Fig. 4.3) creates a potential well centering at Z ∼ 12 cm. It is also to be noted that the depth of the potential well remains almost constant, whereas the magnitude of the plasma potential decreases with the increase of the applied bias voltage to the disk.

Fig. 4.5(a) shows the plasma potential variation along the Z–axis (similar to Fig. 4.4) for two different neutral gas pressures, p = 0.05 mbar (indicated by squares) and 0.025 mbar (indicated by closed circles) at an rf power of 10 W, whereas Fig. 4.5(b) shows the same for two different rf powers, P = 10 and 13 W at a particular pressure, p = 0.025 mbar. In the both cases, the DC plasma is

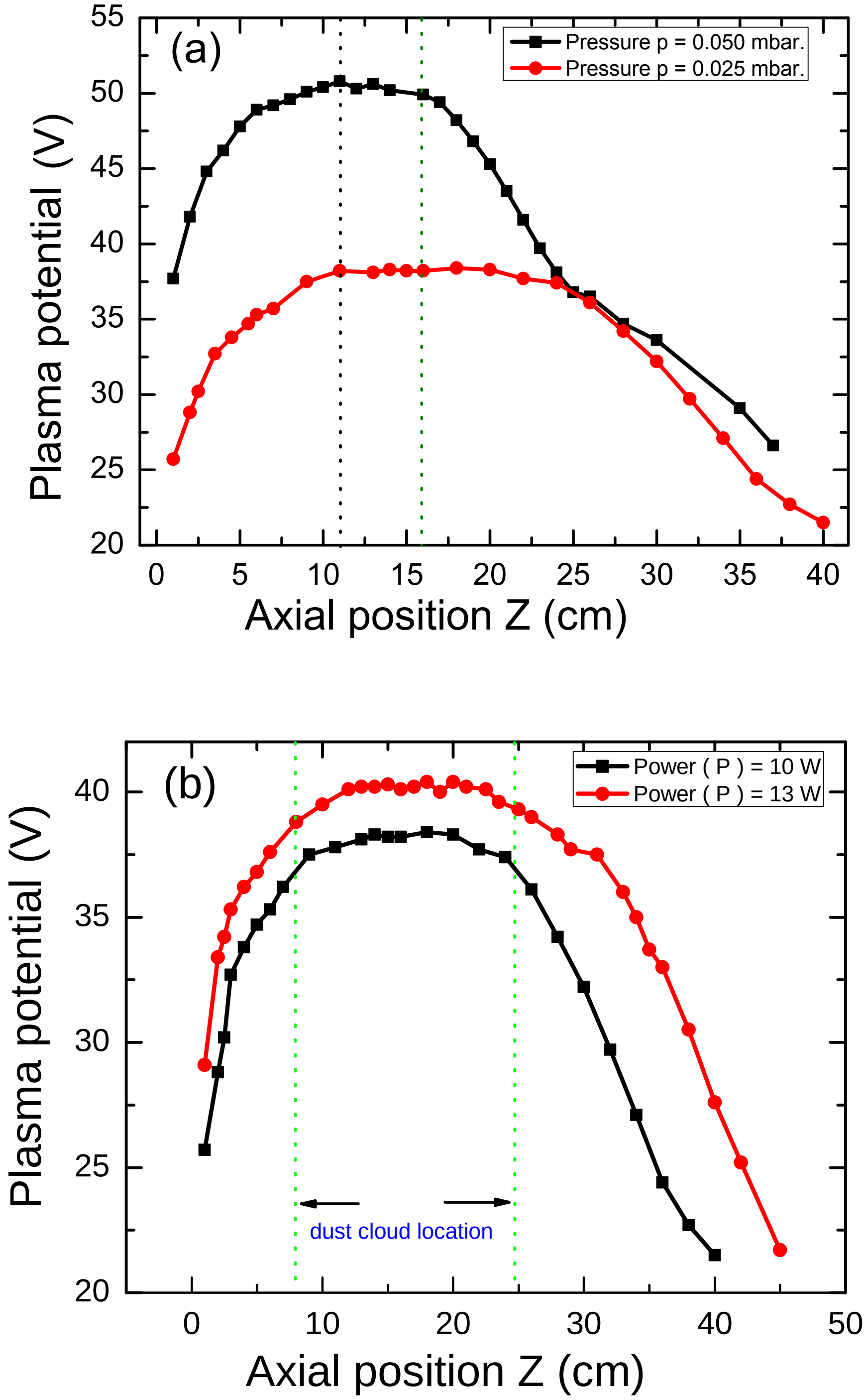

Figure 4.5: Axial plasma potential profiles of the diffused plasma for (a) two different gas pressures p = 0.05 and 0.025 mbar at a fixed rf power P = 10 W and (b) two different rf powers P = 10 and 13 W at a fixed gas pressures, p = 0.025 mbar. The measurements are taken after switching off the DC plasma. The black and green dotted lines (in Fig. 4.5(a)) represent the center of the potential well at 0.05 and 0.025 mbar, respectively. The errors in the measured value of plasma potential are within ± 5%.

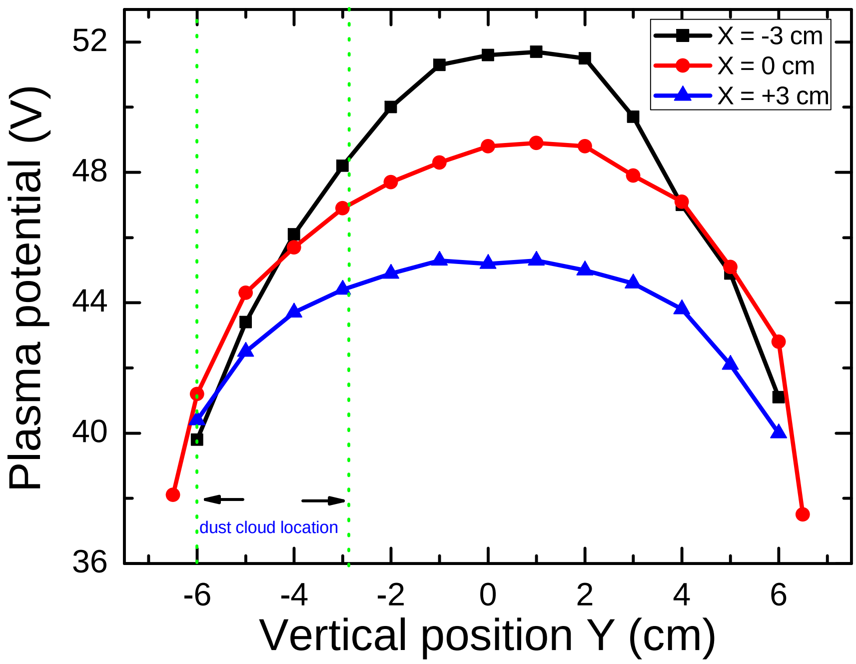

Figure 4.6: Plasma potential variation along the direction of gravity (along Y– direction) for different X locations at Z $\sim$ 12 cm. The experiments are performed in argon gas at pressure, p = 0.05 mbar and rf power, P = 10 W. The dust cloud lies between the dotted lines. The errors in the measured plasma potential are within $\pm$ 5%.

kept switched off ,i.e., no bias on the disk. It is noticed from Fig. 4.5 that depth of the potential well increases, whereas the width decreases significantly with the increase of the gas pressure. Interestingly, the center of the potential well also shifted from left (Z $\sim$ 11 cm) to right (Z $\sim$ 16 cm) when the pressure is decreased from 0.05 mbar to 0.025 mbar. However, the depth and the width of the potential well increase when the rf input power is increased from 10 W to 13 W keeping the center at the same location.

The plasma potential profiles along the direction of gravity (along the Y– direction) for different X locations are shown in Fig. 4.6. The different X locations are X = -3, 0, and 3 cm for a given Z $\sim$ 12 cm. The plasma potential is measured for the discharge parameters, P = 10 W and p = 0.05 mbar. It is clearly seen in Fig. 4.6 that the plasma potential follows a nearly symmetric trend in the vertical direction from the center (Y = 0 cm) for a given X location. The plasma potential decreases gradually in the direction of gravity (along and opposite) away from the center. It is also worth mentioning that the plasma potential decreases from X

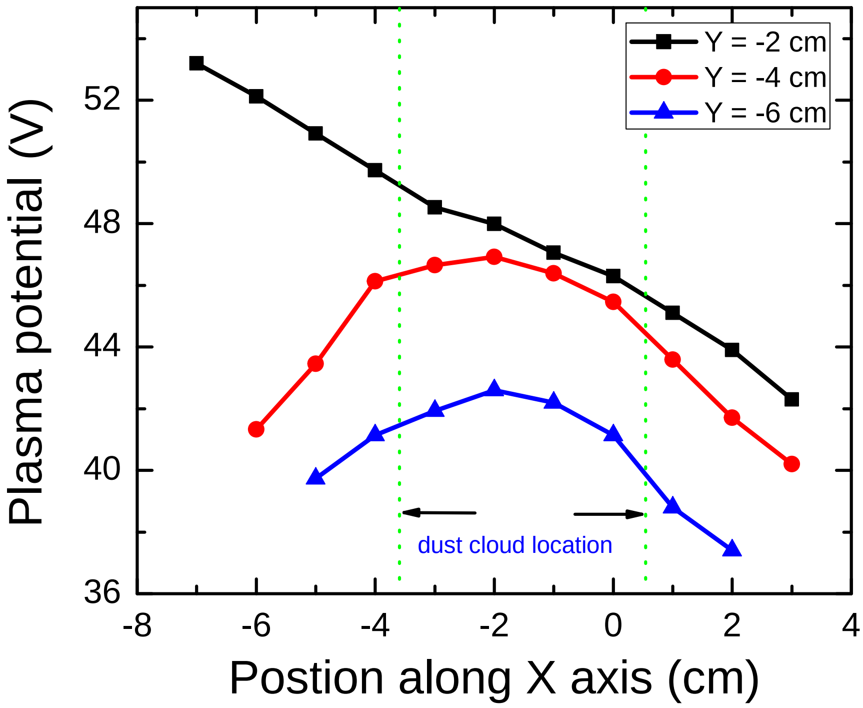

Figure 4.7: Plasma potential variation along the axis of source tube (along X–direction) for different Y locations (Y = -2 cm, -4 cm, and -6 cm) at Z $\sim$ 12 cm. The experiments are performed in argon gas at pressure, p = 0.05 mbar and rf power, P = 10 W. The dust cloud lies between the dotted lines. The measurement errors are within $\pm$ 5%.

= - 3 (close to the plasma source) to X = +3 cm (away from the source) for the given Z and Y values due to the gradient in plasma density and electron temperature along the X axis (Fig. 4.3(c)). The variation in plasma potential along the Y–direction for different X locations confirms the finite potential gradient in the diffused plasma along the gravity. The variation of plasma potential along the X–axis for different Y locations (Y = -2 cm, -4 cm and -6 cm) at Z $\sim$ 12 cm is shown in Fig. 4.7. For Y = - 2 cm, plasma potential monotonically decreases along the length of diffused plasma (from X = -7 cm to X = 3 cm). On the other hand, there is a potential well centering at X $\sim$ -2 cm for other two Y locations, Y = -4 cm and -6 cm. The plasma potential measurements along the diffused plasma in all the directions (along the X, Y and Z axis) essentially confirms the formation of an electrostatic potential well, which can confine the negatively charged dust grains.

4.4 Dust grain transport and trapping

In this experimental configuration, a unique technique is followed to introduce the dust particles in an electrostatic trap. The dust reservoir is negatively biased (about -300 V or above) to produce a secondary DC glow discharge plasma. The dust grains get negatively charged in this DC plasma background by acquiring more electrons than ions. These negatively charged dust particles then levitate near the sheath boundary by balancing the electrostatic force and the gravitational force. Because of the poor radial confinement and high voltage cathode spots, these particles come into the plasma volume. When the particles fall down at the edge of potential well (at Z $\sim$ 30 cm) as shown in Fig. 4.4, they start to flow towards the center of potential well as discussed in Sec. 4.3. Finally, these transported particles get confined at a particular axial location where the confinement is strong. The axial confining potential well in absence of the DC glow discharge is shown in Fig. 4.5 for two different pressures and rf powers. After the confinement of particles in an electrostatic trap, the DC glow discharge is switched off to provide even a better confinement to the particles. It is because the dust particles are continuously transported toward the central region while DC plasma is on.

The velocity of the flowing particles is estimated by using Particle Image Velocimetry (PIV) analysis [21]. For performing the PIV analysis on still images, MATLAB based open access software openPIV [178] is used. In this technique, the velocity profile of flowing particles can be constructed by performing cross–correlation between two consecutive frames. The images with illuminated dust grains are decomposed into a similar interrogation boxes with the dimension of 64 $\times$ 32 pixels. After that, a cross–correlation of two images of a single interrogation box is used to construct the velocity vector for dust particles lying in an interrogation box. The distance traveled by a particle in the two consecutive frames is known; therefore, the velocity of flowing dust particles can be computed. For the measurement of drift velocity of the particles, few consecutive frames of flowing dust particles are considered. Fig. 4.8(a) shows a typical image of PIV analysis, where arrows indicate the direction of the particles flow whereas the length of an arrow represents the magnitude of the grain velocity. It is clear from Fig. 4.8(a) that particles are drifting towards the center of the potential well not horizontally rather obliquely. Although, the vertical component of the velocity is negligible compared to the horizontal component. Fig. 4.8(b) shows quantitative variation of these velocity components, v_z and v_y, along the Z and Y–axis. It is noticed in this figure that the velocity (average value is $\sim$ 0.23 cm/sec) in the Y-direction remains almost constant, whereas the velocity varies from 1.6 cm/sec to 1.0 cm/sec along the axis of the experimental chamber. The possible explanation is provided at the end of this section.

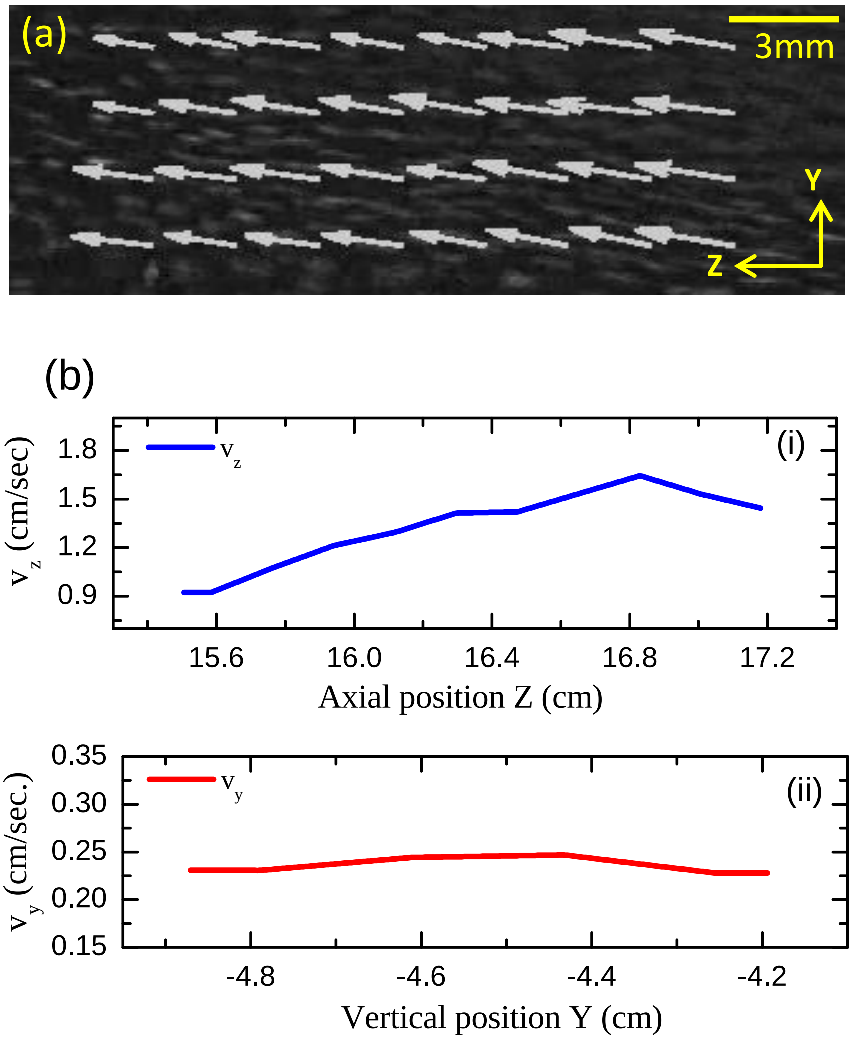

Figure 4.8: (a) PIV analysis shows the flow of particles toward the central region (Z $\sim$ 12 cm) when the dust reservoir is biased to -450 V. The direction of arrows indicates the dust particles flow, whereas length corresponds to the magnitude of the velocity vector. The white spots in the image correspond to the flowing kaolin particles. (b) The particle velocity profiles in two directions (Z and Y–directions). During the flow argon pressure and input power are 0.05 mbar and 10 W, respectively.

When we switch off the applied DC voltage to the dust reservoir, transport of the dust particles stop and they get confined in a region where they satisfy the force balance conditions. As a result, an equilibrium large 3D dust cloud is formed. It is observed that the dust cloud expands at lower pressure and its center shifts towards the re the reservoir if the other parameters are kept constant. The dust cloud expansion and its center shifting can be understood on the basis of broadening of the potential well at lower pressure (see Fig. 4.5(a)). It is also observed that the expanded dust cloud can be achieved with increasing the input power at given pressure, which is directly related to the broadening of potential well (see Fig. 4.5(b)). Hence, it is concluded that by adjusting the gas pressure, input rf power, and DC bias to the dust reservoir dust number density as well as the dust cloud volume can be controlled.

To understand the dust grain transport and confinement in the diffused plasma, the possible forces acting on the particle are estimated for a given discharge condition. The estimated electric field (E) to levitate the dust particles, which comes from the force (the gravitational force to the electrostatic force) balance condition [43] is as follows:

$$E = \frac{r_d^2 \rho g}{3\varepsilon_0 \phi_d}, \tag{4.1}$$

where, r_d is radius of the dust particle, ρ is mass density of particles, g is gravitational constant, ε_0 is dielectric constant of vacuum and ϕ_d is the dust surface potential.

For kaolin dust particles ($\rho = 2.6\ gm/cm^3$ and $r_d \sim 0.5$ to 5 μm), the required electric field turns out to be $\approx$ 1 V/cm to 12 V/cm. For calculations, we have considered the kaolin particles of average radius, $r_d \sim 3\ \mu$m. The gravitational force experienced by the particle of an average mass, $M_d \approx 2.8 \times 10^{-13}$ kg, comes out to be $F_g \sim 10^{-12}$ N. In the potential well, the downward gravitation force is mainly balanced by the upward electrostatic force, $F_E = Q_d E$. The charge on the dust grain is estimated using the Orbital Motion Limited (OML) theory, which has been discussed in subsection 1.3.1. For our discharge conditions (Fig. 4.3 (b)), charge on the dust grain comes out to be $Q_d \sim 4 \times 10^{-15}$ C. For this charge value, the vertical electrostatic force due to the Y-component of the E-field is estimated and it comes out to be $F_E \sim 10^{-12}$ N for the experimentally measured value of

E-field (from Fig. 4.6), E $\sim$ 3 V/cm. In this parametric regime, value of the ion drag force (F_i), which is acting in the direction of gravity comes out to be $\sim 10^{-13}$ N. The ion drag force acting on the charged dust particles is estimated using the Barnes formula [92], which has been discussed in section 1.4. It implies that the gravitational force is well balanced by the vertically electrostatic force for the present experimental condition to levitate the microparticles. Similarly, we have estimated the axial (along the Z-axis) E–field component using Fig. 4.5 and X-component using Fig. 4.7 to estimate forces to understand the dust confinement along the Z and X–axis. The dust–dust interaction or repulsive force (F_{int}) for the discharge parameters (Fig. 4.3(b) and Fig. 4.3(c)) is estimated as $F_{int} \sim 10^{-15}$ N for the inter-particle distance (d) of 0.6 mm. The magnitude of the Z and X component of the electrostatic force is estimated to be $\sim 10^{-12}$ N, whereas value of the ion drag force components come out to be $\sim 10^{-13}$ N. It clearly indicates that the electrostatic force dominates over the ion drag and dust-dust repulsive force, which confines the particles in the Z and X directions. Apart from theses forces, the equilibrium of the confined particles can be disturbed by the temperature gradient induced thermophoretic force [207, 208]. In our experimental configuration, an inductive coil is wound on the source tube that can heat up the glass chamber even at low power (3–10 W) but the dusty plasma is formed far from the source tube. Therefore, the contribution of thermophoretic force on the dust particle is considerably smaller compared to other dominating forces. Hence, we ignore the effect of thermophoretic force in our calculations. It essentially concludes that electrostatic force is dominating over the other forces (ion drag, dust-dust repulsive and thermophoretic) to trap the particles in a potential well of the diffused plasma.

The calculation of forces acting on dust particles (using Fig. 4.3(b) and Fig. 4.4) helps to understand the transport of dust particles in the diffused plasma. During the transport, dust particle motion is controlled by the axial electrostatic force, ion drag force, neutral drag force and the Coulomb repulsive force. The electrostatic force on the dust particles arises due to the gradient of axial plasma potential (see Fig. 4.4), which drags the particle towards the center of the potential. The magnitude of the axial electrostatic force, $F_E \sim 10^{-13}$ N at Z $\sim$ 16 cm. The ion drag force tries to drag the dust particles along its direction (opposite to the dust motion). The estimated value of the ion drag at the same location is, $F_i \sim 10^{-14}$ N. In the absence of neutral flow, the stationary background neutrals always resist the motion of dust particles. The force experienced by the flowing dust grains due to the neutral background is estimated using the Epstein formula, which has been discussed in Sec. 1.4. For the given pressure ($p = 0.05$ mbar) and dust drift velocity ($v_z = 1.2$ cm/sec), value of the neutral drag force comes out to be $F_n \sim 10^{-14}$ N. Since, the particles density is very low (at Z $\sim$ 16 cm); therefore, the Coulomb repulsive force is assumed to be negligible compared to the other forces. However, the Coulomb interaction between the drifted particles and the stationary dust cloud also plays an important role during the transportation near the confined cloud. It is clear from Fig. 4.8 that the drift velocity decreases gradually mainly because of this repulsive force that comes from the confined dust particles. The force estimation shows that an electrostatic force due to ambipolar E–field of the diffused plasma is the primary cause of the particle transport.

In an electrostatic trap of the diffused plasma, dust grains are found to confine in an electrodeless sheath under the combination of electric field due to diffused plasma (ambipolar E–field) and field due to the glass wall charging (sheath E–field). Depending upon the discharge conditions, these confined dust cloud can form an equilibrium large volume dusty plasma. It is also observed that the volume and the location of the dusty plasma can be changed by changing the discharge parameters. Since the potential well created in this configuration provides a better confinement to the dust particles; therefore, we can perform experiments for a longer time with a constant dust density. The dusty plasma volume exhibits various self–oscillatory motion at particular input rf power and gas pressure. An equilibrium 3D dusty plasma is also possible at low pressure (p $<$ 0.03 mbar) when dust density is tuned at low power (P $<$ 4 W). Fig. 4.9 shows the 2D image (in the X–Z plane) of a stable 3D dust cloud at P $=$ 7 W and p $=$ 0.06 mbar. The dust acoustic waves get excited in the large volume dusty plasma at higher power (P $>$ 8 W) and higher dust density for pressure below 0.1 mbar. A typical image of dust cloud (in Y–Z plane) exhibits the dust acoustic waves is depicted in Fig. 4.10. Sometimes it is also observed that the linear wave gets bifurcated and/or merged during the propagation along its direction. The encircle regions in Fig. 4.10 represent the wavefront splitting and merging, which may be due to the large size of the dust cloud. Self–oscillatory motion of a large volume dusty plasma at wide range of discharge parameters are discussed in next chapter.

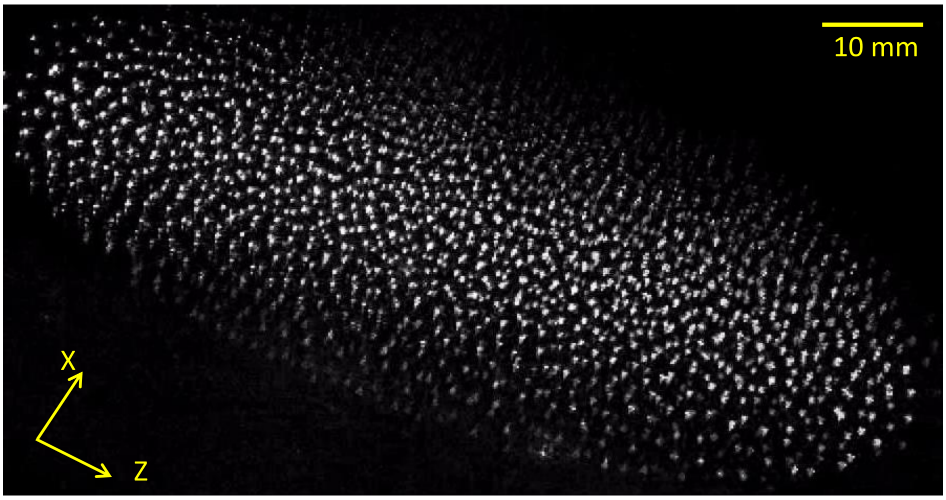

Figure 4.9: A snapshot of dust particles distribution in X–Z plane near the center of source tube (at Y ≈ -4 cm). The bright points correspond to the dust particles. Kaolin particles with average radius of ∼ 3 μm are used in this experiment. Input rf power and argon pressure is set to 7 W and 0.06 mbar, respectively. The field of view of an image is 8.94 mm × 2.8 mm

.

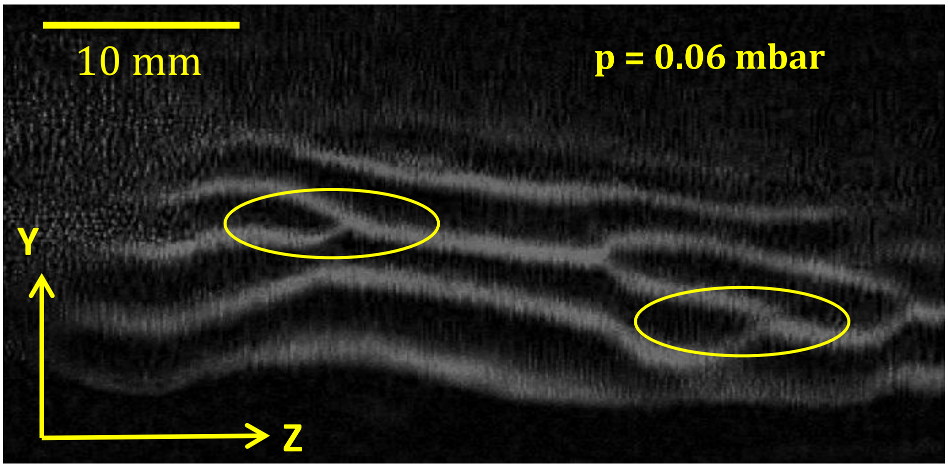

Figure 4.10: A single video frame of the dust cloud in Y–Z plane near the central region (at X ≈ -2 cm) shows the breaking and merging of dust acoustic wave at pressure p = 0.06 mbar and rf power P = 10 W. For this experiment, kaolin particles of average size ($r_d \sim 3$ μm) are used. The field of view of an image is 46.8 mm × 25.6 mm.

4.5 Summary and conclusions

In this chapter, we have provided a novel configuration using an inductively coupled diffused plasma to produce the large volume dusty plasma at low pressure. The discharge is initiated in the source section after passing a high-frequency current (13.56 MHz) through an inductive coil, which is wound on the source tube. Plasma is formed in the source section and diffuses into the experimental chamber. This diffused plasma is characterized thoroughly using different electrostatic probes. The non–uniformity in the plasma density and electron temperature of the diffused plasma in all axis gives rise to a potential trap, which can be used to confine the negatively charged dust grains. The characteristics of the potential well are investigated for a wide range of discharge parameters. For injecting the dust grains into the electrostatic trap, a unique technique using the DC glow discharge is employed. The homogeneously sprinkled dust grains get negatively charged while a negative bias voltage is applied to dust containing disk (dust reservoir) and found to levitate at the plasma–sheath interface. As these particles come into the plasma volume (due to poor confinement), they are drifted towards the electrostatic trap under the action of an axial ambipolar electric field, which comes from the diffused plasma. These transported particles are found to confine in the potential trap of the diffused plasma. In this potential trap, particles are trapped in the resultant E–field of the diffused plasma (ambipolar E–field) and glass wall charging (sheath E–field). As a result of this confinement, a large volume dusty plasma is formed at low pressure. According to the requirements, the volume of the dust cloud can be controlled very precisely by tuning the bias voltage on dust reservoir. This electrodeless dusty plasma device is free from micro-arcing, which can affect the dynamics of dust particles, is useful to study the collective phenomena in the large volume dusty plasma at low pressure.

The limitations to produce dusty plasma at a low pressure in the DC discharge configuration, as discussed in Chapter 3, have been resolved using the inductively coupled discharge configuration. This configuration provides a platform to study the dusty plasma dynamics at a wide range of discharge parameters. The self–oscillatory motion of dust grains in a large volume dusty plasma at low pressure are discussed in Chapter 5.

5

Multiple Co–rotating Vortex Structures

In this chapter, self–oscillatory motion of the large volume dusty plasma with inhomogeneous plasma background is presented. The collective dynamics of dust grains which gives rise to vortex motion is examined for a wide range of discharge parameters. The quantitative analysis of the origin of vortex motion and its multiplicity are discussed in detail.

5.1 Introduction

In the background of plasma, the interactions among the highly charged dust grains causes the dust grain medium to follow collective behavior. In presence of an infinitesimal perturbation in the dust medium, the background plasma instabilities [22, 23, 118] provide energy to enhance the local/infinitesimal perturbation of the dust grain medium. The evolution of local perturbation, which is result of the collective response of medium, appears in the form of dust acoustic modes [1, 5, 209–211] and dust vortices [27]. As discussed in Chapter 4, the large volume dusty plasma exhibits self–excited acoustic modes (Fig. 4.9) or attains an equilibrium state (Fig. 4.8) at different discharge conditions. Dusty plasma is a dissipative medium; therefore, the collective modes such as vortices are mainly established when the energy dissipation is compensated by the available free energy in the dust system. The main causes of energy dissipation are dust–neutral collisions and dust–dust frictions. The energy required to establish the vortex motion in presence of the weak magnetic field ($\mathbf{B} < 500$ G) is provided by the driven motion of plasma species (ions and electrons). On the imposition of magnetic field above a critical value, the ions and electrons set into the rotatory motion due to the $\mathbf{E} \times \mathbf{B}$ drift and exerts a drag on the dust grains and drives them along its motion [12,132–134,138,212,213]. The momentum transfer for electron to dust grain is minimal; therefore, dust motion can be approximated to be unaffected by the electron–drag force. The application of the strong magnetic field ($\mathbf{B} > 4$ T) can magnetize the micron-sized dust particles, which gyrate in a plane perpendicular to the magnetic field vector [135, 136].

The self–excited dust rotation and convective vortex motion have been observed in the various dusty plasma systems in the absence of an external magnetic field. Agarwal *et al.* [17] have observed the spontaneous rotation of dust grains in the DC glow discharge. The strongly coupled dusty plasma exhibits wave motion along with the vortex motion, which has been experimentally observed in the DC glow discharge and Inductively coupled discharge [214, 215]. In the DC glow discharge, the dusty plasma exhibits a 2–dimensional vortex flow in presence of an auxiliary biased object [137]. The poloidal rotation of dust grains with toroidal symmetry has been recently observed in the high pressure dusty plasma [13]. The rotation of dust clusters in the dusty plasma under different gas pressures has been experimentally studied by Feng *et al.* [138]. Spontaneous vortex flow in ice dusty plasma, which is confined in an rf sheath has been reported by Chai *et al.* [11]. The horizontal and vertical vortex motion of dust grains in presence of an auxiliary electrode near the levitated dust cloud in an RF sheath has been reported by Daw *et al.* [15] and Samarian *et al.* [139].

The rotation or vortex motion of dust particulates in the absence of magnetic field can be induced by asymmetric ion flow or sheared flow along with electric field [8, 216, 217], or Rayleigh–Taylor instability [218], or transient shear instability [219], or convection motion of the background gas [220, 221], or charge gradient of the particles along with the non–electrostatic forces [27]. Vaulina *et al.* [146, 222, 223] have carried out theoretical and numerical analysis of the dusty plasma medium having particle charge gradient orthogonal to the non-electrostatic forces (i.e. gravity or ion drag force). Their studies indicate that the spatial dependence of grain charge is a possible mechanism to convert the potential energy into the kinetic energy of the dust grains, which in turn induces the vortex flow in the dusty plasma. The spatial charge variation (gradient) of dust grain arises due to inhomogeneity in the plasma parameters such as plasma density (n) and electron temperature (T_e). All the reported work suggest that dust dynamics is strongly affected by the motion of background species (electrons, ions and neutral) and associated instabilities. The self–oscillatory motion of dust grain in a large volume dusty plasma at different plasma environments need to be explored.

In this Chapter, the dynamics of dust grains in the extended 2D planes of large volume dusty plasma, which gives rise to multiple co–rotating vortex structures is presented. The Chapter is organized as follows: Sec. 5.2 deals with the detailed description of the experimental setup, plasma and dusty plasma production and their characterization. The experimental observations of co–rotating multiple dust vortices and their characteristics are discussed in Sec. 5.3. Quantitative analysis of the origin of multiple vortices in the dusty plasma medium is presented in Sec. 5.4. A brief summary of the work along with concluding remarks are discussed in Sec. 5.5.

5.2 Dusty plasma and its characteristics

The experimental study of the self–oscillatory motion (e.g.vortices) of dusty plasma medium is carried out in the experimental device, which has been described in Chapter 4. The schematic of the experimental setup used in the present set of studies is depicted in Fig. 5.1(a). In this configuration, Z = 0 cm and Z = 60 cm correspond to the left axial (A1) and right axial (A2) ports of the experimental chamber (Fig. 2.1(a)), respectively. The X = 0 cm and Y = 0 cm indicate the points on the axis that passes through the centre of the experimental tube. The center of the source tube (P1) is located at Z $\sim$ 12 cm. This chapter mainly focuses on the study of self–excited collective modes of a large volume (3D) dusty plasma at low pressure (p = 0.04 mbar). It is well known that video imaging is a primary diagnostic tool to track the dust grain dynamics, thereby, it is difficult to diagnose the 3D dusty plasma directly using it. The characteristics of 3D dusty plasma can be obtained after assembling a stack of images of 2D planes within the volume of the dust grain suspension. In our experiments; even though, the dusty plasma has 3D nature but the imaging tools restrict us to track the dynamics in a 2D plane; therefore, dust grain dynamics is studied in an extended dust cloud in different 2D planes. It is observed that dust cloud is homogeneous in the axial direction near the center of source section (at Z$\sim$ 12 cm) where plasma potential

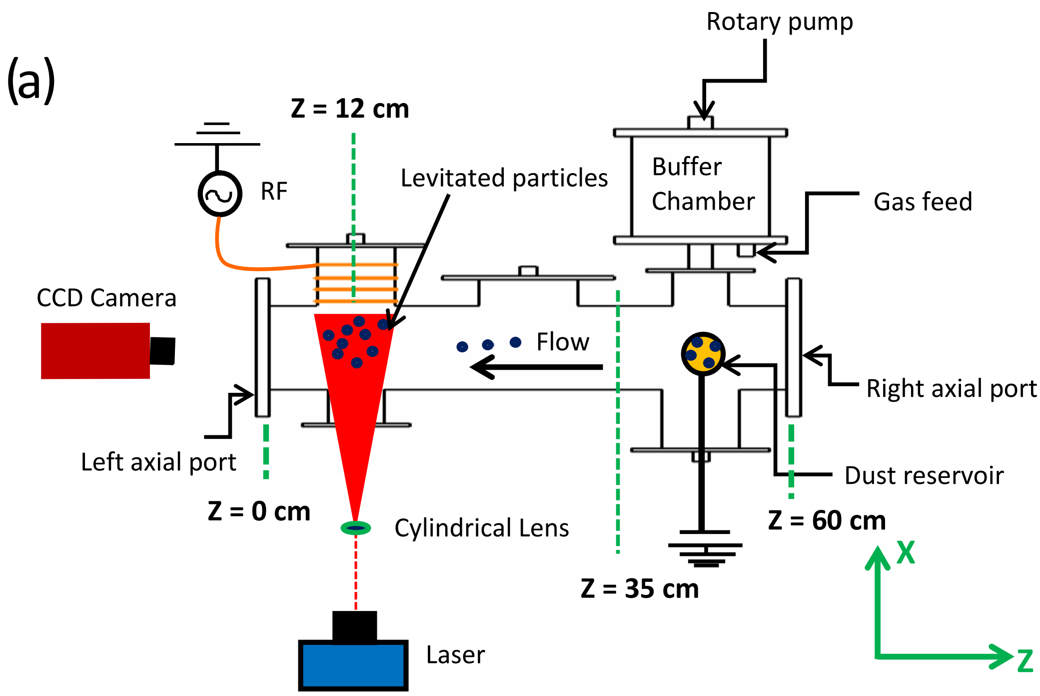

is nearly uniform (see Fig. 4.5). To reduce the complexity of dust grain dynamics and to get an extended dust cloud, we limit our studies in the X–Y plane at different Z-locations. The arrangement of red diode laser and a cylindrical lens to illuminate the dust grains in the X–Y plane is shown in Fig. 5.1(a). To record the dust dynamics in the X–Y plane, the scattered Laser light is captured through axial port (A1) with the help of a CCD camera, having a frame rate of 16 fps and spatial resolution of 2352 $\times$ 1768 pixels, and a standard zoom lens. The series of images are then stored into a high-speed computer and later analyzed with the help of ImageJ software [177] and MATLAB based open access software, called openPIV [178]. Fig. 5.1(b) is a snapshot of the diffused plasma (P = 6 W and p = 0.04 mbar) in the X–Y plane, which represents the location of confined dust grains. A video image of the full view of the confined dust cloud in the X–Y plane at Z $\sim$ 12 cm is shown in Fig. 5.1(c). The dotted lines in this figure correspond to real coordinate system to describe the dust grain dynamics.

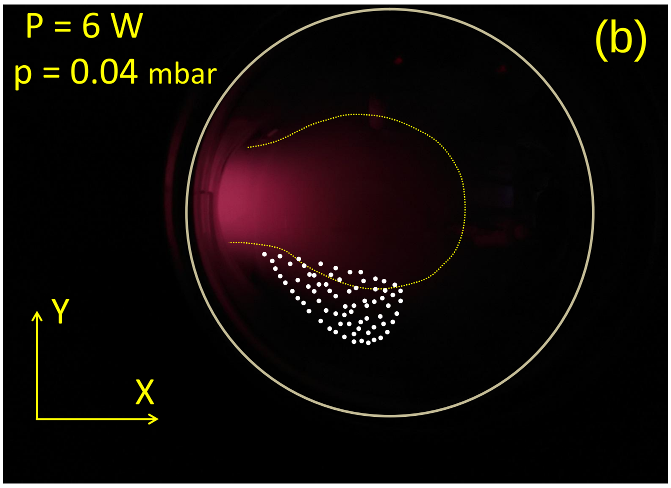

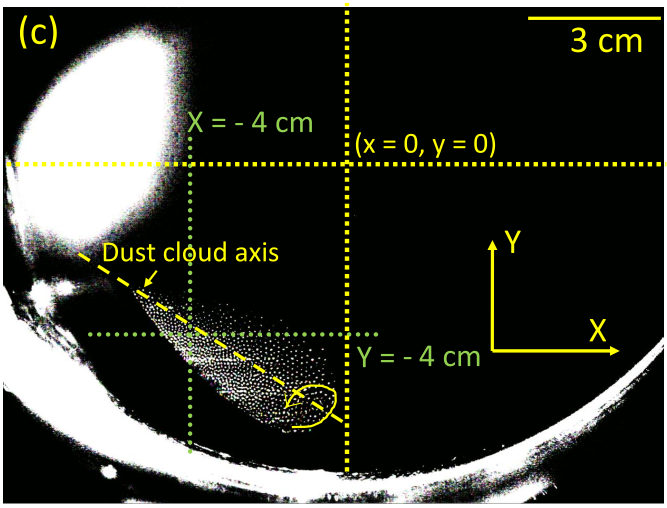

Figure 5.1: (a) Schematic of experimental configuration (top view). (b) A snapshot of the diffused plasma in the X–Y plane at Z $\sim$ 12 cm when gas pressure and input power are set to 0.04 mbar and 6 W, respectively. The white closed loop represents the boundary of the left axial port (A1) and the yellow dotted line represents the boundary of the diffused plasma. Confined dust particles at the edge of the glow are indicated by white spots. (c) A full view image of the confined dust cloud in the X–Y plane near the center of source tube (Z $\sim$ 12 cm). The yellow line with arrow indicates the direction of the rotating particles in the X–Y plane. The circular arc (due to the reflected light) indicates the inner boundary of glass chamber. The position of the dust cloud can be determined by using the reference of yellow dotted lines. The green dotted lines represent the typical measurement axes (along X and Y axis) for a given X and Y values. The yellow dashed line represents the typical axis of the confined dust cloud in this plane.

5.3 Observations on dust vortices

This section discusses dust dynamics in an extended dust cloud in the X–Y plane (at Z $\sim$ 12 cm) at different input rf powers and the velocity distribution of the particles in corresponding vortex structures. We also provide some results on the vortices in different X–Y planes at a fixed input power, which give some insight into the dynamics of large volume dusty plasma.

5.3.1 Vortices in a plane at different input RF powers

It has been discussed in Chapter 4 that dust particles are confined near the centre of source region (at Z $\sim$ 12 cm) and form a 3D dusty plasma. As we have discussed, imaging limitations restrict us to study the dusty plasma volume (3D) at any instant. To study the dynamics of dust grains, 2D images of the 3D dusty plasma are captured in different X–Y planes at a given Z location of dust cloud. At higher rf power (P $>$ 8 W) and low pressure (p $=$ 0.04 mbar), the dust cloud is observed to be unstable due to the instabilities (ion streaming instability or dust-acoustic instability) associated to the dusty plasma. The collective motion of the grain medium gives rise to dust acoustic waves. The present work keeps away from the study of dust acoustic waves; therefore, these results are not being discussed. The dynamics of dust particles in the X–Y plane at Z $\sim$ 12 cm with different rf powers at fixed argon pressure, p $=$ 0.04 mbar is depicted in Fig. 5.2. Five consecutive frames at a time interval of 66 ms are superimposed to get information of the trajectories of the different particles. Continuous trajectories are seen in Fig. 5.2(a)–Fig. 5.2(c) for particles which follow a particular trajectory (or directed motion), whereas the randomly moving particles show only the dotted points. The dynamics of dust grain get changed when power is changed. At P $=$ 7.5 W and p $=$ 0.04 mbar, almost all of the particles participate in rotational motion in the form of separate, co–rotating, anti–clockwise multiple (three) vortices as shown in Fig. 5.2(a). It is to be noted that the vortices are found to be stable until the discharge parameters remain unchanged. Small changes in the ambient plasma parameters lead to the distortion in the vortex structures. It is also observed that dust cloud dimension (specially length of the dust cloud) is changed when the input rf power is reduced. This is due to falling down of the particles from the dust cloud edge. When rf

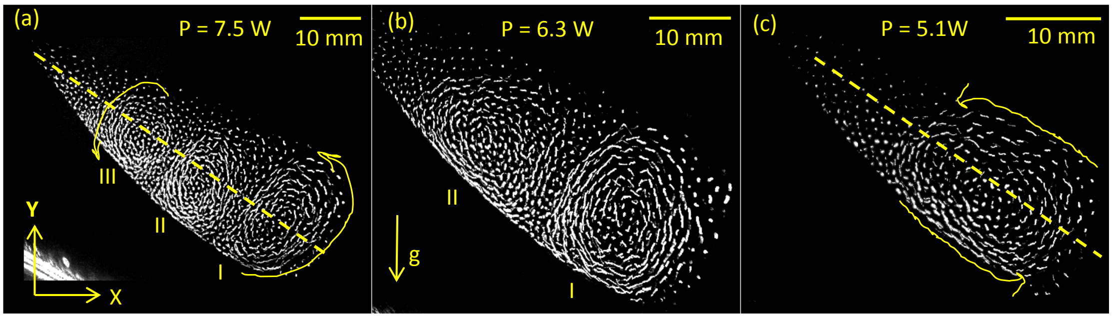

Figure 5.2: Video images of the dust cloud in the X–Y plane at Z $\sim$ 12 cm. Images ((a) – (c)) are obtained by the superposition of five consecutive images at a time interval of 66 ms. Fig.5.2(a)–Fig.5.2(c) are observed vortex structures at different input rf power (P) 7.5 W, 6.3 W and 5.1 W, respectively. The yellow solid lines with an arrow indicate the direction of vortex motion of dust grains and dashed line corresponds to the axis of the dust cloud. The vortex representation (I, II, and III) are made based on the number notation from the outer edge of the dust cloud. Kaolin particles are used to perform the dusty plasma experiments at argon pressure 0.04 mbar.

power decreases to 6.3 W then dust cloud length reduces. At this rf power, P = 6.3 W, two co–rotating (anti–clockwise) dust vortices are observed in the dust cloud (see Fig. 5.2(b)). Dust cloud length and dust density decrease with further reduction of power to 5.1 W. At this discharge condition, the dust particles form an elongated single vortex structure (see Fig. 5.2(c)) along the dust cloud axis. It is worth mentioning that dust particles near the mouth of the diffused plasma (nearby the plasma source) always exhibit the random motion.

5.3.2 Velocity distribution in vortex structures

The Particle Image Velocimetry (PIV) technique [21] is used to determine the direction and the magnitude of the particle velocity in each vortex structure with the help of a MATLAB based open access software (openPIV) [178] . For constructing the vector field, an adaptive 2-pass algorithm (a 64×64, 50% overlap analysis, followed by a 32×32, 50% overlap analysis) is considered. The contour map of the average magnitude of the velocity, constructed after averaging the flow fields of 40 frames, is shown in Fig. 5.3. The direction of the field vectors (shown by arrows in the figure) represents the direction of particles motion in X–Y plane. The average velocity (v_d) profile of the rotating particles confirms the non-uniform

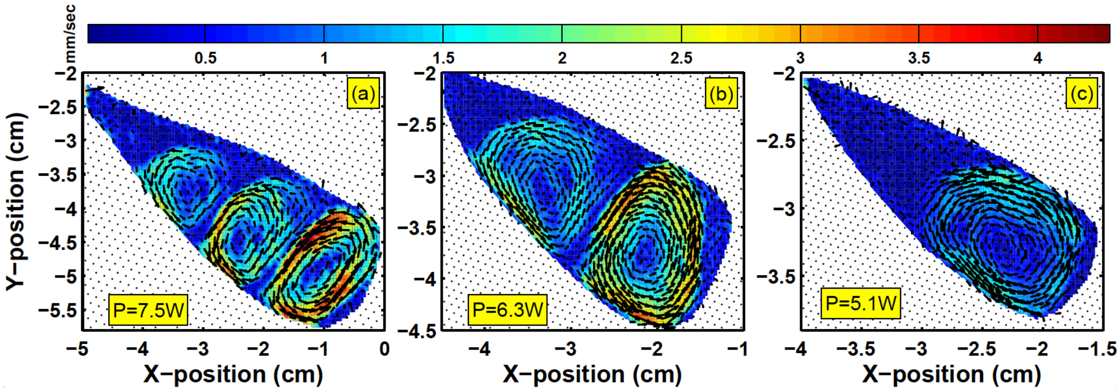

Figure 5.3: Images show the velocity distribution of dust particles in a vortex structure at different input rf powers (Fig.5.2). Images (Fig.5.3 (a)–Fig.5.3(c)) are obtained after PIV analysis of the corresponding still images. Velocity vectors are showing the direction of the rotating particles in X–Y plane at Z $\sim$ 12 cm. Color bar on the images show the value of dust velocity in mm/sec. Three anti–clockwise co–rotating dust vortices are observed in the extended dust cloud at P = 7.5 W (Fig.5.3(a)). Dust cloud supports only two co–rotating vortices when input power is 6.3 W (Fig.5.3(b)). A single anti–clockwise dust vortex is observed at power of 5.1 W (Fig.5.3(c)). All the measurements are taken at fixed gas pressure of 0.04 mbar

.

velocity distribution of particles in a particular vortex structure, which is shown in Fig. 5.3(a). The particles rotate with minimum velocity at the center of the vortex and increasing towards the boundary. The velocity profile of the three vortices (see Fig. 5.3(a)) at their boundary clearly show that particles in the biggest vortex (vortex–I) have maximum velocity and minimum in the smallest vortex (vortex–III). It is worth mentioning that the interface (having anti–parallel flow) of two consecutive vortices are well separated. However, it is noticed that the magnitude of the velocity of the particles in vortex structure depends on the density of dust particles. The maximum velocity of the particles (at the boundary) in the vortex structure decreases with the decrease of input rf power, which is clearly seen in Fig. 5.3. The maximum velocity (for vortex–I) is observed to be $\sim$ 4 mm/sec and $\sim$ 2 mm/sec at input power P = 7.5 W and P = 5.1 W, respectively. It is also to be noted that all the dust particles do not follow a closed path in the X–Y plane (some of the particles move to another plane) but the dust density remains nearly constant in the vortex structures.

The radial dependence of particles velocity (v_d) and angular velocity (ω) of vortex–I at P = 6.3 W (as shown in Fig. 5.2(b)) are displayed in Fig. 5.4. The

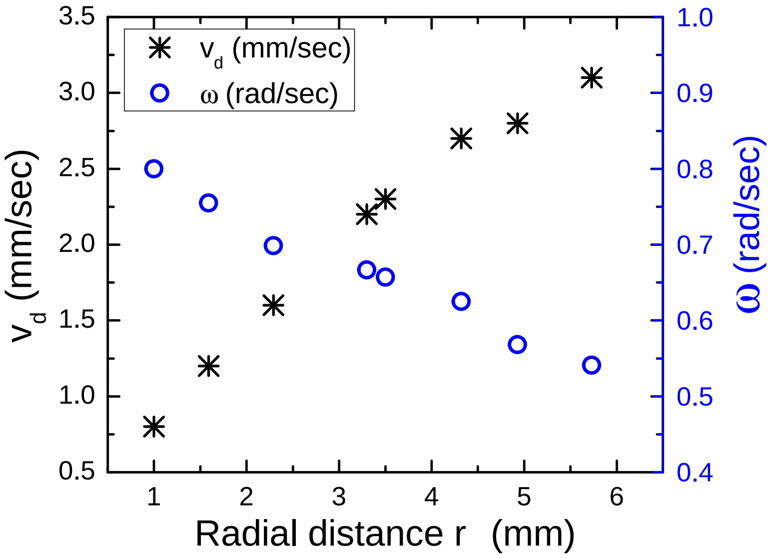

Figure 5.4: Radial variation of speed of particle and angular velocity for Vortex-I (Fig. 5.2(b)) at P = 6.3 W and p = 0.04 mbar. Here, r = 0 mm corresponds to X = -2.1 cm, Y = -3.7 cm and r = 6 mm corresponds to X = -1.5 cm, Y = -3.7 cm. Errors in the measured values are within 10%.

measurements are taken from the centre (X_0 = -2.1 and Y_0 = -3.7 cm) of the vortex–I to the outer edge (X = -1.5 and Y = -3.7 cm) of the same vortex (see Fig. 5.3(b)). These two points of Fig. 5.4 are denoted by r = 0 and r = $\sqrt{(X_0 - X)^2 + (Y_0 - Y)^2}$ = 6 mm, respectively. It is observed that the speed of the particles (v_d) increases linearly towards the outer edge of the vortex. The speed of particles is found to be higher with a large number of dust grains involving in the formation of vortex structure. It is also seen that the angular velocity (calculated from $\omega = v_d$/r) of rotating particles has a radial variation toward the outer boundary of the vortex.

5.3.3 Vortices in different planes at a constant power

It is observed that the confined dust grains form a large 3D dusty plasma near the center of source tube (Z ∼ 12 cm). And dust cloud is extended on the both sides of the central region, which is shown in Fig. 4.9. The dynamics of the dust grains in different X–Y planes can show some characteristics of the large volume (3D) dusty plasma; therefore, the dynamic structures at different X–Y planes (i.e., at different Z locations) are investigated for a fixed discharge condition. Observation of the dust vortices in different planes are shown in Fig. 5.5(a)–Fig. 5.5(c). It should be noted that the dust cloud has its maximum dimension near the centre of the source

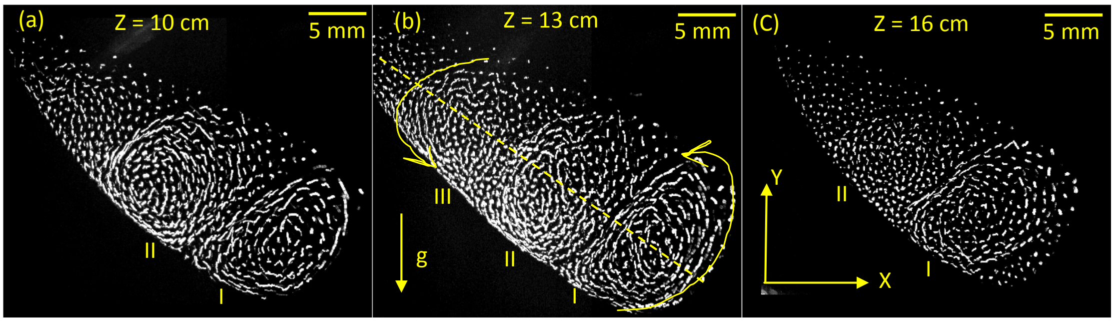

Figure 5.5: Video images of the dust cloud in different X–Y planes. All the images are obtained by the superposition of five consecutive images at a time interval of 66 ms. Fig.5.5(a)–Fig.5.5(c) corresponds to Z = 10 cm, Z = 13 cm and Z = 16 cm, respectively. Yellow lines with an arrow indicate the direction of the rotating particles in the extended cloud. The measurements are taken at fixed gas pressure 0.04 mbar and input rf power 7.5 W.

region (Z $\sim$ 13 cm), which then decreases if one goes away from the source region. The number of vortex structures depends on the dimension of the dust cloud. For example at P = 7.5 W and p = 0.04 mbar, three vortices are formed at Z $\sim$ 13 cm, whereas at other locations (Z $\sim$ 10 and 16 cm) only two vortices are observed. The observations suggest that the vortex structures are indeed 3D in nature but the camera sees only 2D image of 3D expending dust structure. At present, our focus is on the study of the multiple vortex structures in an extended dust cloud, detailed studies on 3D characteristic of the vortices will be carried out in future work.

5.4 Origin of multiple dust vortices

In this section, we provide the qualitative as well as quantitative description of the formation of a vortex structure and its multiplicity in an extended dust cloud. For the quantitative analysis of the vortex motion, a theoretical model proposed by Vaulina *et al.* [27] is used. The details are given as follows:

5.4.1 Formation of a vortex

For the formation of a steady-state equilibrium dust vortex, as described in Sec. 5.3, energy dissipation of the particles due to frequent dust–neutral collision and/or dust–dust interaction has to be balanced by the available free energy. The spatial dependence of dust charge is one of the possible mechanisms to convert the potential energy into the kinetic energy of the dust particles [27, 146, 222], which can drive the vortex flow in a dusty plasma. The monotonic variation (gradient) of dust charge in a dusty plasma occurs due to inhomogeneity in the plasma parameters such as electrons (ions) density ($n_{e(i)}$) and/or electrons (ions) temperature ($T_{e(i)}$). In addition to that, poly–dispersive nature of the dust particles sometimes also play an important role in creating a charge gradient in a confined dust column. The present studies are carried out in an inductively coupled diffused plasma where inhomogeneity in T_e and $n_{e(i)}$ are expected,which can result in a charge gradient along the length of the dust cloud. Theoretical analysis and numerical simulations show such type of dynamical structures (vortices) in the presence of a dust charge gradient, $\vec{\beta} = \nabla Q_d = e\nabla Z_d$, orthogonal to a nonelectrostatic force $\vec{F}_{non}$ such as gravitational force ($\vec{F}_g$), ion drag force ($\vec{F}_I$), or thermophoretic force ($\vec{F}_{th}$) acting on the dust particles in the dust cloud [27, 146, 222]. The role of non–electrostatic forces ($\vec{F}_{non}$) in the formation of dynamical structures in the dusty plasma is determined by their capacity to hold the particles in the region of the non-zero electric field.

Vaulina *et al.* [27, 146, 222] have carried an extensive study to explain the self-oscillatory motion (acoustic vibrations, vortex etc.) in a dusty plasma with an inhomogeneous plasma background. In such a dusty plasma medium, they found that the curl of the total force acting on an individual particle is non-zero due to a finite value of $\vec{\beta} \times \vec{E}$. In this case, the electric field does positive work in compensating dissipative energy losses. An infinitely small perturbation emerging in the dust cloud due to thermal and/or charge fluctuations in such a system grows in the absence of any restoring force and triggers an instability, which is known as the dissipative instability [222]. The evolution of this instability gives rise to regular dynamic structures (or vortices). The particles in a dust cloud start to move in the direction of F_{non} where the particle has its maximum charge value and form a vortex structure. In the vortex motion, the vorticity ($\Omega = \nabla \times \vec{v}_d$) is non-zero along a certain closed curve. The frequency (ω) of the steady–state rotation of particles in a vortex structure is given by [27, 146, 222]

$$\omega = \left| \frac{F_{non}}{M_d} \frac{\beta}{eZ_0\nu_{dn}} \right|, \tag{5.1}$$

where $Z_0 = Q_{d0}/e$ is the charge on the dust particle at an equilibrium position in the rotating plane. In the present experimental configuration, the dust cloud is confined in a X–Y plane (Fig. 5.1(c)). It is realized that the non–electrostatic force $\vec{F}_{non}$ required for the formation of the vortex motion of the particle is induced by the directional motion of ions relative to the dust particles, i.e. $\vec{F}_{non} = \vec{F}_I$ (ion drag force) [224]. Hence, $\vec{F}_{non}$ can be replaced by $\vec{F}_I$ in Eq. (5.1) to obtain the angular frequency of rotation. It should be noted that the force experienced by the particle due to gravity is not found to be orthogonal to the charge gradient; therefore, its role in the vortex motion is not included in the calculations. However, its component along the ion drag force also contributes to the vortex motion. The schematic representation of the vortex motion in the presence of charge gradient (β) and non–electrostatic force (F_I) in the X–Y plane is depicted in Fig. 5.6. According to Matsoukas and Russel's approximations [225], the charge on the dust grain (Q_d) can be expressed as:

$$Q_d = eZ_d \approx C\frac{4\pi r_d k_B T_e}{e^2} ln\frac{n_i}{n_e}\left(\frac{m_e T_e}{m_i T_i}\right)^{\frac{1}{2}}, \tag{5.2}$$

where r_d is radius of the micro-particle, k_B is Boltzmann's constant, e is the electron charge, n_e and n_i are the electron and ion densities, m_e and m_i are their masses, and T_e and T_i are their temperatures. For a typical argon plasma, the constant C comes out to be ≈ 0.73 [225].

Ion drag force $\vec{F}_I = F_i\hat{E}$, where F_i is the magnitude of the ion drag force which is estimated using the Barnes formula. The complete formulation for the ion drag force is given in section 1.4. The neutrals (either in rest or in motion) affect the motion of the dust particles in the plasma. In the present set of experiments, the directed gas flow inside the chamber is negligible [26] thus neutrals are assumed to be in thermal equilibrium (or stationary). The force experienced by the dust grains in the stationary background of neutral atoms has also been discussed in section 1.4. The expression for the dust–neutral frequency (ν_{dn}) is

$$\nu_{dn} = \frac{8}{3}\sqrt{2\pi}r_d^2\frac{m_n}{m_d}n_n v_{Tn}\left(1+\frac{\pi}{8}\right), \tag{5.3}$$

where m_n, n_n, and v_{Tn} are the mass, number density, and thermal velocity of the neutral gas atoms, respectively.

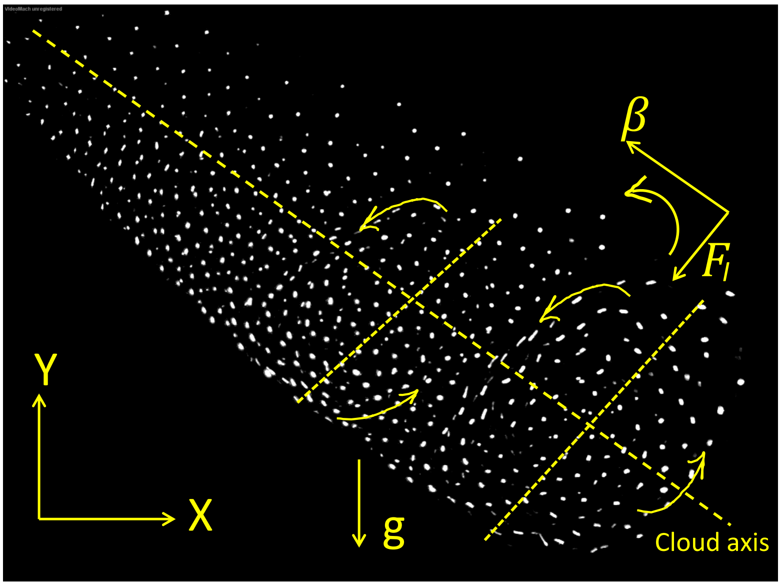

Figure 5.6: Video image of dust cloud in a X–Y plane with direction of charge gradient (β) and the ion drag force (F_I). The direction of rotation is represented by a yellow line with arrow. Dust grains rotate in the direction of the gradient of dust charge.

To estimate the angular frequency of dust rotation, it is necessary to estimate the dust charge gradient β along the dust cloud axis and ion drag force F_I, which are assumed orthogonal to each other. It is discussed in section 5.3, the dust cloud axis always lies in the X–Y plane (see Fig. 5.1(c)). For calculating the dust charge gradient along the dust cloud axis, the plasma parameters such as electron temperature (T_e) and plasma density (n) are measured. The present experimental configuration restricts us to trace the plasma parameters along the axis of dust cloud; therefore, they are scanned along the X–axis for given Y locations and along the Y–axis for given X locations at Z $\sim$ 12 cm. These measurements are then used to reconstruct the profiles of plasma parameters along the axis of dust cloud.

The typical variation of T_e along the X–axis at Y $\approx$ -3 cm and Z $\sim$ 12 cm for different rf powers (6.3 W and 5.1 W) in the absence of particles is shown in Fig. 5.7(a). It is seen in Fig. 5.7(a) that there is non–uniformity (or gradient) in T_e along the X–axis for different rf powers. T_e is observed to be high near the plasma source (at X = -7 cm) and decreases along the length of diffused plasma (from X = -7 to X = +3 cm). The typical variation of T_e along the Y–axis at X $\approx$ -4 cm and Z $\sim$ 12 cm is depicted in Fig. 5.7(b). It is clear from Fig. 5.7(b) that T_e also has

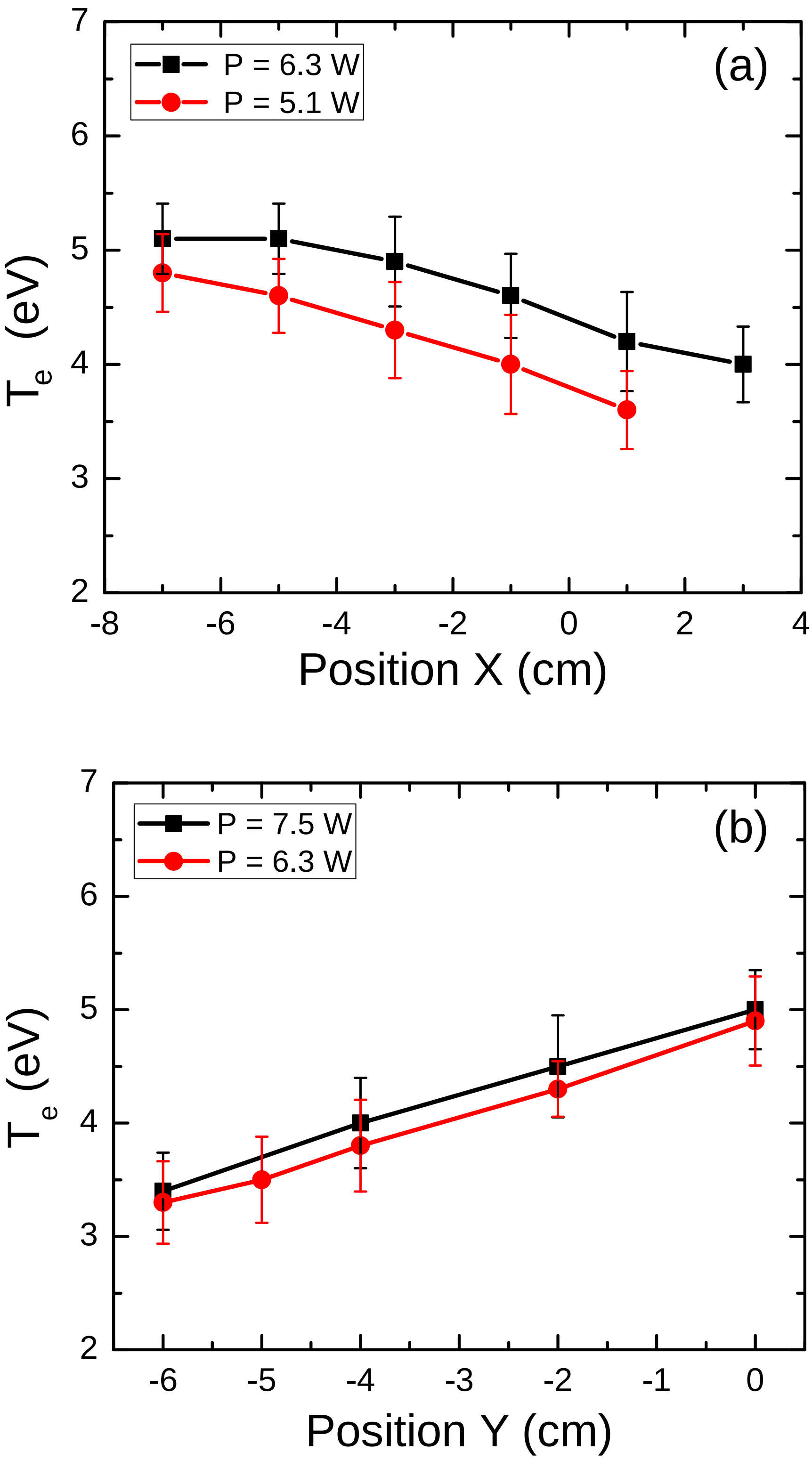

Figure 5.7: (a) Electron temperature (T_e) variation along the X–axis at Y ≈ -3 cm and Z ∼ 12 cm for two rf powers, P = 6.3 W and 5.1 W. (b) T_e variation along Y–axis at X ≈ -4 cm and Z ∼ 12 cm for two rf powers, P = 7.5 W and 6.3 W. All the measurements are taken in the absence of the dust particles at gas pressure, p = 0.04 mbar.

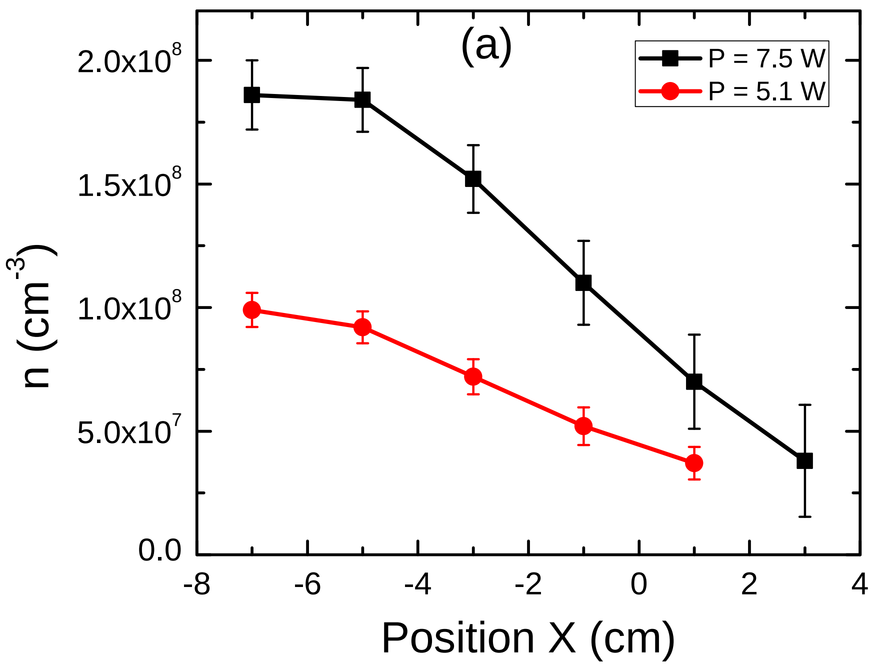

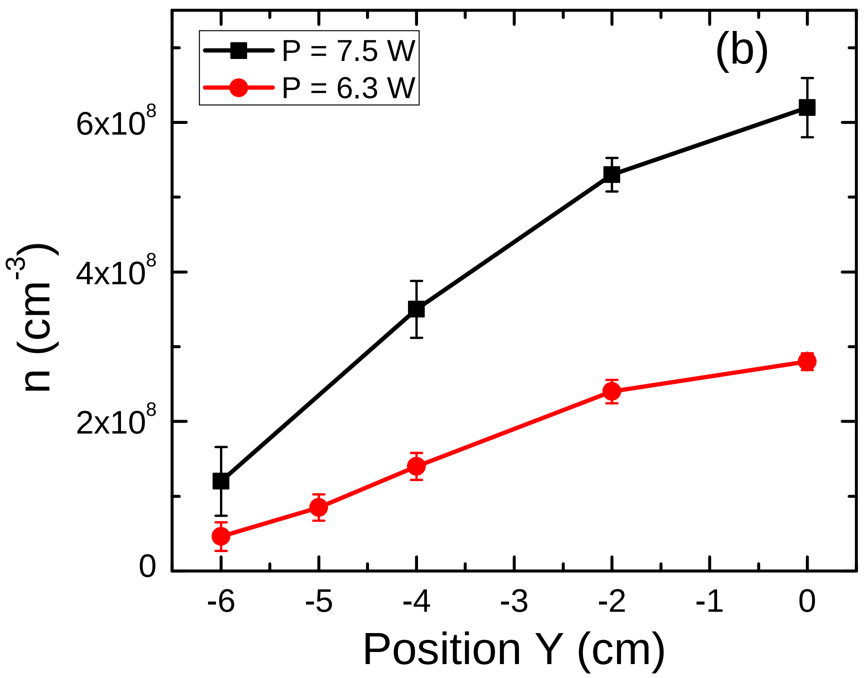

Figure 5.8: (a) Plasma density (n) variation along X–axis at Y $\approx$ -3 cm and Z $\sim$ 12 cm for two rf powers, P = 6.3 W and 5.1 W. (b) plasma density variation along Y–axis at X $\approx$ -3 cm and Z $\sim$ 12 cm for two rf powers, P = 7.5 W and 6.3 W. All the measurements are taken in the absence of the dust particles at gas pressure, p = 0.04 mbar.

a gradient along the Y–axis for different rf powers. Similarly, the typical plasma density variation along the X–axis at Y $\approx$ -4 cm and along Y–axis at X $\approx$ -3 cm with different rf powers are displayed in Fig. 5.8(a) and Fig. 5.8(b), respectively. The plasma density varies monotonically along the length of diffused plasma. It is higher near the plasma source and decreases towards the chamber wall.

Fig. 5.9(a) and Fig. 5.9(b) represent the variation of T_e and n along the dust cloud length for P= 7.5 W and 6.3 W. These plots are constructed using the measured values of T_e and n along the X–axis (X = -6 cm to 0 cm) for different Y values (Y $\approx$ -1, -3, -4 and -6 cm) and along the Y–axis (Y = -1 cm to -6 cm) for different X values (X $\approx$ -6, -4, -2 and 0 cm) at Z $\sim$ 12 cm. It is clear from these figures that there exists a finite gradient in electron temperature (see Fig. 5.9(a)) and plasma density (see Fig. 5.9(b)) along the dust cloud axis for a given rf power. For the estimation of charge resides on dust surface and its gradient, an expression (Eq. 5.2) is used, which clearly indicates that the gradient of plasma density and electron temperature causes a gradient in dust charge along the axis of the dust cloud. However, the effect of plasma density gradient on the dust charge gradient is found to be negligible than that of electron temperature gradient.

For the estimation of electric fields along X and Y directions near the region where dust particles get levitated, the plasma potential (V_p) is measured. The plasma potential profiles at different rf powers are plotted in Fig. 5.10. Fig. 5.10(a) shows the potential profile along the X–axis for Y $\approx$ -4 cm, whereas Fig. 5.10(b) shows the same along the Y–axis for X $\approx$ -4 cm near the center of the source tube (at Z $\sim$ 12 cm). It is to be noted that the plasma potential gradient near the glass wall (or diffused edge) is observed to be higher at higher rf power, which gives a higher E–field near the glass wall. The vertical E–field (along Y–axis) component holds the particles against gravity and the horizontal component (along X–axis) confines the particles as discussed in Chapter 4. It is also seen in the Fig. 5.10(a) that the X–component of E–field is negligible (flat V_p) inside the dust cloud (from X= -3 to +1 cm) and it has a finite value at the both edges of the dust cloud. It essentially indicates that the E–field has both components in a plane where the dust particles are confined. The direction of the E–field ($\hat{E}$) is assumed to be perpendicular to the curved glass wall (Fig. 5.1(c)), which is orthogonal to the dust cloud axis (or along the direction of charge gradient).

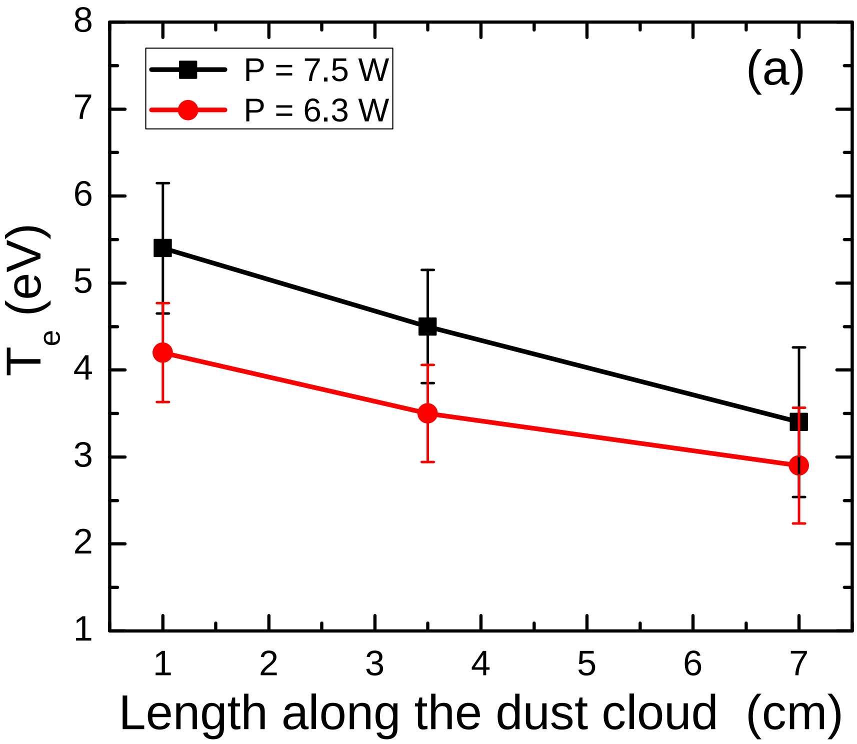

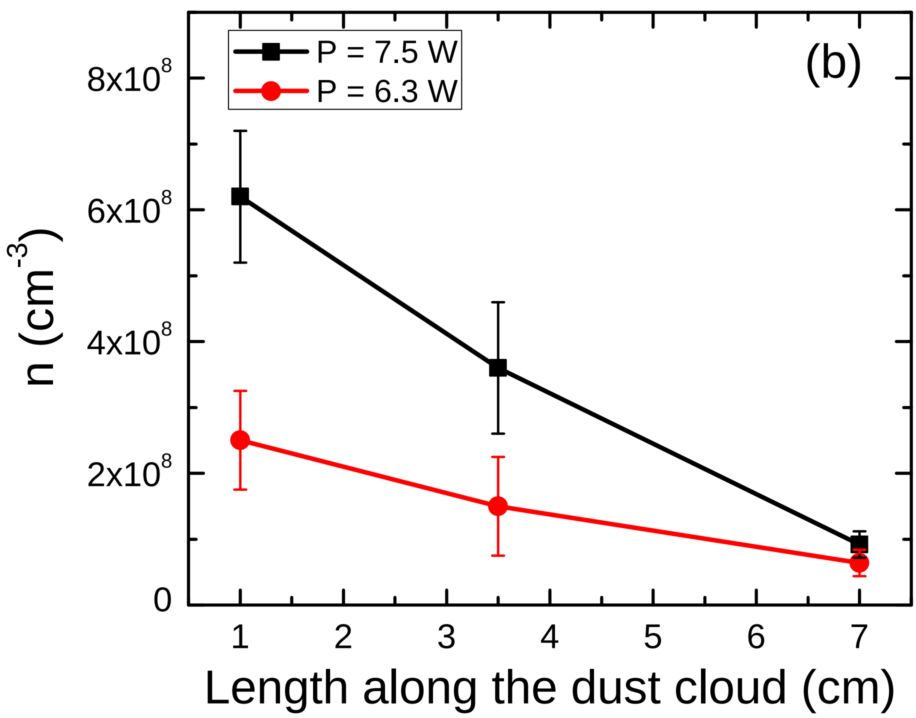

Figure 5.9: (a) Electron temperature (T_e) and (b) plasma density (n) variations along the axis of confined dust cloud at rf powers of 7.5 W and 6.3 W. All the measurements are taken in the absence of the dust particles at gas pressure, p = 0.04 mbar

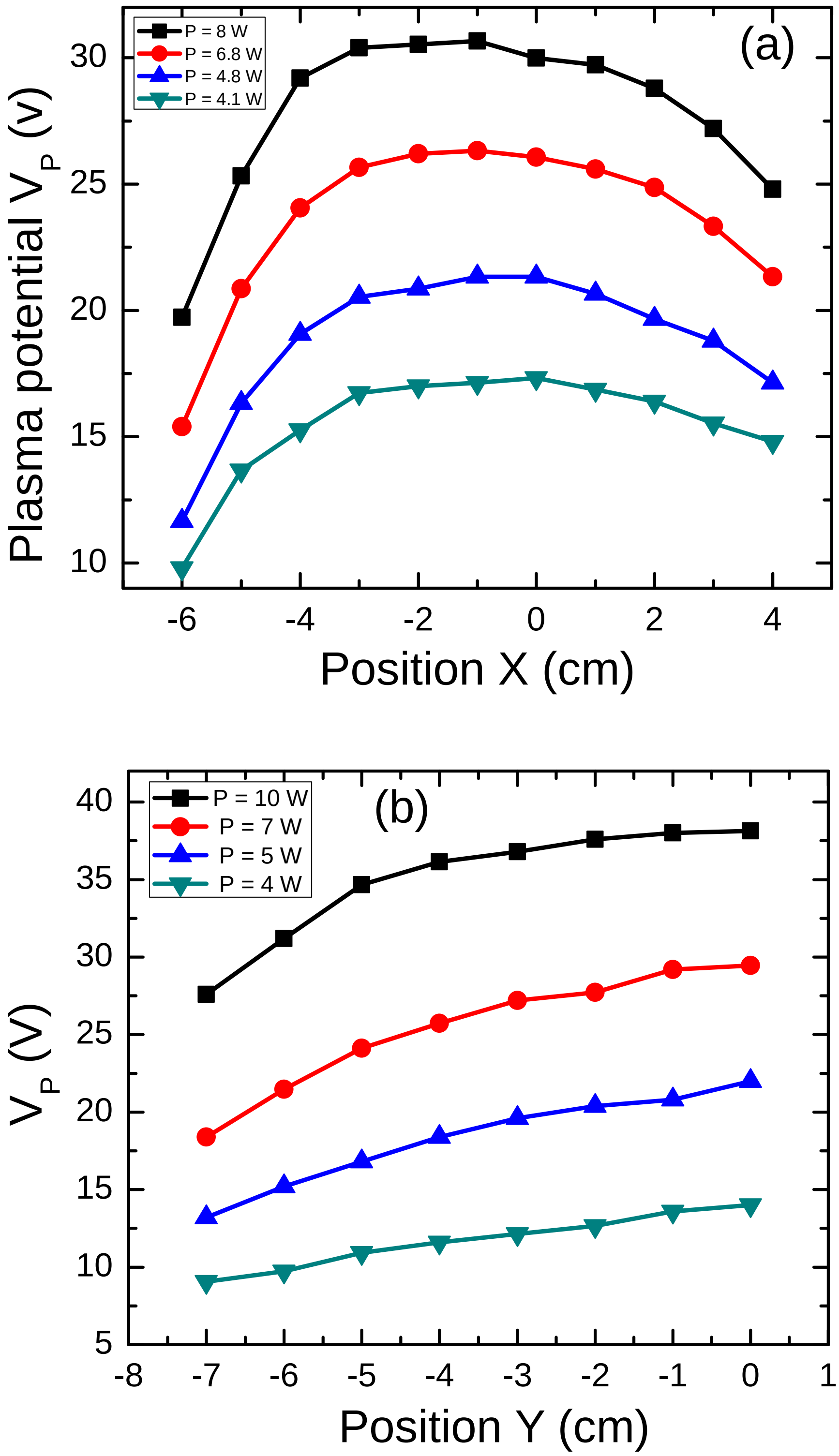

Figure 5.10: (a) Plasma potential profile along the X–axis at Y ≈ -4 cm and Z ∼ 12 cm (b) along the Y–axis at X ≈ -4 cm and Z ∼ 12 cm for different rf powers. The plasma potential measurements are taken with an emissive probe using floating point method. The argon pressure is kept fixed at 0.04 mbar during the experiments. Errors in the measured value of plasma potential are within ± 2 V.

The charge gradient along the axis of dust cloud is defined as $\nabla Q_d = (Q_{d2} - Q_{d1})/(d_2 - d_1)$, where d_1 and d_2 are two spatial points on the dust cloud axis. For a quantitative analysis, only average sized particles (~ 2 μm) are considered based on the force balance conditions. As shown in Fig. 5.4, the observed value of angular frequency (ω_{exp}) at P = 6.3 W and p = 0.04 mbar is found to be in the range of $\sim$ 0.5–0.8 rad/sec. The theoretically estimated value of angular frequency (ω_{th}) comes out to be $\sim$ 0.5 rad/sec for $\beta/eZ_0 \sim 0.08$ cm^{-1}, $M_d \sim 8 \times 10^{-14}$ kg, $F_I \sim 7 \times 10^{-14}$ N and $\nu_{dn} \approx 8$ sec^{-1}. Similarly, ω_{exp} and ω_{th} are found to be $\sim$ 0.6–0.9 rad/sec and 0.4–1.1 rad/sec at P = 7.5 W, respectively. At lower power (P = 5.1 W), the experimentally measured angular frequency $\omega_{exp} \sim$ 0.5–0.6 rad/sec is comparable with the estimated angular frequency $\omega_{th} \sim$ 0.4–0.6 rad/sec. It can be concluded that the measured values of angular frequency and the theoretically predicted values (by Vaulina *et al.* [27]) are in good agreement for different rf powers. Moreover, the direction of rotation of the observed dust vortex is also consistent with the direction predicted by their theoretical model. It essentially confirms that the charge gradient of micron–sized particles is a possible energy source to drive the vortex motion.

5.4.2 Formation of the multiple vortices

The characteristic size D_0 of the vortices can be obtained from the viscosity (η_k) of the dusty plasma medium [28], as $D_0 = \alpha\,(\eta_k/(\omega^* + \nu_{dn}))^{1/2}$, where ω^* is effective dusty plasma frequency and α takes into account the difference between viscosity in quasi–stationary and dynamic vortex structure. The coefficient is estimated as $\alpha \approx 49$ [28]. The variation of kinetic viscosity (η_k) with a wide range of discharge parameters and coupling parameter (Γ) is reported by Fortov *et al.* [226]. For the present set of experiments, the effective coupling constant (Γ^*) [28] has values between 10 to 100 for the particle of size (r_d) ~ 2 μm, inter–particle distance (d) $\sim$ 700–900 μm, particle temperature (T_d) $\sim$ 0.2–0.4 eV and dust charge (Q_d) $\sim$ 1–5 $\times 10^{-15}$ C. In this parametric regime, the kinetic viscosity η_k is considered to be $\sim$ 0.01 to 0.04 cm^2s^{-1} similar to the value reported in Refs. [226, 227]. The characteristic size (D_0) of the vortices (shown in Fig 5.2(a)) for the parameters η_k = 0.02–0.03 cm^2s^{-1}, $\nu_{dn} \approx 8$ s^{-1}, $\lambda_D \sim 130$ μm and $\omega^* \sim 40$ s^{-1} comes out to be $\sim$ 11–15 mm, which is in close agreement with the experimentally measured vortex diameter $\sim$ 12–17 mm. The dimension of the dust cloud in this discharge condition is $L \sim 55$ mm, hence the formation of multiple ($n = L/D_0 \sim 3$) vortices could possibly be in the dust cloud. In accordance with the above theoretical estimation, we have also observed three vortices in our experiments. As discussed in section 5.4, the length of the dust cloud reduces with lowering the rf power by losing the edge particles. The length of the dust cloud reduces from $\sim$ 55 mm to $\sim$ 25 mm at P = 5.1 W. In addition to that, the average vortex size along the axis of the dust cloud increases to $\sim$ 16–19 mm (see Fig. 5.2(c)). For this discharge condition, the characteristic size (D_0) of the vortex is estimated as $\sim$ 11–16 mm for $\eta_k \approx$ 0.02–0.04 $cm^2 s^{-1}$, $\omega^* \sim 30\ s^{-1}$ and $\Gamma^* \sim 60$, which agrees well with the observed average size of the vortex. Therefore; in this case, the expected vortex structures are observed to be $n = L/D_0 \sim 1$, which is clearly seen in the experiment. The estimated vortex structures in an extended dust cloud is found to be similar to the experimental observed vortices. It concludes that multiple vortices could be formed in a large aspect ratio (extended) dust cloud if the driving source (i.e., charge gradient) is present in the dust system. It is also observed that the size of vortex structure depends on various dusty plasma parameters such the dust-dust interactions (coupling constant and viscosity), gradient of the particles charge, shape and size of the dust cloud, dust number density, and dust–neutral friction frequency. To incorporate these effects, further studies on the multiplicity of vortex structures are required and will be presented in future.

5.5 Summary and conclusion

The dynamics of dust grains in an extended dust column in the background of inhomogeneous plasma at a wide range of discharge parameters is studied. At a particular discharge condition, multiple co–rotating (anti–clockwise) vortices are observed in an extended dusty plasma medium in the X–Y plane near the centre of source section. The transition from multiple vortices to a single vortex is observed when input rf power is lowered. The rotation speed is found to be non–uniform throughout the vortex structure and increases towards the boundary of the vortex structure. The angular frequency of the rotation based on the model provided by Vaulina *et al.* [27, 222] is found to be in close agreement with the experimentally observed values, which essentially indicates that the charge gradient of dust particles orthogonal to the ion drag is a possible mechanism to drive the vortex flow.

In this model, they have pointed out that for the occurrence of these self–excited vortex motion, a small charge gradient in the dust cloud ($\sim 1\%$) is an effective source for conversion of potential energy to kinetic energy of dust grains. Inhomogeneity in the plasma parameters (n and T_e) along the dust cloud length is a major cause for the charge gradient of dust particles. It is observed that a vortex structure has a characteristic size in the dusty plasma medium, which mainly depends on its properties (*i.e.* dust–dust interaction, dust–neutral interaction, dust density etc.). The preliminary quantitative analysis shows that the multiple co–rotating vortices could possibly be formed in an extended dusty plasma with inhomogeneous plasma background when the vortex size is smaller than the dust cloud dimension. The experimental results on the multiple vortex formation are compared with a theoretical model and are found to be in close agreement.

This Chapter discusses the origin of co–rotating vortices in an extended dust cloud with inhomogeneous plasma environment, which is observed first time in dusty plasma medium. The detailed nature and reason for multiple vortices and its size dependence are still under investigation through further experiments. In this experimental configuration, dust cloud lies in the X–Y plane; therefore, direct measurement of plasma parameters along the dust cloud axis is difficult. To overcome this situation and to get large aspect ratio dust cloud (or large volume dusty plasma), a modified experimental configuration using inductively coupled discharge has been proposed for the future work. Brief introduction about the modified experimental configuration, potential well to confine particles and some preliminary observations of the future work is presented in next Chapter.

6

Summary and Future Scope

In this Chapter, a brief summary and conclusions of the work carried out in this thesis is provided in Sec. 6.1 and future directions to perform the experiments on the low pressure large volume dusty plasma is presented in Sec. 6.2.

6.1 Summary and conclusion

This thesis presents the experimental configurations to produce large volume dusty plasma at low argon pressure (≤ 0.07 mbar) and to study the role of ambient plasma environment on the collective modes (e.g. waves and vortices) of dusty plasma medium. At first, a DC discharge (cathode trap) configuration is employed to create dusty plasma using poly–dispersive (kaolin) dust particles. A bowl shaped 3D dusty plasma is formed at argon pressure of 0.07 mbar. The study of dust acoustic waves and its propagation characteristics in presence of an external potential perturbation is investigated in this dusty plasma. Working at even low pressure (< 0.05 mbar) in DC discharge configuration makes dust medium highly unstable; therefore, a novel configuration using inductively coupled plasma (diffused edge trap) is investigated to produce a large volume dusty plasma at low pressure (0.05 to 0.01 mbar). A unique technique using the DC plasma source is also used to inject the dust grains into the electrostatic trap. The collective dynamics of dust grains, which results in the formation of multiple co–rotating vortex structures, is studied in an extended 2D dust cloud at wide range of discharge parameters. The underlying physics causing the modification in the propagation characteristics of the dust acoustic wave with an external potential perturbation, particles transport and confinement in a potential well of the diffused plasma, and origin of multiple co–rotating vortices in large volume dusty plasma is thoroughly investigated.

The dusty plasma in laboratory is produced using two different discharge (DC and RF) configurations. In the DC discharge configuration, strong electric field present in the cathode sheath is exploited to levitate the negatively charged dust particles in a bowl shaped (3D) dust cloud. In the case of inductively coupled discharge configuration, dust particles are confined in a potential well created by an inductively coupled diffused plasma. The levitation or confinement of these particles in both discharge configurations is the result of the action of various forces such as gravitational force, the electrostatic force due to the electric field, the repulsive Coulomb force among the like charged dust particles, ion drag force due to the streaming of ions relative to the dust particles, and friction force due to collision with the neutrals. It is well known that the dynamics of dust grains is self–consistently linked to the ambient plasma environment. Therefore, to track the dynamical changes of the dust grain medium, plasma parameters are measured using active diagnostics such as a single Langmuir probe, double probe and emissive probe in the absence of dust particles. For imaging the self–oscillatory motion of dust grains, a diode pumped solid state (DPSS) red laser, cylindrical lens, CCD/CMOS camera, zoom lens, and high performance computer are utilized. The wavelength, frequency and phase velocity of the low frequency oscillations are obtained from the video images by using imageJ software and MATLAB based software. In the case of vortex motion, Particle Image Velocimetry (PIV) analysis [21] is conducted on the still video images to measure the magnitude as well as the direction of the velocity vector (or flowing particles) in a given vertical plane of the dust cloud. The angular velocity of a rotating particle is also measured using the PIV analysis technique. The dynamics of dust grain medium at low pressure is presented in the following parts of this dissertation:

In the first part of this thesis, we have studied the excitation of dust acoustic waves and its propagation characteristics in presence of an external electric perturbation (or floating object). To produce dusty plasma, DC glow discharge is initiated by applying a voltage difference between the cathode and two anodes (both are grounded) at an argon gas pressure of 0.07 mbar. The two anode configuration demands minimum voltage to breakdown the argon gas. At first, plasma is formed in between the cathode and lower anode at about 320 V and later it strikes between the cathode and upper anode. As plasma density crosses a critical limit, dust particles on the cathode surface (sprinkled on the surface before the production of plasma) get negatively charged and are levitated at the plasma–sheath boundary. These particles are horizontally confined due to an inward component of the radial electrostatic field of the sheath formed around the ring at its periphery balancing the repulsive Coulomb force among the charged particles. The vertical levitation of the dust particle is primarily a consequence of the balance between the upward electrostatic force, F_E and the downward gravitational force, F_g. The role of other forces in an equilibrium condition is found to be smaller at least by an order of magnitude as compared to the F_E and F_g . The levitated dust particles are organized into a three-dimensional (bowl shaped) cloud at ∼40 mm above the cathode at the discharge voltage of 340 V and argon pressure of 0.07 mbar. At the discharge voltage beyond 350 V, dust particles start to oscillate about its equilibrium position and these oscillations are seen to propagate towards the cathode. At this discharge condition, the streaming ions trigger these longitudinal dust cloud oscillations [22, 23], which consist of the alternating compression and rarefaction regions. Theses longitudinal low-frequency oscillations are classified as dust acoustic waves (DAWs) [24]. The measured wavelength and phase velocity are 1.5 – 2.5 mm and 2 – 3 cm/sec, respectively; while the frequency is lying in the range of 10 – 15 Hz.

After the characterization of DAWs, experiments are performed to study the modification of its propagation characteristics in the presence of an external electric perturbation, which is applied using a floating cylindrical rod of radius (r) larger than the dust Debye length (λ_D). The floating rod is introduced into the plasma perpendicular to the cathode plane (vertically aligned) and in the plane of cathode (horizontally aligned). In the presence of a vertically aligned floating rod, the DAWs are disappeared in the perturbed region at discharge voltage $V_d \sim 380$ – 400 V, whereas at higher discharge voltage (> 420 V); the DAWs are observed to propagate obliquely in the vertical plane. In the radial plane of a rod (horizontal plane), circular DAWs are found to originate at the outer edge of the perturbed region and propagate towards the rod surface. Interaction of the horizontally aligned rod provides detailed information on the DAWs propagation characteristics with the discharge parameters. In the case of horizontally aligned rod, it is observed that dust cloud takes various shapes (concave or cone shape) depending on the position of the rod with respect to the levitated dust cloud. In the presence of a floating rod, sheath around it alters the potential contour (or electric field distribution) of the cathode sheath region because of the coupling of the sheaths formed around the cylindrical rod and the cathode [25]. As a result, the dust grains follow the modified equipotential surfaces to get an equilibrium position in the perturbed region. Hence, in the perturbed region; dust grains are lifted up by few mm near the rod. Also, the directional flow of ions through dust cloud changes in the perturbed region, which causes the oblique propagation of DAWs.

In the second part of this thesis, a novel configuration using an inductively coupled diffused plasma to create a large volume dusty plasma at low gas pressure is presented. Plasma is produced by passing the high frequency (13.56 MHz) current through an inductive coil, which is wound around a glass tube (called source section). Plasma is produced in the source section and after that it diffuses into the experimental chamber. This diffused plasma provides an electrostatic confinement to the negatively charged dust grains. For injecting the dust grains into the potential well, a novel technique using the DC discharge plasma is employed. The dust grains are homogeneously sprinkled on the SS disk, which is kept fixed inside the experimental tube about 30 cm away from the source section. A negative DC voltage is applied to this disk to levitate the dust grains at plasma–sheath boundary. Due to the poor confinement, these particles come into the plasma volume and are found to be transported in an ambipolar E–field of diffused plasma. These transported particles are confined in the electrostatic potential well, which is formed due to the diffused plasma (ambipolar E–field) and the charged glass wall (sheath E–field) [26]. These confined particles form a 3–dimensional (3D) dusty plasma and remains confined for longer time. One unique aspect of this device is that volume of the dust medium can be controlled precisely by changing the DC bias on the disc. In this experimental configuration, an equilibrium dust grain medium is possible at low pressure ($\sim$0.01 mbar) and low rf power (3–4 W). The ambient plasma parameters (n, T_e and V_p) are measured to estimate the forces acting on the charged particle to understand the transport and trapping of dust grains in a potential well of the diffused plasma.

In the third part of this thesis, we have investigated self–oscillatory motion of the dust grains in an extended dust cloud with inhomogeneous plasma environment. It is observed that dust particles show the acoustic vibrations at the higher rf power (P > 8 W) and particles set up into rotational motion below this power. The multiple co–rotating (anti–clockwise) vortices are observed in the dust cloud for a particular discharge condition (P = 7.5 W and p = 0.04 mbar). When rf power is lowered, transition from multiple to single dust vortex is observed. The PIV analysis is conducted on the still images to get the velocity distribution of particles in the vortex structures. It is observed that particles have non–uniform velocity distribution in a vortex structure. The occurrence of these vortices is explained on the basis of the charge gradient in the dust column orthogonal to the ion drag force [27]. This charge gradient is a consequence of the plasma inhomogeneity along the dust cloud length. The vortex structure has a characteristic size in the dusty plasma so that multiple vortices could be formed in an extended dust cloud in inhomogeneous plasma background [228]. The experimental results on the vortex motion of particles are compared to an available theoretical model [27, 28] and found to be in close agreement.

In conclusion, the work performed in this thesis gives insight in several newly observed phenomena in dusty plasma such as oblique propagating dust acoustic waves, transport and trapping of negatively charged dust grains in a potential well of the diffused plasma, and multiple co–rotating vortex structures.

6.2 Future work

- **Collective modes in a large volume dusty plasma**

The main task of the thesis work was to study the collective phenomena in a large volume dusty plasma at low pressure. We have designed and built a dusty device to perform the dusty plasma experiments with various particles trapping configurations. In Chapter 3, a DC glow discharge configuration (cathode trap) has been discussed to perform the dusty plasma experiments at low pressure. Chapter 4 discusses an inductively coupled discharge configuration (diffused edge trap) for the formation of a large volume dusty plasma at low pressure. The dynamics of dust grains in an extended dusty plasma (in 2D plane) has been presented in Chapter 5. The multiple co–rotating vortex structures are observed in an extended dust cloud with inhomogeneous plasma background. The preliminary quantitative analysis shows that the charge gradient (β) of dust particles orthogonal to the ion

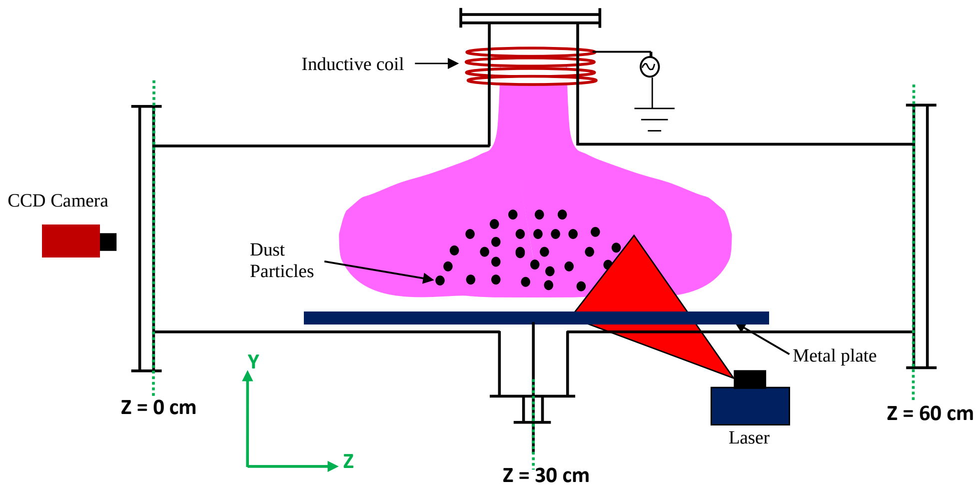

Figure 6.1: A schematic of the experimental setup to produce large aspect ratio (or large volume) dusty plasma at low pressure.

drag force is possible source to drive the vortex motion. These results essentially suggest that large aspect ratio dusty plasma can accommodate multiple vortex structures if there exist a possible source to drive the vortex motion. The observed results in this thesis motivates to further study the large volume or large aspect ratio dusty plasma at a wide range of discharge parameters. To get a large volume dusty plasma which can easily be diagnosed, a modified configuration using the inductively coupled discharge is proposed. The schematic of the modified experimental configuration is depicted in Fig. 6.1. In this configuration, inductive coil is wound on the radial port (P6) of the experimental chamber and a SS metal plate is placed near the inner bottom wall of the chamber. The use of this floating plate is to modify the shape of the edge of diffused plasma. In this modified configuration, the plasma is formed in source section (P6) and diffuses in the experimental chamber. The radial port (P4) is used to hold the dust reservoir. The dust particles are introduced into the electrostatic trap using a secondary DC plasma source. The dust grains are found to be confined in a potential well created by the diffused plasma.

To get the shape of potential well, plasma potential is measured along the X, Y and Z axis at a given discharge parameters. Fig. 6.2(a) shows the potential well to confine the particles axially. The E-field component along the Y direction holds the grains against gravity (see Fig. 6.2(b)). The potential well to confine the particles in the X direction is shown in Fig. 6.2(c). The mechanism for particle

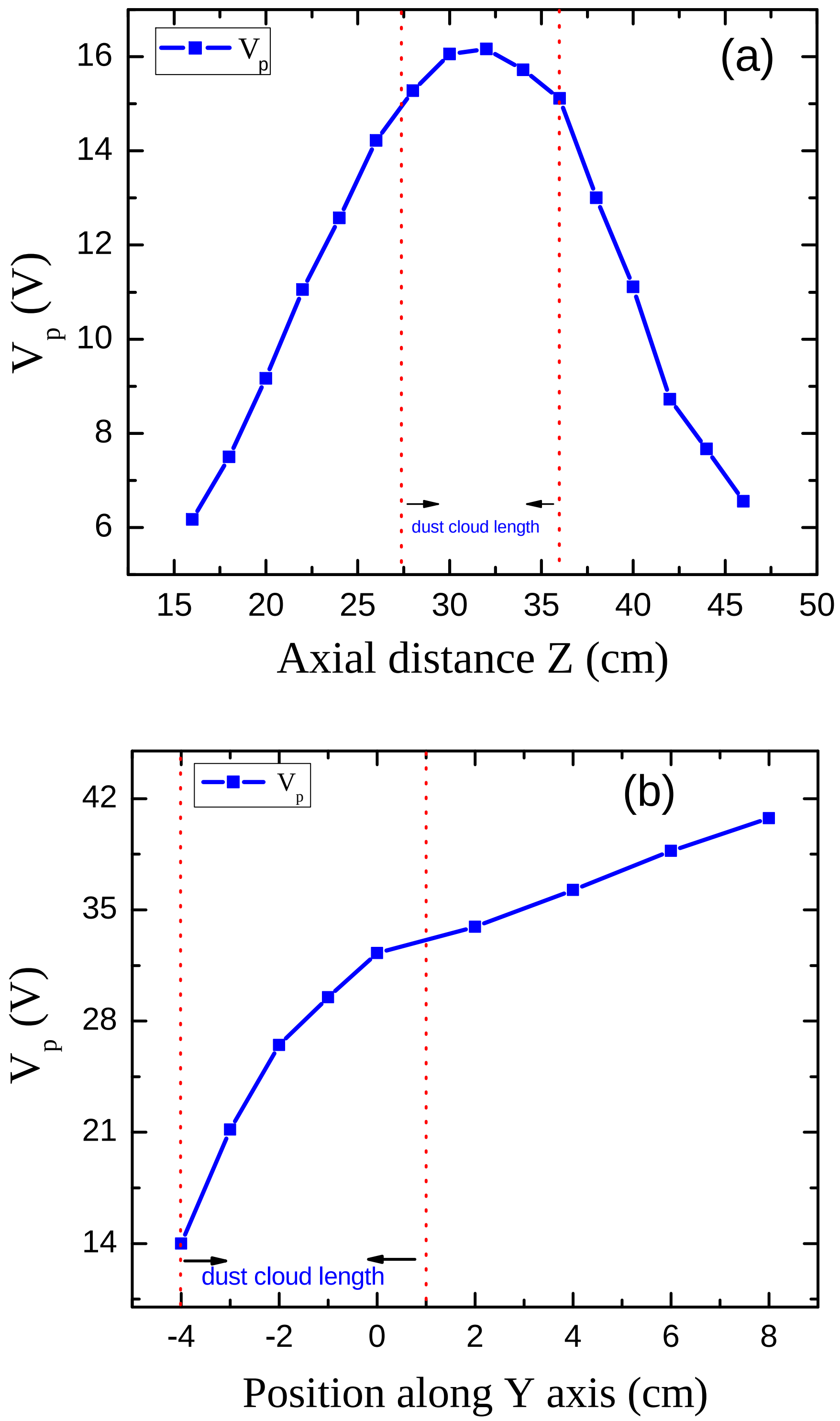

Vp
(a)
dust cloud length
16
14
12
10
8
6
Vp (V)
15
20
25
30
35
40
45
50
Axial distance Z (cm)
Vp
(b)
dust cloud length
42
35
28
21
14
Vp (V)
-4
-2
0
2
4
6
8
Position along Y axis (cm)

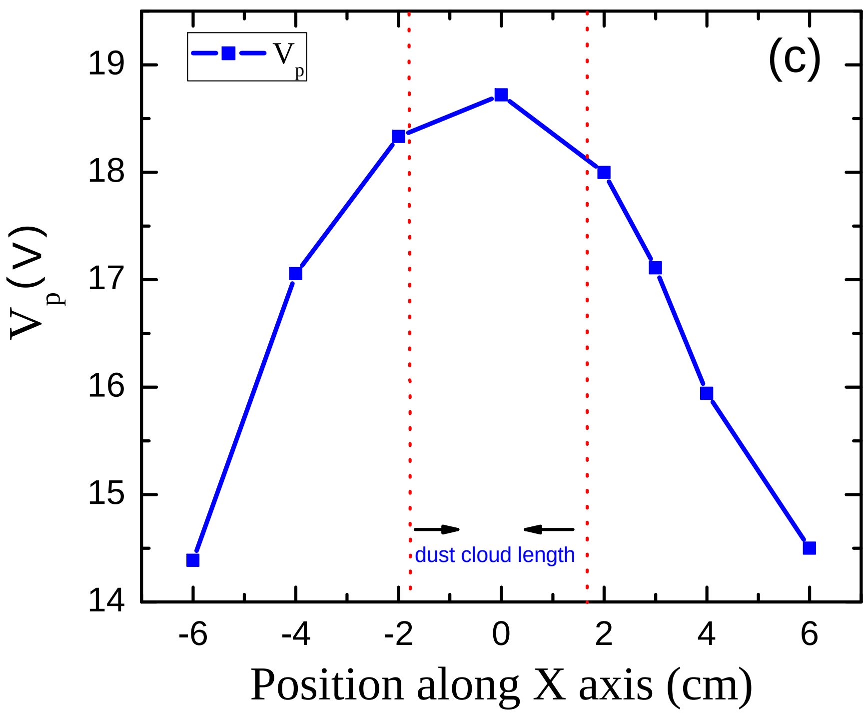

Figure 6.2: Plasma potential profiles: (a) along Z–axis for Y ≈ -4 cm and X ≈ 0 cm. (b) along Y–axis for Z ≈ 30 cm and X ≈ 0 cm. (c) along X–axis for Y ≈ -3 cm and Z ≈ 30 cm. All the measurements are taken in absence of dust particles at P = 9 W and p = 0.04 mbar. The errors in the measured value of plasma potential are ± 2 V

.

Figure 6.3: A video image of the dust cloud in the Y–Z plane at X ∼ 0 cm. The experiment is performed with kaolin particles at P = 8 W and p = 0.06 mbar.

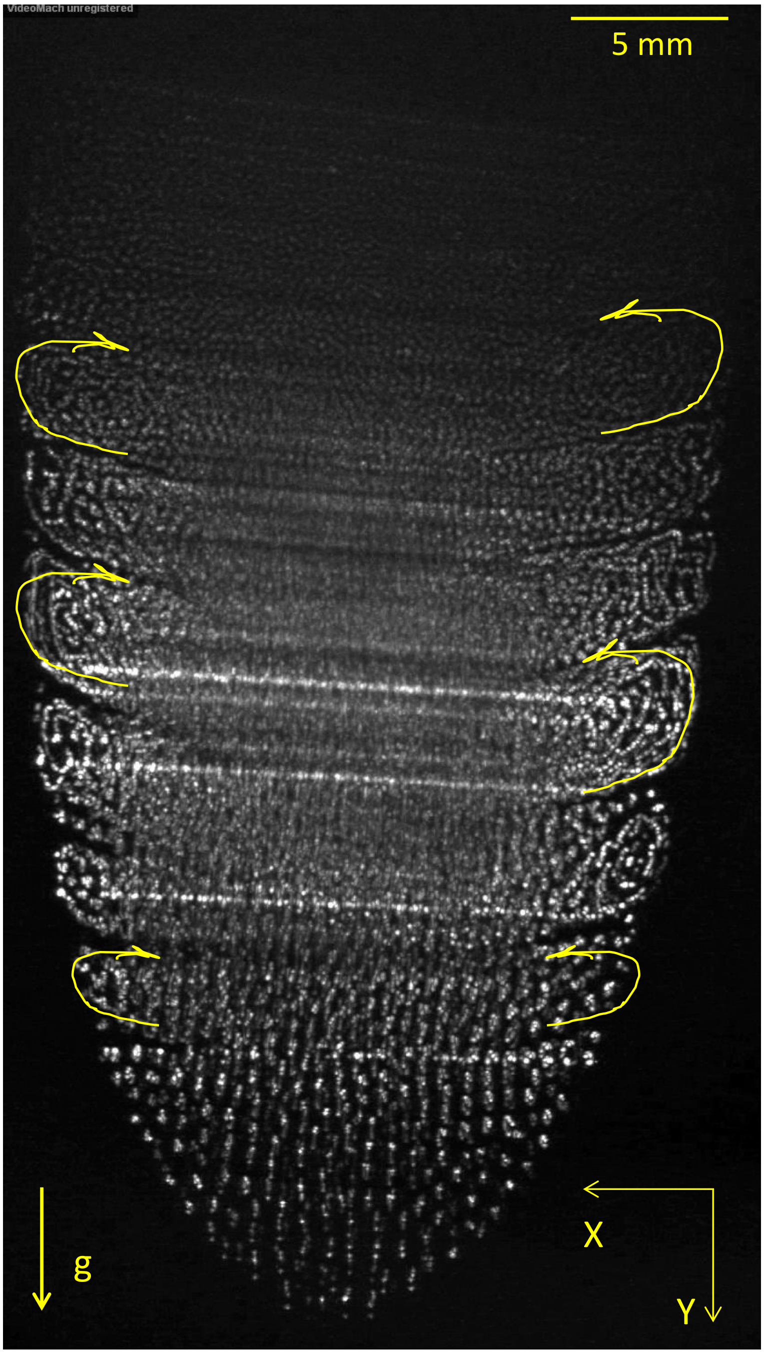

Figure 6.4: A video image of the dust cloud in the X–Y plane at Z $\sim$ 30 cm. Experiment is performed with kaolin particles at P = 6 W and p = 0.03 mbar. The yellow curved lines with an arrow indicate the direction of dust grain rotation.

confinement is similar to that has been discussed in Chapter 4.

In this modified configuration, a symmetric (along the Z axis) large volume dusty plasma can be produced using the poly-dispersive dust particles. A video image of the dust cloud in the Y–Z plane is shown in Fig. 6.3, which shows signature of transverse nature of the dust acoustic waves. An another video image of the dust cloud after superposition of five consecutive frames in the X–Y plane is shown in Fig. 6.4, which shows a series of co–rotating vortex structures near the edge of the confined dust cloud. The center region of dust cloud is observed to have wave like structures (not clearly seen in Figure). These preliminary observations provide the future directions to carry the research work in large volume dusty plasma. The future works are listed below:

1. The origin of the series of co–rotating vortices (see Fig. 6.4) and its size dependence on dust as well as the plasma parameters can be studied. The dust cloud is symmetric about the Y- axis for a given Z value in the modified configuration; therefore, it can be considered in a plane of the cylindrical co-ordinate system for solving the equation of motion. The wave like structures in the central region of dust cloud and vortex at the edge of cloud need to be understood using the available theoretical model [27].

2. It is observed that particles flow is opposite at an interface of two co–rotating vortex structures. These opposite flow can induce K–H type instability at an interface of opposite flowing medium at certain discharge or dusty plasma parameters. Such type of instabilities can also be investigated.

3. It has been discussed in Chapter 5 that vortex structure probably has 3D characteristics. We can reconstruct the three dimensional structure/flow from several parallel planes of the motion using ImageJ (PIV plugin) or MATLAB based software. To get the images in different X–Y planes, precise shifting of optical system (laser and cylindrical lens) is required and that can be done using a motorized shifting.

4. Study of the longitudinal dust acoustic modes (merging and splitting of wave fronts) in a large volume (or in an extended dust cloud) dusty plasma (see Fig. 4.10) need to be explored. The signature of the transverse dust acoustic

modes (see Fig. 6.3) in an extended strongly coupled dusty plasma is also an interesting problem and can be studied in future.

5. Chapter 4 discusses the transport of dust grains in an ambipolar E–field of diffused plasma. The motion of charged particles can be traced with time in the ambipolar E–field. The OML theory is applicable in the diffused plasma where quasi-neutrality condition is satisfied; therefore, plasma parameters can be measured using the electrostatic probes. These plasma parameters can be used to solve the equation of motion of a transported particle in the diffused plasma to get the charge on dust particle. In addition to that dynamics of the flowing particles can be used to understand the transport properties of the dust grain medium.

- **Transient response of low pressure dusty plasma**

It is observed that an equilibrium dusty plasma (small volume) can be created using the diffused edge trap (Fig. 6.1) at low pressure (< 0.01 mbar). Chapter 3 discusses the effect of a time-independent electrostatic perturbation on the dust acoustic modes. In recent years, dust grain dynamics under the action of transient positive pulses of high voltage (1–20 kV) and nanosecond duration have been studied by various researchers [229–231].

Recently, Choudhary *et al.* [232] have reported the long–time evolution of low pressure (at p = 0.001 mbar) plasma after the application of transient high voltage positive pulses. They have observed the electron heating as well as the presence of a beam component during the evolution process. They have also reported the effect of pulse width and amplitude of pulses on the evolution time of low pressure plasma. Fig. 6.5 represents the transient electron energy distribution function for pulse width of 10 μs and amplitude of 1020 V, which indicates the presence of a beam component along with the bulk electron group. It is well known that dust grain dynamics is self–consistently associated to background plasma parameters. It has been experimentally verified that charge on the dust grain surface is determined by the energetic electrons in the plasma [233]. In the low pressure dusty plasma, it is expected that dust grain dynamics may get altered during the relaxation process (or after removal of the transient positive pulses). Also, dust grain heating is possible if the inter–particle potential (or charge on the dust) is time varying [234],

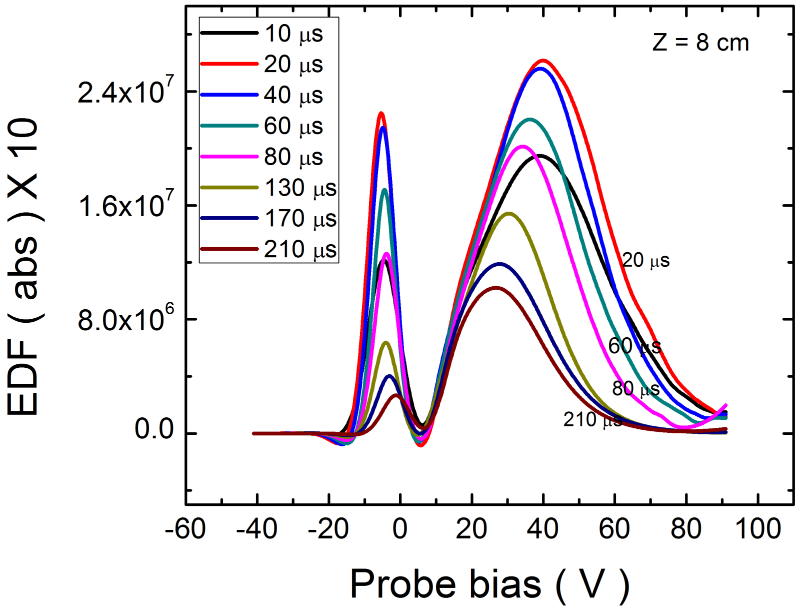

Figure 6.5: Transient electron energy distribution function (EEDF) for pulse width of 10 μs and amplitude $U_p = 1020$ V at 8 cm far away from an exciter. The argon gas pressure was 0.001 mbar.

which can also induce some instabilities in the dust grain medium. Moreover, after application of transient pulses; mechanism of pulse-induced charge variations may also trigger the oscillation of micro particles and instabilities in the dust cloud. All these considerations motivate to study the dust grain dynamics with positive pulses ($\tau_p \gg \tau_d$) of higher amplitude (> 1 kV) in future.

Bibliography

[1] A. Barkan, R. L. Merlino, and N. D'Angelo. Laboratory observation of the dust-acoustic wave mode. *Phys. Plasmas*, 2:3563–3565, 1995.

[2] C. Thompson, A. Barkan, N. D'Angelo, and R. L. Merlino. Dust acoustic waves in a direct current glow discharge. *Phys. Plasmas*, 4:2331–2335, 1997.

[3] M. C. Chang and I. Tsai, Y. Y.and Lin. Observation of 3d defect mediated dust acoustic wave turbulence with fluctuating defects and amplitude hole filaments. *Phys. Plasmas*, 20:083703, 2013.

[4] M. Schwabe, M. Rubin-Zuzic, S. Zhdanov, H. M. Thomas, and G. E. Morfill. Highly resolved self-excited density waves in a complex plasma. *Phys. Rev. Lett.*, 99:095002, 2007.

[5] P. Bandyopadhyay, G. Prasad, A. Sen, and P. K. Kaw. Experimental study of nonlinear dust acoustic solitary waves in a dusty plasma. *Phys. Rev. Lett.*, 101:065006, 2008.

[6] J. Heinrich, S.-H. Kim, and R. L. Merlino. Laboratory observations of self-excited dust acoustic shocks. *Phys. Rev. Lett.*, 103:115002, 2009.

[7] A. Homann, A. Melzer, S. Peters, R. Madani, and A. Piel. Laser-excited dust lattice waves in plasma crystals. *Physics Letters A*, 242:173 – 180, 1998.

[8] Tim Bockwoldt, Oliver Arp, Kristoffer Ole Menzel, and Alexander Piel. On the origin of dust vortices in complex plasmas under microgravity conditions. *Phys. Plasmas*, 21:103703, 2014.

[9] O. S. Vaulina, A. A. Samarian, O. F. Petrov, B. W. James, and V. E. Fortov. Self-excited motions in dusty plasmas with gradient of charge of macroparticles. *New Journal of Physics*, 5:82, 2003.

[10] M. M. Vasiliev, S. N. Antipov, and O. F. Petrov. Large–scale vortices in dc glow discharge dusty plasmas. *Journal of Physics A: Mathematical and General*, 39:4539, 2006.

[11] Kil-Byoung Chai and Paul M. Bellan. Vortex motion of dust particles due to non-conservative ion drag force in a plasma. *Phys. Plasmas*, 23:023701, 2016.

[12] M. M. Vasil'ev, L. G. D'yachkov, S. N. Antipov, O. F. Petrov, and V. E. Fortov. Dusty plasma structures in magnetic fields in a dc discharge. *JETP Letters*, 86:358–363, 2007.

[13] Manjit Kaur, Sayak Bose, P. K. Chattopadhyay, D. Sharma, J. Ghosh, Y. C. Saxena, and Edward Thomas. Generation of multiple toroidal dust vortices by a non-monotonic density gradient in a direct current glow discharge plasma. *Phys. Plasmas*, 22:093702, 2015.

[14] E. Thomas, Jr., K. Avinash, and R. L. Merlino. Probe induced voids in a dusty plasma. *Phys. Plasmas*, 11:1770–1774, 2004.

[15] D. A. Law, W. H. Steel, B. M. Annaratone, and J. E. Allen. Probe-induced particle circulation in a plasma crystal. *Phys. Rev. Lett.*, 80:4189–4192, 1998.

[16] S.-H. Kim, J. R. Heinrich, and R. L. Merlino. Diffraction of dust acoustic waves by a circular cylinder. *Phys. Plasmas*, 15:090701, 2008.

[17] A.K Agarwal and G Prasad. Spontaneous dust mass rotation in an unmagnetized dusty plasma. *Physics Letters A*, 309:103–108, 2003.

[18] Edward Thomas and Michael Watson. First experiments in the dusty plasma experiment device. *Phys. Plasmas*, 6:4111–4117, 1999.

[19] Y. Nakamura and H. Bailung. A dusty double plasma device. *Rev. Sci. Instrum.*, 70:2345–2348, 1999.

[20] V. E. Fortov, A. D. Usachev, A. V. Zobnin, V. I. Molotkov, and O. F. Petrov. Dust-acoustic wave instability at the diffuse edge of radio frequency inductive low-pressure gas discharge plasma. *Phys. Plasmas*, 10:1199–1208, 2003.

[21] Jeremiah D. Williams. Application of particle image velocimetry to dusty plasma systems. *J. Plasma Phys.*, 82:615820302, 2016.

[22] R. L. Merlino. Dust-acoustic waves driven by an ion-dust streaming instability in laboratory discharge dusty plasma experiments. *Phys. Plasmas*, 16:124501, 2009.

[23] V. E. Fortov, A. G. Khrapak, S. A. Khrapak, V. I. Molotkov, A. P. Nefedov, O. F. Petrov, and V. M. Torchinsky. Mechanism of dust-acoustic instability in a direct current glow discharge plasma. *Phys. Plasmas*, 7:1374–1380, 2000.

[24] Mangilal Choudhary, S. Mukherjee, and P. Bandyopadhyay. Propagation characteristics of dust–acoustic waves in presence of a floating cylindrical object in the dc discharge plasma. *Physics. Plasmas*, 23:083705, 2016.

[25] E. V. Barnat and G. A. Hebner. Electric field profiles around an electrical probe immersed in a plasma. *J. Appl. Phys.*, 101:013306, 2007.

[26] Mangilal Choudhary, S. Mukherjee, and P. Bandyopadhyay. Transport and trapping of dust particles in a potential well created by inductively coupled diffused plasmas. *Rev. Sci. Instrum.*, 87:053505, 2016.

[27] O. S. Vaulina, A. P. Nefedov, O. F. Petrov, and V. E. Fortov. Instability of plasma-dust systems with a macroparticle charge gradient. *Journal of Experimental and Theoretical Physics*, 91:1147–1162, 2000.

[28] O. S. Vaulina, O. F. Petrov, V. E. Fortov, G. E. Morfill, H. M. Thomas, Yu. P. Semenov, A. I. Ivanov, S. K. Krikalev, and Yu. P. Gidzenko. Analysis of dust vortex dynamics in gas discharge plasma. *Physica Scripta*, T107:224, 2004.

[29] Lewi Tonks and Irving Langmuir. Oscillations in ionized gases. *Phys. Rev.*, 33:195–210, 1929.

[30] Anthony L. Peratt. *Physics of the Plasma Universe*. Springer- Verlag, 1992.

[31] Wolfgang Baumjohann and Rudolf A. Treumann. *Basic Space Plasma Physics*. Imperial College Press , London, 1996.

[32] B. A. Smith et al. Encounter with saturn: Voyager 1 imaging science results. *Science*, 212:163, 1981.

[33] B. A. Smith et al. A new look at the saturn system: The voyager 2 images. *Science*, 215:504–537, 1982.

[34] C. K. Goertz and G. Morfill. A model for the formation of spokes in saturn's ring. *Icarus*, 53:219–229, 1983.

[35] M. Horãnyi, T. W. Hartquist, O. Havnes, D. A. Mendis, and G. E. Morfill. Dusty plasma effects in saturn's magnetosphere. *Rev. Geophys.*, 42:RG4002, 2004.

[36] C.K. Goertz. Formation of saturn's spokes. *Advances in Space Research*, 4:137–141, 1984.

[37] Eberhard Grün, Gregor E. Morfill, Richard J. Terrile, Torrence V. Johnson, and Gerhard Schwehm. The evolution of spokes in saturn's b ring. *Icarus*, 54:227–252, 1983.

[38] G. E. Morfill and H. M. Thomas. Spoke formation under moving plasma clouds-the goertz morfill model revisited. *Icarus*, 179:539–542, 2005.

[39] G. E. Morfill, E. Grün, C. K. Goertz, and T. V. Johnson. On the evolution of saturn's spokes: Theory. *Icarus*, 53:230–235, 1983.

[40] Jay Roderick Hill and D. A. Mendis. On the braids and spokes in saturn's ring system. *The moon and the planets*, 24:431–436, 1981.

[41] R. Greenberg and A. Brahic. Planetary rings. *IAU Colloq. 75: Planetary Rings*, 1984.

[42] Ellis D. Miner, Randii R. Wessen, and Jeffrey N. Cuzzi. *Planetary Ring Systems*. Springer, Praxis, chichester, UK, 2003.

[43] P. K. Shukla and A. A. Mamun. *Introduction to Dusty Plasma Physics*. series in plasma physics. IOP, Bristol, 2002.

[44] Frank Verheest. *Waves in Dusty Space Plasmas*. Springer Science and Business Media, 2012.

[45] Lyman Spitzer Jr. *Physical Processes in the Interstellar Medium*. Wiley VCH, 1998.

[46] Ingrid Mann, Nicole Meyer-Vernet, and Andrzej Czechowski. *Nanodust in the Solar System: Discoveries and Interpretations*. Springer-Verlag Berlin Heidelberg, 2012.

[47] Backhouse T. W. *Meteorol. Mag.*, 20:133, 1985.

[48] Michael Gadsden and Wilfried Schröder. *Noctilucent clouds*. Springer–Verlag, Berlin Heidelberg, 1989.

[49] I. Mann et al. Dusty plasma effects in near earth space and interplanetary medium. *Space Sci. Rev.*, 161:1–47, 2011.

[50] E. Grün et al. Discovery of jovian dust streams and interstellar grains by the ulysses spacecraft. *Nature*, 362:428–430, 1993.

[51] C. K. Goertz. Dusty plasmas in the solar system. *Reviews of Geophysics*, 27:271–292, 1989.

[52] Gary S. Selwyn, John E. Heidenreich, and Kurt L. Haller. Rastered laser light scattering studies during plasma processing: Particle contamination trapping phenomena. *J. Vac. Sci. Technol. A*, 9:2817–2824, 1991.

[53] Y. Watanabe. Dust phenomena in processing plasmas. *Plasma Phys. Control. Fusion*, 39(5A):A59–A72, 1997.

[54] Laïfa Boufendi and André Bouchoule. Industrial developments of scientific insights in dusty plasmas. *Plasma Sources Sci. Technol.*, 11:A211, 2002.

[55] André Bouchoule. *Dusty Plasmas: Physics, Chemistry, and Technological Impact in Plasma Processing*. Willey, 1999.

[56] Michael A. Lieberman and Alan J. Lichtenberg. *Principles of Plasma Discharges and Materials Processing*. John Wiley and Sons, 2005.

[57] Pere Roca i Cabarrocas, Patrick Gay, and Aomar Hadjadj. Experimental evidence for nanoparticle deposition in continuous argon-silane plasmas: Effects of silicon nanoparticles on film properties. *J. Vac. Sci. Technol.*, 14:655–659, 1996.

[58] J. Winter. Dust in fusion devices - experimental evidence, possible sources and consequences. *Plasma Phys. Control. Fusion*, 40:1201, 1998.

[59] V. Tsytovich and J. Winter. The on the role of a dust in fusion devices directory. *Phys. Usp.*, 41:815–822, 1998.

[60] J. Winter and J. Gebauer. Dust in magnetic confinement fusion devices and its impact on plasma operation. *Journal of Nuclear Materials*, 266–269:228–233, 1999.

[61] S. I. Krasheninnikov, Y. Tomita, R. D. Smirnov, and R. K. Janev. On dust dynamics in tokamak edge plasmas. *Phys. Plasmas*, 11:3141–3150, 2004.

[62] J. P. Sharpe, D. A. Petti, and H. W. Bartels. A review of dust in fusion devices: Implications for safety and operational performance. *Fusion Engineering and Design*, 63–64:153–163, 2002.

[63] J. Winter. Dust: A new challenge in nuclear fusion research? *Phys. Plasmas*, 7:3862–3866, 2000.

[64] S. I. Krasheninnikov, R. D. Smirnov, and D. L. Rudakov. Dust in magnetic fusion devices. *Plasma Phys. Control. Fusion*, 53:083001, 2011.

[65] Jin Jwang Wu and Robert J. Miller. Measurements of charge on submicron particles generated in a sputtering process. *J. Appl. Physics*, 67:1051–1054, 1990.

[66] B. Walch, M. Horanyi, and S. Robertson. Measurement of the charging of individual dust grains in a plasma. *IEEE Transactions on Plasma Science*, 22:97–102, 1994.

[67] O. Havnes. Charges on dust particles. *Adv. Space. Res.*, 4:75–83, 1984.

[68] J. Goree. Charging of particles in a plasma. *Plasma Sources Sci. Technol.*, 3:400–406, 1994.

[69] A. Barkan, N. D'Angelo, and R. L. Merlino. Charging of dust grains in a plasma. *Phys. Rev. Lett.*, 73:3093–3096, 1994.

[70] M. R. Jana, A. Sen, and P. K. Kaw. Collective effects due to charge-fluctuation dynamics in a dusty plasma. *Phys. Rev. E*, 48:3930–3933, 1993.

[71] P. K. Shukla. A survey of dusty plasma physics. *Phys. Plasmas*, 8:1791–1803, 2001.

[72] H. Ikezi. Coulomb solid of small particles in plasmas. *Phys. Fluids*, 29:1764–1766, 1986.

[73] J. H. Chu and Lin I. Direct observation of coulomb crystals and liquids in strongly coupled rf dusty plasmas. *Phys. Rev. Lett.*, 72:4009–4012, 1994.

[74] Vladimir E. Fortov, Vladimir I. Molotkov, Anatoli P. Nefedov, and Oleg F. Petrov. Liquid- and crystallike structures in strongly coupled dusty plasmas. *Phys. Plasmas*, 6:1759–1768, 1999.

[75] A. P. Nefedov, Oleg. F. Petrov, and Vladimir E. Fortov. Quasicrystalline structures in strongly coupled dusty plasma. *Physics-Uspekhi*, 40(11):1163, 1997.

[76] A. P. Nefedov, O. F. Petrov, V. I. Molotkov, and V. E. Fortov. Formation of liquidlike and crystalline structures in dusty plasmas. *JETP Letters*, 72:218–226, 2000.

[77] H. Thomas, G. E. Morfill, V. Demmel, J. Goree, B. Feuerbacher, and D. Möhlmann. Plasma crystal: Coulomb crystallization in a dusty plasma. *Phys. Rev. Lett.*, 73:652–655, 1994.

[78] J. H. Chu and Lin I. Coulomb lattice in a weakly ionized colloidal plasma. *Physica A*, 205:183–190, 1994.

[79] H. Thomas and G. E Morfill. Melting dynamics of a plasma crystal. *Nature*, 379:806–809, 1996.

[80] V.E. Fortov, A.V. Ivlev, S.A. Khrapak, A.G. Khrapak, and G.E. Morfill. Complex (dusty) plasmas: Current status, open issues, perspectives. *Physics Reports*, 421:1–103, 2005.

[81] Hubertus M. Thomas and Gregor E. Morfill. Solid/liquid/gaseous phase transitions in plasma crystals. *J. Vac. Sci. Technol. A*, 14:501–505, 1996.

[82] S. Nunomura, J. Goree, S. Hu, X. Wang, A. Bhattacharjee, and K. Avinash. Phonon spectrum in a plasma crystal. *Phys. Rev. Lett.*, 89:035001, 2002.

[83] Bin Liu and J. Goree. Phonons in a one-dimensional yukawa chain: Dusty plasma experiment and model. *Phys. Rev. E*, 71:046410, 2005.

[84] S. Nunomura, D. Samsonov, and J. Goree. Transverse waves in a two-dimensional screened-coulomb crystal (dusty plasma). *Phys. Rev. Lett.*, 84:5141–5144, 2000.

[85] H. M. Mott-Smith and Irving Langmuir. The theory of collectors in gaseous discharges. *Phys. Rev.*, 28:727–763, 1926.

[86] J. E. Allen. Probe theory - the orbital motion approach. *Physica Scripta*, 45:497, 1992.

[87] S. A. Khrapak and G. E. Morfill. An interpolation formula for the ion flux to a small particle in collisional plasmas. *Phys. Plasmas*, 15:114503, 2008.

[88] A. Barkan, N. D'Angelo, and R.L. Merlino. Experiments on ion-acoustic waves in dusty plasmas. *Planet. Space Sci.*, 44:239–242, 1996.

[89] C. K. Goertz and W.-H. Ip. Limitation of electrostatic charging of dust particles in a plasma. *Geophysical Research Letters*, 11:349–352, 1984.

[90] E. C. Whipple, T. G. Northrop, and D. A. Mendis. The electrostatics of a dusty plasma. *Journal of Geophysical Research: Space Physics*, 90:7405–7413, 1985.

[91] Francis F. Chen. *Introduction to plasma physics and controlled fusion.* Springer US, 1984.

[92] Michael S. Barnes, John H. Keller, John C. Forster, James A. O'Neill, and D. Keith Coultas. Transport of dust particles in glow-discharge plasmas. *Phys. Rev. Lett.*, 68:313–316, 1992.

[93] S. A. Khrapak, A. V. Ivlev, G. E. Morfill, and H. M. Thomas. Ion drag force in complex plasmas. *Phys. Rev. E*, 66, 2002.

[94] Paul S. Epstein. On the resistance experienced by spheres in their motion through gases. *Phys. Rev.*, 23:710–733, 1924.

[95] Manjit Kaur, Sayak Bose, P. K. Chattopadhyay, Devendra Sharma, J. Ghosh, and Y. C. Saxena. Observation of dust torus with poloidal rotation in direct current glow discharge plasma. *Phys. Plasmas*, 22:033703, 2015.

[96] N. N. Rao, P. K. Shukla, and M. Y. Yu. Dust-acoustic waves in dusty plasmas. *Planet. Space Sci.*, 38:543–546, 1990.

[97] F. Li, O. Havnes, and F. Melandsø. Longitudinal waves in a dusty plasma. *Planet. Space Sci.*, 42:401–407, 1994.

[98] A. V. Ivlev, D. Samsonov, J. Goree, G. Morfill, and V. E. Fortov. Acoustic modes in a collisional dusty plasma. *Phys. Plasmas*, 6:741–750, 1999.

[99] M. Salimullah and M. Salahuddin. Dust-acoustic waves in a magnetized dusty plasma. *Phys. Plasmas*, 5:828–829, 1998.

[100] Frank Melandsø, Torsten K. Aslaksen, and Ove Havnes. A kinetic model for dust acoustic waves applied to planetary rings. *J. Geophys. Res.*, 98:2156–2202, 1993.

[101] P. K. Shukla. Low-frequency modes in dusty plasmas. *Phys. Scr.*, 45:504, 1992.

[102] N. D'Angelo. Low-frequency electrostatic waves in dusty plasmas. *Planet. Space Sci.*, 38:1143–1146, 1990.

[103] P. K. Kaw and A. Sen. Low frequency modes in strongly coupled dusty plasmas. *Phys. Plasmas*, 5:3552–3559, 1998.

[104] Frank Melandsø. Lattice waves in dust plasma crystals. *Phys. Plasmas*, 3:3890–3901, 1996.

[105] B. Farokhi, P. K. Shukla, N. L. Tsintsadze, and D. D. Tskhakaya. Dust lattice waves in a plasma crystal. *Phys. Plasmas*, 7:814–818, 2000.

[106] V. I. Molotkov, A. P. Nefedov, V. M. Torchinskii, V. E. Fortov, and A. G. Khrapak. Dust acoustic waves in a dc glow-discharge plasma. *Journal of Experimental and Theoretical Physics*, 89:477–480, 1999.

[107] Edward Thomas Jr. Measurements of spatially growing dust acoustic waves in a dc glow discharge plasma. *Phys. Plasmas*, 13:042107, 2006.

[108] V. E. Fortov, O. F. Petrov, V. I. Molotkov, M. Y. Poustylnik, V. M. Torchinsky, A. G. Khrapak, and A. V. Chernyshev. Large-amplitude dust waves

excited by the gas-dynamic impact in a dc glow discharge plasma. *Phys. Rev. E*, 69:016402, 2004.

[109] A. A. Samaryan, A. V. Chernyshev, O. F. Petrov, A. P. Nefedov, and V. E. Fortov. An analysis of acoustic oscillations in dust plasma structures. *Journal of Experimental and Theoretical Physics*, 92:454–461, 2001.

[110] J. Pramanik, B. M. Veeresha, G. Prasad, and P.K. Sen, A.and Kaw. Experimental observation of dust- acoustic wave turbulence. *Physics Letters A*, 312:84 – 90, 2003.

[111] Thomas Trottenberg, Dietmar Block, and Alexander Piel. Dust confinement and dust-acoustic waves in weakly magnetized anodic plasmas. *Phys. Plasmas*, 13:042105, 2006.

[112] J H Chu, Ji-Bin Du, and Lin I. Coulomb solids and low-frequency fluctuations in rf dusty plasmas. *J.l Phys. D: Appl. Phys.*, 27:296, 1994.

[113] T. M. Flanagan and J. Goree. Observation of the spatial growth of self-excited dust-density waves. *Phys. Plasmas*, 17:123702, 2010.

[114] A. V. Zobnin, A. D. Usachev, O. F. Petrov, and V. E. Fortov. Dust-acoustic instability in an inductive gas-discharge plasma. *Journal of Experimental and Theoretical Physics*, 95:429–439, 2002.

[115] B. Farokhi, P. K. Shukla, N. L. Tsintsadze, and D. D. Tskhakaya. Dust lattice waves in a plasma crystal. *Phys. Plasmas*, 7:814–818, 2000.

[116] Bin Liu, J. Goree, V. E. Fortov, A. M. Lipaev, V. I. Molotkov, O. F. Petrov, G. E. Morfill, H. M. Thomas, H. Rothermel, and A. V. Ivlev. Transverse oscillations in a single-layer dusty plasma under microgravity. *Phys. Plasmas*, 16:083703, 2009.

[117] M. Rosenberg. A note on ion–dust streaming instability in a collisional dusty plasma. *J. Plasma Physics*, 67:235–242, 2002.

[118] N. D'Angelo and R. L. Merlino. Current driven dust acoustic instability in a collisional plasma. *Planet. Space Sci.*, 44:1593 –1598, 1996.

[119] A. A. Mamun and P. K. Shukla. Streaming instabilities in a collisional dusty plasma. *Phys. Plasmas*, 7:4412–4417, 2000.

[120] R. K. Varma, P. K. Shukla, and V. Krishan. Electrostatic oscillations in the presence of grain-charge perturbations in dusty plasmas. *Phys. Rev. E*, 47:3612–3616, 1993.

[121] P.K. Shukla and G. Morfill. Ionization instability of dust-acoustic waves in weakly ionized colloidal plasmas. *Physics Letters A*, 216:153–156, 1996.

[122] V. E. Fortov, A. G. Khrapak, S. A. Khrapak, V. I. Molotkov, A. P. Nefedov, O. F. Petrov, and V. M. Torchinsky. Mechanism of dust-acoustic instability in a direct current glow discharge plasma. *Phys. Plasmas*, 7:1374–1380, 2000.

[123] C. O. Thompson, N. D'Angelo, and R. L. Merlino. The interaction of stationary and moving objects with dusty plasmas. *Phys. Plasmas*, 6:1421–1426, 1999.

[124] S. Sarkar, M. Mondal, M. Bose, and S. Mukherjee. Observation of external control and formation of a void in cogenerated dusty plasma. *Plasma Sources Sci. Technol.*, 24:035007, 2015.

[125] M. Klindworth, A. Piel, A. Melzer, U. Konopka, H. Rothermel, K. Tarantik, and G. E. Morfill. Dust-free regions around langmuir probes in complex plasmas under microgravity. *Phys. Rev. Lett.*, 93:195002, 2004.

[126] J. K. Meyer, J. R. Heinrich, S.-H. Kim, and R. L. Merlino. Interaction of a biased cylinder with a flowing dusty plasma. *J. Plasma Physics*, 79:677–682, 2013.

[127] Surabhi Jaiswal, P. Bandyopadhyay, and A. Sen. Experimental observation of precursor solitons in a flowing complex plasma. *Phys. Rev. E*, 93:041201, 2016.

[128] Y. Maemura, S.-C. Yang, and H. Fujiyama. Transport of negatively charged particles by e x b drift in silane plasmas. *Surface and Coatings Technology*, 98:1351–1358, 1998.

[129] U. Konopka, D. Samsonov, A. V. Ivlev, J. Goree, V. Steinberg, and G. E. Morfill. Rigid and differential plasma crystal rotation induced by magnetic fields. *Phys. Rev. E*, 61:1890–1898, 2000.

[130] Noriyoshi Sato, Giichiro Uchida, Toshiro Kaneko, Shinya Shimizu, and Satoru Iizuka. Dynamics of fine particles in magnetized plasmas. *Phys. Plasmas*, 8:1786–1790, 2001.

[131] Predhiman K. Kaw, Kyoji Nishikawa, and Noriyoshi Sato. Rotation in collisional strongly coupled dusty plasmas in a magnetic field. *Phys. Plasmas*, 9:387–390, 2002.

[132] F. Cheung, A. Samarian, and B. James. Angular velocity saturation in planar dust cluster rotation. *Physica Scripta*, T107:229, 2004.

[133] V. Yu Karasev, E. S. Dzlieva, A. Yu. Ivanov, and A. I. Eikhvald. Rotational motion of dusty structures in glow discharge in longitudinal magnetic field. *Phys. Rev. E*, 74:066403, 2006.

[134] E. S. Dzlieva, V. Yu. Karasev, and A. I. Éĭkhval'd. The onset of rotational motion of dusty plasma structures in strata of a glow discharge in a magnetic field. *Optics and Spectroscopy*, 100:456–462, 2006.

[135] E. Thomas, A.M. DuBois, B. Lynch, S. Adams, R. Fisher, D. Artis, S. LeBlanc, U. Konopka, R.L. Merlino, and M. Rosenberg. Preliminary characteristics of magnetic field and plasma performance in the magnetized dusty plasma experiment (mdpx). *J. Plasma Physics*, 80, 20014.

[136] E Thomas Jr, R L Merlino, and M Rosenberg. Magnetized dusty plasmas: the next frontier for complex plasma research. *Plasma Physics and Controlled Fusion*, 54:124034, 2012.

[137] Giichiro Uchida, Satoru Iizuka, Tetsuo Kamimura, and Noriyoshi Sato. Generation of two–dimensional dust vortex flows in a direct current discharge plasma. *Phys. Plasmas*, 16:053707, 2009.

[138] Huang Feng, Liu Yan-Hong, Chen Zhao-Yang, Wang Long, and Ye Mao-Fu. Cluster rotation in an unmagnetized dusty plasma. *Chinese Physics Letters*, 30:115201, 2013.

[139] A. Samarian, O. Vaulina, W. Tsang, and B. W. James. Formation of vertical and horizontal dust vortexes in an rf-discharge plasma. *Physica Scripta*, T98:123–126, 2002.

[140] G. E. Morfill, H. M. Thomas, U. Konopka, H. Rothermel, M. Zuzic, A. Ivlev, and J. Goree. Condensed plasmas under microgravity. *Phys. Rev. Lett.*, 83:1598–1601, 1999.

[141] M. R. Akdim and W. J. Goedheer. Modeling of self-excited dust vortices in complex plasmas under microgravity. *Phys. Rev. E*, 67:056405, 2003.

[142] W. J. Goedheer and M. R. Akdim. Vortices in dust clouds under microgravity: A simple explanation. *Phys. Rev. E*, 68:045401, 2003.

[143] M Schwabe, L-J Hou, S Zhdanov, A V Ivlev, H M Thomas, and G E Morfill. Convection in a dusty radio-frequency plasma under the influence of a thermal gradient. *New Journal of Physics*, 13:083034, 2011.

[144] S. Mitic, R. Sütterlin, A. V. Ivlev H. Höfner, M. H. Thoma, S. Zhdanov, and G. E. Morfill. Convective dust clouds driven by thermal creep in a complex plasma. *Phys. Rev. Lett.*, 101:235001, 2008.

[145] T. M. Flanagan and J. Goree. Gas flow driven by thermal creep in dusty plasma. *Phys. Rev. E*, 80:046402, 2009.

[146] O. S. Vaulina, A. P. Nefedov, O. F. Petrov, and V. E. Samaryan, A. A .and Fortov. Self-oscillations of macroparticles in the dust plasma of glow discharge. *Journal of Experimental and Theoretical Physics*, 93:1184–1189, 2001.

[147] M. R. Akdim and W. J. Goedheer. Modeling the effect of dust on the plasma parameters in a dusty argon discharge under microgravity. *Phys. Rev. E*, 67:066407, 2003.

[148] Nirab Chandra Adhikary, Heremba Bailung, Arup Ratan Pal, Joyanti Chutia, and Yoshiharu Nakamura. Observation of sheath modification in laboratory dusty plasma. *Phys. Plasmas*, 14:103705, 2007.

[149] N. D'Angelo. Ion-acoustic waves in dusty plasmas. *Planet. Space Sci.*, 42:507–511, 1994.

[150] Y. Nakamura. Experiments on ion-acoustic shock waves in a dusty plasma. *Phys. Plasmas*, 9:440–445, 2002.

[151] V. I. Molotkov, O. F. Petrov, M. Yu. Pustyl'nik, V. M. Torchinskii, V. E. Fortov, and A. G. Khrapak. Dusty plasma of a dc glow discharge: methods of investigation and characteristic features of behavior. *High Temperature*, 42:827–841, 2004.

[152] A. Barkan and R. L. Merlino. Confinement of dust particles in a double layer. *Phys. Plasmas*, 2:3261–3265, 1995.

[153] J. Pramanik, B. M. Veeresha, G. Prasad, and P.K. Sen, A.and Kaw. Experimental observation of dust- acoustic wave turbulence. *Physics Letters A*, 312:84 – 90, 2003.

[154] Yuri P. Raizer. *Gas Discharge Physics.* Springer-Verlag Berlin Heidelberg, 1991.

[155] A. H. Von Engel. *Ionised Gases.* Oxford: Oxford University Press, 1964.

[156] N St J Braithwaite. Introduction to gas discharges. *Plasma Sources Sci. Technol.*, 9:517, 2000.

[157] F. Paschen. *Wied. Ann.*, 37:69–96, 1889.

[158] Alan J. Lichtenberg Michael A. Lieberman. *Principles of Plasma Discharges and Materials Processing.* John Wiley & Sons, 2005.

[159] P. Chabert and N. St. J. Braithwaite. *Physics of Radio-Frequency Plasmas.* Cambridge University Press, New York, 2011.

[160] H. M. Mott-Smith and Irving Langmuir. The theory of collectors in gaseous discharges. *Phys. Rev.*, 28:727–763, 1926.

[161] N. Hershkowitz. How langmuir probes work. In O. Auciello and D. L. Flamm, editors, *Plasma Diagnostics, Discharge Parameters and Chemistry*, volume 1, chapter 3. Academic, Boston, 1989.

[162] R. L. Merlino. Understanding langmuir probe curent-voltage characteristics. *Amer. J. Phys*, 75:1078, 2007.

[163] V. I. Demidov, S. V. Ratynskaia, and K. Rypdal. Electric probes for plasmas: The link between theory and instrument. *Rev. Sci. Instrum.*, 73:3409–3439, 2002.

[164] F. F. Chen. Lecture notes on langmuir probe diagnostics. mini course on plasma disgnostics. IEEE-ICOPS meeting. Jeju, Korea, 2013.

[165] I. M. Hutchinson. *Principles of plasma diagnostics.* Cambridge University Press, Cambridge, 2011.

[166] Soumen Ghosh, Prabal K. Chattopadhyay, Joydeep Ghosh, and Dhiraj Bora. Rf compensation of single langmuir probe in low density helicon plasma. *Fusion Engineering and Design*, 112:915–918, 2016.

[167] R. M. Castro, G. A. Cirino, P. Verdonck, H. S. Maciel, M. Massi, M. B. Pisani, and R. D. Mansano. A comparative study of single and double langmuir probe techniques for rf plasma characterization. *Contrib. Plasma Phys.*, 39:235–246, 1999.

[168] E. O. Johnson and L. Malter. A floating double probe method for measurements in gas discharges. *Phys. Rev.*, 80:58–68, 1950.

[169] M. Y. Naz, A. Ghaffar, N. U. Rehman, S. Naseer, and M. Zakaullah. Double and triple langmuir probes measurments in inductively coupled nitrogen plasma. *Progress In Electromagnetics Research*, 114:113–128, 2011.

[170] J. P. Sheehan and N. Hershkowitz. Emissive probes. *Plasma Sources Sci. Technol.*, 20:063001, 2011.

[171] M. A. Makowski and G. A. Emmert. New method to measure plasma potential with emissive probes. *Rev. Sci. Instrum.*, 54:830–836, 1983.

[172] Robert F. Kemp and J. M. Sellen Jr. Plasma potential measurements by electron emissive probes. *Rev. Sci. Instrum.*, 37:455–461, 1966.

[173] J. R. Smith, N. Hershkowitz, and P. Coakley. Inflection–point method of interpreting emissive probe characteristics. *Rev. Sci. Instrum.*, 50:210–218, 1979.

[174] C. R. Hoffmann and D. J. Lees. A differential method of measuring plasma potential. *Plasma Physics*, 13:689, 1971.

[175] J. P. Sheehan, Y. Raitses, N. Hershkowitz, I. Kaganovich, and N. J. Fisch. A comparison of emissive probe techniques for electric potential measurements in a complex plasma. *Phys. Plasmas*, 18:073501, 2011.

[176] Craig F. Bohren and Donald R. Huffman. *Absorption and scattering of light by small particles.* Wiley: New York, 1983.

[177] C.A. Schneider, W.S. Rasband, and K.W. Eliceiri. Nih image to imagej: 25 years of image analysis. *Nature Methods*, 9:671–675, 2012.

[178] A. Liberzon, R. Gurka, and Z. Taylor. http://www.openpiv.net/openpiv-matlab, 2009.

[179] VA Vasiliev, Yu M Romanovskii, DS Chernavskii, and VG Yakhno. *Autowave Processes in Kinetic Systems: Spatial and Temporal Self-Organisation in Physics, Chemistry, Biology, and Medicine*, volume 11. Springer Science & Business Media, 2012.

[180] Zuev L. B., Danilov V. I., Barannikova S. A., Gonchikov K. V., and Zykovi I. Yu. On a new type of plastic deformation waves in solids. *Russian Physics Journal*, 44:169–177, 2001.

[181] Nicolas Garnier and Arnaud Chiffaudel. Nonlinear transition to a global mode for traveling-wave instability in a finite box. *Phys. Rev. Lett.*, 86:75–78, 2001.

[182] Suzanne J. M. H. Hulscher and C. Marjolein Dohmen-Janssen. Introduction to special section on marine sand wave and river dune dynamics. *J. Geophys. Res.*, 110:2156–2202, 2005.

[183] Hiraku Nishimori and Noriyuki Ouchi. Formation of ripple patterns and dunes by wind-blown sand. *Phys. Rev. Lett.*, 71:197–200, 1993.

[184] Sanjib Sarkar, M. Bose, S. Mukherjee, and J. Pramanik. Spatiotemporal evolution of dielectric driven cogenerated dust density waves. *Phys. Plasmas*, 20:064502, 2013.

[185] E. Thomas, Jr, and M. Watson. First experiments in the dusty plasma experiment device. *Phys. Plasmas*, 6:4111–4117, 1999.

[186] J. B. Pieper and J. Goree. Dispersion of plasma dust acoustic waves in the strong-coupling regime. *Phys. Rev. Lett.*, 77:3137–3140, 1996.

[187] R. L. Merlino, A. Barkan, C. Thompson, and N. D'Angelo. Laboratory studies of waves and instabilities in dusty plasmas. *Phys. Plasmas*, 5:1607–1614, 1998.

[188] V. E. Fortov, A. D. Usachev, A. V. Zobnin, V. I. Molotkov, and O. F. Petrov. Dust-acoustic wave instability at the diffuse edge of radio frequency inductive low-pressure gas discharge plasma. *Phys. Plasmas*, 10:1199–1208, 2003.

[189] W. D. Suranga Ruhunusiri and J. Goree. Synchronization mechanism and arnold tongues for dust density waves. *Phys. Rev. E*, 85:046401, 2012.

[190] J. D. Williams. Time-resolved measurement of global synchronization in the dust acoustic wave. *Phys. Rev. E*, 90:043103, 2014.

[191] V. A. Lisovskiy, V. A. Derevianko, and V. D. Yegorenkov. The child-langmuir collision laws for the cathode sheath of glow discharge in nitrogen. *Vacuum*, 103:49 – 56, 2014.

[192] T. E. Sheridan and J. Goree. Collisional plasma sheath model. *Phys. Fluids B*, 3:2796–2804, 1991.

[193] C. D. Child. Discharge from hot cao. *Phys. Rev. (Series I)*, 32:492–511, 1911.

[194] I. Langmuir. The interaction of electron and positive ion space charges in cathode sheaths. *Phys. Rev.*, 33:954–989, 1929.

[195] M. J. Goeckner, J. Goree, and T. E. Sheridan. Measurments of ion velocity and density in the plasma sheath. *Phys. Fluids B*, 4:1663, 1992.

[196] V. V. Yaroshenko, F. Verheest, H. M. Thomas, and G. E. Morfill. The bohm sheath criterion in strongly coupled complex plasmas. *New Journal of Physics*, 11:073013, 2009.

[197] J. Pramanik, G. Prasad, A. Sen, and P. K. Kaw. Experimental observations of transverse shear waves in strongly coupled dusty plasmas. *Phys. Rev. Lett.*, 88:175001, 2002.

[198] F. Verheest. Waves and instabilities in dusty space plasmas. *Space Sci Rev*, 77:267–302, 1996.

[199] Robert L. Merlino. Experimental investigations of dusty plasmas. *AIP Conference Proceedings*, 799:3–11, 2005.

[200] A. M. Lipaev, V. I. Molotkov, A. P. Nefedov, O. F. Petrov, V. M. Torchinskii, V. E. Fortov, A. G. Khrapak, and S. A. Khrapak. Ordered structures in a nonideal dusty glow-discharge plasma. *Journal of Experimental and Theoretical Physics*, 85:1110–1118, 1997.

[201] V. E. Fortov, A. P. Nefedov, V. M. Torchinskii, V. I. Molotkov, A. G. Khrapak, O. F. Petrov, and K. F. Volykhin. Crystallization of a dusty plasma in the positive column of a glow discharge. *JETP Letters*, 64(2):92–98, 1996.

[202] Vladimir E. Fortov and et al. Crystalline structures of strongly coupled dusty plasmas in dc glow discharge strata. *Physics Letters A*, 229:317–322, 1997.

[203] A. D. Usachev, A. V. Zobnin, O. F. Petrov, V. E. Fortov, M. H. Thoma, M. Y. Pustylnik, M. A. Fink, and G. E. Morfill. Elongated dust clouds in a uniform dc positive column of low pressure gas discharge. *Plasma Sources Sci. Technol.*, 25:035009, 2016.

[204] A. Melzer, A. Homann, and A. Piel. Experimental investigation of the melting transition of the plasma crystal. *Phys. Rev. E*, 53:2757–2766, 1996.

[205] Lee-Wen Teng, Mei-Chu Chang, Yu-Ping Tseng, and Lin I. Wave-particle dynamics of wave breaking in the self-excited dust acoustic wave. *Phys. Rev. Lett.*, 103:245005, 2009.

[206] Tim Bockwoldt, Oliver Arp, Kristoffer Ole Menzel, and Alexander Piel. On the origin of dust vortices in complex plasmas under microgravity conditions. *Phys. Plasmas*, 21:103703, 2014.

[207] O. Havnes, T. Nitter, V. Tsytovich, G. E. Morfill, and T. Hartquist. On the thermophoretic force close to walls in dusty plasma experiments. *Plasma Sources Science and Technology*, 3:448, 1994.

[208] H. Rothermel, T. Hagl, G. E. Morfill, M. H. Thoma, and H. M. Thomas. Gravity compensation in complex plasmas by application of a temperature gradient. *Phys. Rev. Lett.*, 89:175001, 2002.

[209] P. K. Shukla and A. A. Mamun. Dust-acoustic shocks in a strongly coupled dusty plasma. *IEEE Trans. Plasma Sci.*, 29:221–225, 2001.

[210] V. E. Fortov, O. F. Petrov, V. I. Molotkov, M. Y. Poustylnik, V. M. Torchinsky, V. N. Naumkin, and A. G. Khrapak. Shock wave formation in a dc glow discharge dusty plasma. *Phys. Rev. E*, 71:036413, 2005.

[211] Mangilal Choudhary, S. Mukherjee, and P. Bandyopadhyay. Propagation characteristics of dust–acoustic waves in presence of a floating cylindrical object in the dc discharge plasma. *Phys. Plasmas*, 23(8):083705, 2016.

[212] Noriyosh Sato, Giichiro Uchida, Toshiro Kaneko, Shinya Shimizu, and Satoru Iizuka. Dynamics of fine particles in magnetized plasmas. *Phys. Plasmas*, 8:1786–1790, 2001.

[213] Shota Nunomura, Noriyasu Ohno, and Shuichi Takamura. Effects of ion flow by e× b drift on dust particle behavior in magnetized cylindrical electron cyclotron resonance plasmas. *Japanese Journal of Applied Physics*, 36:877, 1997.

[214] F. M. H. Cheung, N. J. Prior, L. W. Mitchell, A. A. Samarian, and B. W. James. Rotation of coulomb crystals in a magnetized inductively coupled complex plasma. *IEEE Transactions on Plasma Science*, 31:112–118, 2003.

[215] O.S Vaulina, A.A Samarian, A.P Nefedov, and V.E Fortov. Self-excited motion of dust particles in a inhomogeneous plasma. *Physics Letters A*, 289:240–244, 2001.

[216] O. Ishihara and N. Sato. On the rotation of a dust particulate in an ion flow in a magnetic field. *IEEE Transactions on Plasma Science*, 29:179–181, 2001.

[217] Modhuchandra Laishram, Devendra Sharma, and Predhiman K. Kaw. Dynamics of a confined dusty fluid in a sheared ion flow. *Phys. Plasmas*, 21:073703, 2014.

[218] B. M. Veeresha, Amita Das, and Abhijit Sen. Rayleigh–taylor instability driven nonlinear vortices in dusty plasmas. *Phys. Plasmas*, 12(4):044506, 2005.

[219] Andria D. Rogava, Stefaan Poedts, and Zaza Osmanov. Transient shear instability of differentially rotating and self-gravitating dusty plasma. *Phys. Plasmas*, 11(4):1655–1662, 2004.

[220] A. V. Ivlev, S. K. Zhdanov, and G. E. Morfill. Free thermal convection in complex plasma with background-gas friction. *Phys. Rev. Lett.*, 99:135004, 2007.

[221] S. Mitic, R. Sütterlin, A. V. Ivlev H. Höfner, M. H. Thoma, S. Zhdanov, and G. E. Morfill. Convective dust clouds driven by thermal creep in a complex plasma. *Phys. Rev. Lett.*, 101:235001, 2008.

[222] O. S. Vaulina, A. A. Samarian, O. F. Petrov, B. W. James, and V. E. Fortov. Self-excited motions in dusty plasmas with gradient of charge of macroparticles. *New Journal of Physics*, 5:82, 2003.

[223] S. K. Zhdanov, A. V. Ivlev, and G. E. Morfill. Non-hamiltonian dynamics of grains with spatially varying charges. *Phys. Plasmas*, 12:072312, 2005.

[224] V. E. Fortov, O. S. Vaulina, O. F. Petrov, V. I. Molotkov, A. V. Chernyshev, A. M. Lipaev, G. Morfill, H. Thomas, H. Rotermell, S. A. Khrapak, Yu. P. Semenov, A. I. Ivanov, S. K. Krikalev, and Yu. P. Gidzenko. Dynamics of microparticles in a dusty plasma under microgravity conditions (first experiments on board the iss. *Journal of Experimental and Theoretical Physics*, 96:704–718, 2003.

[225] Themis Matsoukas and Marc Russell. Particle charging in low–pressure plasmas. *Journal of Applied Physics*, 77:4285–4292, 1995.

[226] V. E. Fortov, O. F. Petrov, O. S. Vaulina, and R. A. Timirkhanov. Viscosity of a strongly coupled dust component in a weakly ionized plasma. *Phys. Rev. Lett.*, 109:055002, 2012.

[227] V. Nosenko and J. Goree. Shear flows and shear viscosity in a two-dimensional yukawa system (dusty plasma). *Phys. Rev. Lett.*, 93:155004, 2004.

[228] Mangilal Choudhary, S. Mukherjee, and P. Bandyopadhyay. Experimental observation of self excited co-rotating multiple vortices in a dusty plasma with inhomogeneous plasma background. *Phys. Plasmas*, 24:033703, 2017.

[229] L. M. Vasilyak, S. P. Vetchinin, A. A. Obvival'neva, and D. N. Polyakov. Parametric excitation and stabilization of dust structures in glow discharge under the action of nanosecond electric pulses. *Tech. Phys. Lett.*, 33:135–138, 2007.

[230] M. Y. Pustylnik, A. V. Ivlev, H. M. Thomas, G. E. Morfill, L. M. Vasilyak, S. P. Vetchinin, D. N. Polyakov, and V. E. Fortov. Effect of high-voltage nanosecond pulses on complex plasmas. *Phys. Plasmas*, 16:113705, 2009.

[231] L.M. Vasilyak, V.E. Fortov, G.E. Morfill, A.V. Ivlev, M.Y. Pustylnik, D.N. Polyakov, H.M. Thomas, and S.P. Vetchinin. Increase of kinetic energy of dusty cluster particles due to parametric instability caused by nanosecond electric pulses. *Contrib. Plasma Phys.*, 51:529–532, 2011.

[232] M.Choudhary, S. Kar, and S. Mukherjee. Long-time evolution of a low pressure laboratory plasma after application of transient high voltage positive pulses. *Contrib. Plasma Phys.*, 56:878–888, 2016.

[233] C. Arnas, M. Mikikian, and F. Doveil. High negative charge of a dust particle in a hot cathode discharge. *Phys. Rev. E*, 60:7420–7425, 1999.

[234] O. S. Vaulina, S. A. Khrapak, A. P. Nefedov, and O. F. Petrov. Charge-fluctuation-induced heating of dust particles in a plasma. *Phys. Rev. E*, 60:5959–5964, 1999.